学位論文

Coupled proton-electron transfer in excited states of X-$MnOH_2$: A nonadiabatic electron wavepacket study

(X-$MnOH_2$ の励起状態におけるプロトン-電子移動の電子動力学)

平成 26 年 12 月 16 日 博士 (理学) 申請

東京大学大学院理学系研究科
化学専攻
山本 憲太郎

Abstract

A number of chemical reaction mechanisms involving nonadiabatic interaction as an essential factor are presented. We investigate those mechanisms by using nonadiabatic electron wavepacket dynamics theory. Here the electronic wavepacket is explicitly time-dependent to go beyond the Born–Oppenheimer approximation (adiabatic approximation between nuclear and electronic motions). We are especially concerned with low energy dynamics, where the total energy allocated to the nuclear motion toward the potential barrier is as much as its height. In this case, nonadiabatic interaction is rather crucial than unignorable. In the first half of the present thesis, we discuss explicit path-branching induced by nonadiabatic interaction. We develop an algorithm based on the so-called path-branching representation (PBR) to apply it to the low energy dynamics. Through the dynamics calculations in a one-dimensional model system, we propose two mechanisms, namely, a tunneling-like effect and a friction-like effect induced by nonadiabatic interaction. Full-quantum calculations and multi-dimensional implementation are also performed to obtain results parallel to the one-dimensional ones.

In the second half, we demonstrate photodynamics of X-$MnOH_2$ to propose a mechanism of coupled proton-electron transfer in excited states resulting in charge separation. We are stimulated to examine this system by a Mn cluster embedded in the photosystem II (PSII). The Mn cluster performs photo-driven oxidation of water molecules to provide protons and electrons, which is known to be an early process of photosynthesis. In the proposed mechanism, the proton and electron take mutually different pathways to reach spatially different places on the accepter to induce charge separation. The roles of Ca in PSII and the relation to the Mn cluster are also presented. Through those nonadiabatic electron wavepacket dynamics, we provide further insight into chemical reactions that is beyond the scope of the standard method based on the Born–Oppenheimer approximation.

Contents

List of Figures

Chapter 1

General introduction

The Born–Oppenheimer approximation [1] (adiabatic approximation between the nuclear and electronic motions) is a basis of all molecular quantum mechanics. [2] The large mass of a nucleus compared to that of an electron allows us to approximately separate the electronic and nuclear motions. This separation vastly simplifies quantum treatment of molecules, where we just solve an eigenvalue problem with respect to an electronic Hamiltonian $\hat{H}^{(el)}(\mathbf{r};\mathbf{R})$ as

$$\hat{H}^{(el)}(\mathbf{r};\mathbf{R})\Phi_\alpha(\mathbf{r};\mathbf{R}) \;=\; V_\alpha(\mathbf{R})\Phi_\alpha(\mathbf{r};\mathbf{R}). \tag{1.1}$$

Such a time-independent electronic state theory is widely recognized as a robust framework of molecular science, in which the obtained V_0 (the ground electronic state) form Eq. (1.1) is used as a potential function of the nuclear configuration.

However, necessity of nonadiabatic treatment of a molecule arises in some exotic cases. Laser chemistry requires such a treatment of electrons. [3] The rapid advances of ultrashort pulse lasers have reached pulse width shorter than 100 attoseconds, [4–6] which is comparable to the time scale of electron dynamics. A molecule with highly (quasi) degenerate electronic states is also of interest. [7] In this case, isolated molecular electronic states become almost meaningless. [8]

A chemical reaction requires the nonadiabatic treatment as well, if the relevant shift of nuclear configuration modifies electronic states in quality. In such a chemical reaction, nonadiabatic electron dynamics is inevitable for appropriate description of molecular dynamics. This is the situation of the main interest in the present thesis. Typical examples can be found in a forbidden reaction of the Woodward-Hoffman symmetry conservation, [9] fast relaxation of

excited states through conical intersections, [2] and a coupled electron and proton transfer reaction. [10, 11] In order to tackle such nonadiabatic problems, methodology should be developed to take in mutually coupled multiple adiabatic states to express nonadiabatic transition. In addition, it should be multi-dimensional so as to consider the interesting nonadiabatic effects including those of a conical intersection [2] and a geometric phase. [12] Thus the problem is essentially multi-state and multi-dimensional, and the involved electronic states must be time-dependent.

Technically speaking, a full-quantum approach to such a multi-state and multi-dimensional molecular system is too difficult in practice. Instead, various methods have been proposed to enable us to investigate the nonadiabatic problems (discussed in Chapter 2 in detail). Some of the methods including surface hopping methods [13–19] can take in nonadiabatic transition. However, they are not suitable for electron dynamics, because they involve unphysical sudden change of electronic states (hopping). In contrast, we approach this problem by means of an on-the-fly nonadiabatic method based on the so-called path-branching representation (PBR), [3, 8, 20–29] which can describe nuclear and electron dynamics consistently. We can clearly interpret the physical picture of both electrons and nuclei with PBR. This feature enables us to investigate insight into chemical reactions.

In the present thesis, we discuss novel mechanisms relevant to chemical reactions involving nonadiabatic interaction thorough electron wavepacket dynamics. We are especially concerned with low energy dynamics, where the total energy allocated to the nuclear motion toward the potential barrier is as much as its height. In this case, nonadiabatic interaction is rather crucial than unignorable. We begin with a one-dimensional model system, and proceed to multi-dimensional molecular systems. The discussion flows from conceptual to realistic. The rest of the thesis is organized to reflect this flow as clearly as possible. In Chapter 2, we examine rather conceptual aspect of chemical reactions involving path-branching induced by nonadiabatic interaction. We briefly review the theory of PBR [3, 8, 20–29] and develop an algorithm so that we can investigate low energy systems, where the total energy allocated to nuclei is comparable to the barrier height. [29] We demonstrate a tunneling-like effect and a friction-like effect induced by nonadiabatic interaction in a one-dimensional model system by using the derived algorithm. Full-quantum dynamics in the same model system is presented for qualitative comparison. We also perform the multi-dimensional implementation of the PBR dynamics for a molecular system to confirm that the mechanisms obtained above are not the characteristics

of the one-dimensional system.

In Chapter 3, we examine rather realistic molecular systems to discuss photodynamical mechanisms resulting in charge separation in excited electronic states. The mechanism is called coupled proton-electron transfer, where the proton and electron take mutually different pathways to reach spatially different places on the acceptor. [11] That is the reason why the charge separation is induced. The target systems commonly include a Mn atom. We are stimulated to examine such systems by the Mn cluster in photosystem II (PSII). The Mn cluster performs photo-driven oxidation of water molecules to produce protons and electrons, which is the early process of photodynamics. The roles of a Ca atom in PSII are discussed by direct comparison of the systems with and without Ca. We briefly investigate the relationship between the system of X-$MnOH_2$ and the Mn cluster in PSII to find they resemble each other significantly. Another scenario (electron attachment instead of the coupled proton-electron transfer) is also mentioned.

Chapter 4 concludes this thesis. Some appendices follow to address technical details.

Chapter 2

Low energy path-branching dynamics and mechanisms induced by nonadiabatic interaction

2.1 Introduction

The theory of nonadiabatic electron wavepackets has two mutually coupled aspects: One is time-dependent nonadiabatically bifurcating electron wavepackets and the other is the dynamics of associated nuclear paths, [30] which carry those electron wavepackets and branch in the nonadiabatic regions (see Ref. [26] and Ref. [3] for review). It is therefore quite important to know how the nuclear paths behave in those critical regions.

As an alternative to quantum-wavefunction method, path concept (as in path integration, [31, 32] semiclassical dynamics, [33, 34] classical trajectory analysis, and so on) is often very useful for conceptual understanding and qualitative analysis of chemical reactions. An example of particularly characteristic dynamical processes is (tentatively) trapping phenomenon of a path in the transition state region of the saddle structure. In addition to the reactive resonances (either Feshbach type or shape resonance), two origins of trapping have been reported. One is a periodic bouncing motion, the trajectory of which is transversal to the reaction coordinate, forming the so-called periodic orbit dividing surface. [35, 36] The other is more universal and emerges from the kinematic coupling between molecular rotation and vibration, which effectively makes a potential basin in the saddle region. [37] These are relevant not only to the rate process but to spectroscopies of the transition states (see [38] for an extensive review of transition-state

spectroscopy. For a theory see [39]). Another interesting dynamics is deep tunneling, in which a "path" penetrates into a potential barrier and eventually passes across to leak in the other side. [40–45] This is a purely quantum phenomenon, and yet it can be well described with paths in complex phase-space (or imaginary time) or by the so-called Bohmian trajectories. [46, 47] These are dynamics on a single potential energy surface (PES).

In molecular systems, however, potential barriers (negatively convex structure along a reaction coordinate) are quite often created by nonadiabatic interactions with upper potential energy surfaces having basin-like structures. [2, 48] The relevant effects manifest themselves in spectroscopy through the Jahn-Teller effect and so on. [49] As for reactive scattering, the so-called nonadiabatic tunneling as studied with Zhu-Nakamura theory is a highlight in semiclassical path dynamics. [50] For a high-energy passage across nonadiabatic regions, the surface hopping model is well accepted to conveniently describe nonadiabatic jump within the (classical) path dynamics. [13–19] On the other hand, it has been revealed by full-quantum studies [51–54] and experiments [55–57] that the passage of quantum wavepackets across nonadiabatic regions (avoided crossing and conical intersection) can be indeed observed. In particular, the theory of time-resolved photoelectron spectroscopy has illustrated how the wavepacket bifurcations can be reflected in the photoelectron signals and how they can be dynamically controlled. [51–54, 58] The wavepacket bifurcation is indeed essential because it is a manifestation of electron-nuclear quantum entanglement induced by nonadiabatic interactions.

Such wavepacket bifurcation can be nicely represented in terms of the so-called path-branching representation based on continuous non-Born–Oppenheimer paths in the theory of nonadiabatic electron wavepacket dynamics. [3, 8, 20–29] In this theoretical framework, a Hamiltonian in the general mixed quantum and classical representation described in the electronic Hilbert space and nuclear configuration space is first established, with which the electronic wavepacket dynamics as well as the relevant nuclear path solutions are sought for. The solutions of these dynamics give rise to infinitely many branching nuclear paths to represent the wavepacket bifurcation as emphasized above. However, the exact solutions of the dynamics should be too complicated and time-consuming to attain. Therefore we introduce an approximate yet appropriate averaging procedure to reduce the number (frequency) of the path-branchings. A typical example can be seen in Refs. [3, 22]. To be a little more precise, the path-branching representation consists of repeated applications of (i) averaging of many to-be-branched paths and (ii) branching of these averaged paths under certain conditions. The branching is performed in terms of

the so-called force matrix. [20] Numerical assessments, accuracy and tractability of the method of path branching, have been repeatedly performed with affirmative conclusions. [3, 8, 20–29]

In these former studies, however, we studied systems of rather high energy dynamics; the total energy of the studied systems is higher than the energy of avoided crossing or conical intersection. In order to study nonadiabatic chemical reactions in a low energy domain, on the other hand, we need more careful treatment of path branching for the non-Born–Oppenheimer trajectories. We therefore first revisit and refine the branching-and-averaging algorithm in an energy range comparable to the height of potential barriers. We also show that the total energy thus partitioned to the branched paths is conserved, even if some of the branched nuclear paths penetrate into classically inaccessible domains. Thus these non-Born–Oppenheimer paths can undergo classical forbidden events through nonadiabatic interactions.

To illustrate such nonclassical events as a manifestation of electronic quantum effects on nuclear paths, we study two characteristic phenomena relevant to chemical reaction dynamics for an incident nuclear wavepacket to encounter a potential barrier, on top of which lies another adiabatic potential curve with nonadiabatic coupling. Two cases are surveyed: (1) Initial paths coming into the nonadiabatic interaction region with energy lower than the barrier height, and each can branch into two pieces (and repeat branching subsequently), the upper counterpart of which may penetrate into the higher energy region and eventually branches back to the ground state and proceed to the product site. This is so to say surmounting the potential barrier via nonadiabatically coupling excited state. (2) A classical path whose initial energy is a little higher than the barrier (and may be lower than the bottom of the excited state) can branch and some of whose counterparts are trapped on top of the potential barrier. Those two mechanisms are also termed in short a tunneling-like effect and a friction-like effect induced by nonadiabatic interaction, respectively. It follows concomitantly that the trains of pulse-like waves flow both to product and reactant sides with time-delay are observed. Such expectations arising from the path-branching representation are numerically confirmed with full quantum mechanical wavepacket dynamics. Although we here treat only a one-dimensional case since it is most illustrative for qualitative presentation, the extension of path-branching theory to multi-dimensional systems is rather straightforward.

This chapter is organized as follows. In Section 2.2, we outline the theoretical framework of path-branching representation and then extend it so as to be able to treat low energy nonadiabatic transitions by proposing a branching condition. Analysis on how the state populations

and associated energies are partitioned to those individual paths is presented. In Section 2.3, the algorithm is applied to the 1-dimensional 2-state model system. In Section 2.4 full-quantum studies will be presented to confirm those expected wavepacket branching phenomena. In Section 2.5, we perform multi-dimensional implementation for molecular systems. Section 2.6 concludes the chapter.

2.2 Smooth path branching into classically forbidden regions

2.2.1 Electron wavepacket dynamics along nuclear non-Born–Oppenheimer (BO) paths

First we briefly review the path-branching representation of nonadiabatic electron wavepacket dynamics. Further details are available elsewhere. [3, 8, 20–29] In this theory, dynamics of the nuclear degrees of freedom is realized by branching non-Born–Oppenheimer paths, and the electron wavepackets propagate in time on these paths. Suppose we have a nonrelativistic molecular system without external electromagnetic fields. The quantum molecular Hamiltonian is written generally as

$$H(\mathbf{r},\mathbf{R}) \;=\; \frac{1}{2}\sum_k \hat{P}_k^2 + H^{(el)}(\mathbf{r};\mathbf{R}), \tag{2.1}$$

where $H^{(el)}(\mathbf{r};\mathbf{R}) = \frac{1}{2}\sum_j \hat{p}_j^2 + V_c(\mathbf{r},\mathbf{R})$ is the electronic Hamiltonian, with $\mathbf{r}$ and $\mathbf{R}$ denoting the electronic and nuclear coordinates, respectively. $\hat{p}_j$ and $\hat{P}_k$ are the operators of the conjugate momenta of the components r_j and R_k of $\mathbf{r}$ and $\mathbf{R}$, respectively. $V_c(\mathbf{r};\mathbf{R})$ represents the Coulomb interactions. Rewriting the total Hamiltonian Eq. (2.1) in the Hilbert space for electrons and configuration space for nuclei as

$$H(\mathbf{R},elec) \equiv \frac{1}{2}\sum_k \left(\hat{P}_k - i\hbar\sum_{IJ}|\Phi_I\rangle X_{IJ}^k\langle\Phi_J|\right)^2 + \sum_{IJ}|\Phi_I\rangle H_{IJ}^{(el)}\langle\Phi_J|. \tag{2.2}$$

Replacing the nuclear momentum operator here in this expression with the classical counterpart $\hat{P}_k \to P_k$, we define the mixed quantum-classical Hamiltonian. Then we apply the time-dependent variational principle with this Hamiltonian and attain the equations of motion for

electron as

$$i\hbar\frac{dC_I}{dt} = \sum_J \left(H_{IJ}^{(el)} - i\hbar \sum_k \dot{R}_k X_{IJ}^k - \frac{\hbar^2}{2} \sum_k Y_{IJ}^k \right) C_J, \tag{2.3}$$

where the electron wavepacket state $\Psi_{\rm elec}(\mathbf{R}\,(t))$ is expanded in basis functions at each nuclear position $\mathbf{R}(t)$ as

$$\Psi_{\rm elec}(\mathbf{r}, \mathbf{R}, t) = \sum_I C_I(t)\ \Phi_I(\mathbf{r}; \mathbf{R})|_{\mathbf{R}=\mathbf{R}(t)} \tag{2.4}$$

with $\{\Phi_I(\mathbf{r}; \mathbf{R}(t))\}$ being the Slater determinants, configuration state functions (CSF), adiabatic electronic functions, and so on at $\mathbf{R} = \mathbf{R}(t)$. The matrix elements in these expressions are defined as

$$H_{IJ}^{(el)} = \left\langle \Phi_I \left| \hat{H}^{(el)} \right| \Phi_J \right\rangle, \quad X_{IJ}^k = \left\langle \Phi_I \left| \frac{\partial}{\partial R_k} \right| \Phi_J \right\rangle \ \text{ and } \ Y_{IJ}^k = \left\langle \Phi_I \left| \frac{\partial^2}{\partial R_k^2} \right| \Phi_J \right\rangle. \tag{2.5}$$

In what follows, bra-ket inner products represent the integrations over the electronic coordinates. We have omitted the terms related to the external fields for the sake of simplicity, but the relevant generalization is rather straightforward. [3, 8, 24–29]

The nuclear path solutions are to be obtained by the Hamilton canonical equations of motions, which in turn give the force matrix $\mathbf{F}(\mathbf{R})$, a matrix representation of the force operator $\hat{\mathcal{F}}^k$ in the kth direction, to drive the nuclear motion, which is defined as

$$\begin{aligned} \mathbf{F}_{IJ}^k &= \langle \Phi_I | \hat{\mathcal{F}}^k | \Phi_J \rangle \\ &= -\left[\frac{\partial H_{IJ}^{(el)}}{\partial R_k} + \sum_K \left(X_{IK}^k H_{KJ}^{(el)} - H_{IK}^{(el)} X_{KJ}^k \right) \right] \\ &\quad + i\hbar \sum_l \dot{R}_l \left[\frac{\partial X_{IJ}^l}{\partial R_k} - \frac{\partial X_{IJ}^k}{\partial R_l} \right], \end{aligned} \tag{2.6}$$

In the semiclassical Ehrenfest theory (SET), [59–64] one takes an force average in the kth direction over the electron wavepacket such that

$$\begin{aligned} \ddot{\mathbf{R}}^k &= \langle \Psi_{\rm elec}(\mathbf{r}, \mathbf{R}, t) | \hat{\mathcal{F}}^k | \Psi_{\rm elec}(\mathbf{r}, \mathbf{R}, t) \rangle = \sum_{I,J} C_I^* \mathbf{F}_{IJ}^k C_J \\ &= -\sum_{I,J,K} C_I^* \left(X_{IK}^k H_{KJ}^{(el)} - H_{IK}^{(el)} X_{KJ}^k \right) C_J - \sum_{IJ} C_I^* \frac{\partial H_{IJ}^{(el)}}{\partial R_k} C_J, \end{aligned} \tag{2.7}$$

which is equivalent to the Hellmann-Feynman force

$$\ddot{\mathbf{R}}^k = -\left\langle \Psi_{\rm elec}(\mathbf{R}(t)) \left| \frac{\partial H^{(el)}}{\partial R_k} \right| \Psi_{\rm elec}(\mathbf{R}(t)) \right\rangle, \tag{2.8}$$

if the electronic basis set happens to be complete. Note also that if X^k_{IJ} is virtually zero in the adiabatic representation, the force matrix has only the diagonal elements, which are equivalent to the ordinary forces given by the energy gradients of the potential energy surfaces.

2.2.2 The semiclassical Ehrenfest paths

The mean-field paths in the semiclassical Ehrenfest theory (SET), [59–64] appear to be as a special case of the present theory when we take a force average in the kth direction over the electron wavepacket such that

$$\begin{aligned} \ddot{\mathbf{R}}^k &= \langle \Psi_{\rm elec}(\mathbf{r},\mathbf{R},t) | \hat{\mathcal{F}}^k | \Psi_{\rm elec}(\mathbf{r},\mathbf{R},t) \rangle = \sum_{I,J} C^*_I \mathbf{F}^k_{IJ} C_J \\ &= -\sum_{I,J,K} C^*_I \left(X^k_{IK} H^{(el)}_{KJ} - H^{(el)}_{IK} X^k_{KJ} \right) C_J - \sum_{IJ} C^*_I \frac{\partial H^{(el)}_{IJ}}{\partial R_k} C_J, \end{aligned} \tag{2.9}$$

which is equivalent to the Hellmann-Feynman force

$$\ddot{\mathbf{R}}^k = -\left\langle \Psi_{\rm elec}(\mathbf{R}(t)) \left| \frac{\partial H^{(el)}}{\partial R_k} \right| \Psi_{\rm elec}(\mathbf{R}(t)) \right\rangle, \tag{2.10}$$

if the electronic basis set happens to be complete. Recall, however, that the equation for electronic state mixing, Eq. (2.3), contains the second-order derivative terms that does not arise in the intuitively-derived equations of motion for the standard SET.

The SET is known to give very accurate nonadiabatic transition amplitude up to the quantum phases as long as it is before the path enters an asymptotic region, where the nonadiabatic coupling elements begin to vanish. [22] As stressed in Section 2.1, the nonadiabatic interactions let the full quantum nuclear wavepackets branch into those pieces that eventually run on the individual adiabatic potential surfaces. But an SET mean-field path can never branch in itself but runs on an averaged potential surface.

Recently new lights are shed on the Ehrenfest paths. Miller has found a particular physical relevance of these paths [65, 66] (see also [67]) from the view point of the so-called Meyer-Miller-Stock-Thoss theory. [59, 68] Shalashilin [69–71] has developed an MCTDH-

based method [72, 73] for the Gaussian coherent states guided by many Ehrenfest paths. This idea is an interesting modification of the method of generating basis functions due to the multiple spawning method. [74–76] (Note though that the SET paths cannot always cover the entire path-space as illustrated in Refs. [22, 23].) We also use the force averaging procedure in the present theory to partly generate mean-paths before path-branchings. However, the main concern of this work is to see how the non-Born–Oppenheimer paths are led to branch naturally by the electronic quantum effects. In particular, we demonstrate that such branched paths are naturally deformed and can penetrate into nonclassical domains, which are important for qualitative understanding of chemical dynamics.

2.2.3 Phase-space averaging and natural branching (PSANB) of the non-BO paths in low energy regime

Technically, the exact solutions of Eqs. (2.3) and (2.6) give rise to the rapid increase of the infinite number of paths. Therefore we need to devise a numerical practice to suppress such unlimited path-branchings. One of such algorithms has already been studied in an energy region higher than those of the relevant avoided crossing or conical intersections, which is called phase-space averaging and natural branching of paths (PSANB). [3, 8, 20–29] We here propose an alternative path-branching algorithm for nonadiabatic dynamics, which works better in a low energy regime. Since the new algorithm shares the many common practices with the high energy PSANB, we begin with a brief review of it.

Force diabatization and branching paths

The force operator $\mathcal{F}$ itself can induce electronic-state mixing because of its off-diagonal elements. Such electronic-state mixing can be avoided by diagonalization of the force matrix for each short time interval Δt at a nuclear position $\mathbf{R}$ as

$$\mathcal{F}(\mathbf{r};\mathbf{R})\lambda_K(\mathbf{r};\mathbf{R}) = f_K(\mathbf{R})\lambda_K(\mathbf{r};\mathbf{R}), \tag{2.11}$$

where $\lambda_K(\mathbf{r};\mathbf{R})$ and $f_K(\mathbf{R})$ are the Kth eigenfunction and eigenforce, respectively. The electron wavepacket at $\mathbf{R}$ may be expanded in $\{\lambda_K\}$ such that

$$\Psi_{\rm elec}(\mathbf{r};\mathbf{R}(t)) = \sum_K D_K(t)\lambda_K(\mathbf{r};\mathbf{R}). \tag{2.12}$$

Each electronic component $D_K\lambda_K(\mathbf{r};\mathbf{R})$ is carried by its own path driven by the eigenforce f_K, without electronic-state mixing among $\{\lambda_K\}$. Note that different eigenforces make different paths even if they start from a single phase space point $(\mathbf{R},\mathbf{P})$ such as

$$(\mathbf{R},\mathbf{P}) \to (\mathbf{R}_K,\mathbf{P}_K). \tag{2.13}$$

Hence the number of paths which stem from a single path is as many as that of electronic states involved in the nonadiabatic coupling. This is the origin of continuous path-branching.

Averaging over the paths to extract a (few) representative path(s) in the coupling region

The main purpose of PSANB [3, 8, 20–29] is to extract the "representative path" from the cascade of branching paths. It is expected that the nonadiabatic region is narrow enough that those branching paths should not geometrically deviate much from each other in phase space. Therefore they should localize along a representative path forming a tube-like structure. We extract such a path by taking an average of phase-space points in the following manner.

1. At a phase-space point $(\langle\mathbf{R}(t)\rangle,\langle\mathbf{P}(t)\rangle)$, diagonalize the force matrix as in Eq. (2.11).

2. The Kth eigenforce drives a path starting from $(\langle\mathbf{R}(t)\rangle,\langle\mathbf{P}(t)\rangle)$ for a short time Δt as

$$\mathbf{R}_K(t+\Delta t) = \langle\mathbf{R}(t)\rangle + \Delta\mathbf{R}_K, \tag{2.14}$$

$$\mathbf{P}_K(t+\Delta t) = \langle\mathbf{P}(t)\rangle + \Delta\mathbf{P}_K, \tag{2.15}$$

3. Average them into the form

$$\langle\mathbf{R}(t+\Delta t)\rangle = \langle\mathbf{R}(t)\rangle + \sum_K |D_K(t)|^2\Delta\mathbf{R}_K / \sum_L |D_L(t)|^2 \tag{2.16}$$

and

$$\langle\mathbf{P}(t+\Delta t)\rangle = \langle\mathbf{P}(t)\rangle + \sum_K |D_K(t)|^2\Delta\mathbf{P}_K / \sum_L |D_L(t)|^2, \tag{2.17}$$

which make the next point $(\langle\mathbf{R}(t+\Delta t)\rangle,\langle\mathbf{P}(t+\Delta t)\rangle)$ of the representative path.

4. With this averaged point, we diagonalize the force matrix as in Eq. (2.11) at this phase-space point and return to the step 2. The successive applications of procedures 1-3 give a single finite path.

Phase-space averaging of to-be-branched paths versus the force averaging (SET)

In the eigenforce representation, the averaged forces in the SET (recall Eq. (2.9)) are represented as

$$\ddot{\mathbf{R}}^k = \sum_K |D_K(t)|^2 f_K^k / \sum_L |D_L(t)|^2. \tag{2.18}$$

The first order approximation to the SET is

$$\begin{aligned} \langle \mathbf{P}(t+\Delta t)\rangle_{SET} &= \langle \mathbf{P}(t)\rangle + \ddot{\mathbf{R}}\Delta t \\ &= \langle \mathbf{P}(t)\rangle + \sum_K |D_K(t)|^2 \Delta \mathbf{P}_K / \sum_L |D_L(t)|^2 \end{aligned} \tag{2.19}$$

and

$$\begin{aligned} \langle \mathbf{R}(t+\Delta t)\rangle_{SET} &= \langle \mathbf{R}(t)\rangle + \langle \mathbf{P}(t)\rangle \Delta t \\ &= \langle \mathbf{R}(t)\rangle + \langle \mathbf{P}(t)\rangle \sum_K |D_K(t)|^2 \Delta t / \sum_L |D_L(t)|^2 \end{aligned} \tag{2.20}$$

Equations (2.19) and (2.17) are formally the same (to the first order) for the short interval. Also, it holds

$$\langle \mathbf{P}(t)\rangle \sum_K |D_K(t)|^2 \Delta t \simeq \sum_K |D_K(t)|^2 \Delta \mathbf{R}_K \tag{2.21}$$

in the first order approximation, and Eqs. (2.20) and (2.16) are also very close to each other in the first order of Δt. Thus, it turns out that phase-space averaging and SET are equivalent to each other in the first order approximation. Technically, however, the latter (SET) should be faster than the former (PSANB) because diagonalization of the force matrix is not necessary. Therefore we use the force averaging as an averaging procedure in what follows for its simplicity.

2.2.4 A guiding principle to let an averaged path branch

Branching condition

We next consider a condition to terminate the averaging procedure at a point, where one can judge that it is inaccurate or not physically appropriate to continue the averaging. Such points can be either an exit point of the interaction region or even in a region of strong coupling. In

our former studies, [3, 8, 20–29] the path-branching condition was set to

$$|\dot{R}X_{IJ}| < A \tag{2.22}$$

with A being a parameter that should be predetermined appropriately. This method has been proved to be very useful for high energy cases compared to the barrier height to obtain relevant paths and transition probability. Moreover, Eq. (2.22) has been applied mainly to the path branching at the exit of nonadiabatic region. This is because for high energy passage of nonadiabatic region an averaged path gives a good approximation as long as the nonadiabatic electronic state mixing is strong. Therefore path branching that terminates the averaging was usually applied once at an exit from the region of strong coupling. However, in case of an energy comparable with or lower than the crossing energy, the branched paths in the strong coupling region should well represent precise phenomena induced by the bifurcating quantum wavepackets. For instance, when the total energy is comparable to the barrier height, it is anticipated that one path may surmount the barrier while the other comes back. We therefore consider below which conditions should be theoretically acceptable and numerically tractable.

It is quite natural to judge that path-averaging is no longer good when the average path deviates appreciably from the paths that are generated according to their own individual eigenforces. Suppose an averaged path lies at a phase space point $(\mathbf{R}(t), \mathbf{P}(t))$. From this point on, we can keep generating an averaged path. But unaveraged paths can emanate that are driven by the individual eigenforces $f_K(\mathbf{R})$. With $(\mathbf{R}(t), \mathbf{P}(t))$ being the initial point a path given by, say, $f_K(\mathbf{R})$ is propagated as

$$\mathbf{R}_K(t + \Delta t) = \mathbf{R}_K(t) + \Delta\mathbf{R}_K, \tag{2.23}$$

$$\mathbf{P}_K(t + \Delta t) = \mathbf{P}_K(t) + \Delta\mathbf{P}_K, \tag{2.24}$$

where K is fixed for each path. We call these trajectories side paths. The number of side paths is as many as that of eigenforces. The side paths are made restart at each starting point of the average paths. They gradually deviate from each other, reflecting the diversity of the relevant paths due to the nonadiabatic interactions. Some of the side paths are expected to run on the edge of the cascade of branching paths as shown in Fig. 2.1. Therefore we monitor a pair of side paths that are most separate in phase space, and if the distance exceeds a predetermined

value Θ such that

$$\sum_{K<L} |\mathbf{R}_K - \mathbf{R}_L|^2 + |\mathbf{P}_K - \mathbf{P}_L|^2 > \Theta, \tag{2.25}$$

we judge that the real paths surrounding the average path are too widely distributed and it is a time to terminate the path-averaging.

Branching

We here consider only a two-state case for simpler illustration, and extension to the more states is rather straightforward. Suppose at a phase space point $(\mathbf{R}(t), \mathbf{P}(t))$ we have a SET path, for which the force diagonalization gives a set of $\{D_1(t), D_2(t)\}$ for the force eigenstates $\{\lambda_1(\mathbf{r}, \mathbf{R}(t)), \lambda_2(\mathbf{r}, \mathbf{R}(t))\}$, giving rise to an electron wavepacket

$$\Phi(t) = D_1(t)\lambda_1(\mathbf{r}, \mathbf{R}(t)) + D_2(t)\lambda_2(\mathbf{r}, \mathbf{R}(t)). \tag{2.26}$$

We here consider the following two propagation of the state: (1) Continue the Ehrenfest dynamics for the next short time interval Δt (denoted as path 0), and (2) let the path branch into two pieces (path 1 and 2). For the path-branching, along with the associated electronic state mixing, we prepare two vectors as the initial electronic states (at time t)

$$(D_1(t), 0) \quad \text{and} \quad (0, D_2(t))\,. \tag{2.27}$$

The wavefunctions for them are, respectively,

$$\Phi_1(t) = D_1(t)\lambda_1(\mathbf{r}, \mathbf{R}(t)) \quad \text{and} \quad \Phi_2(t) = D_2(t)\lambda_2(\mathbf{r}, \mathbf{R}(t)). \tag{2.28}$$

With these initial conditions, two SET paths are generated. Then at time $t + \Delta t$ we compare the energies thus partitioned. This gives two branching paths, which are different from the SET path, as schematically illustrated in Fig. 2.1.

2.2.5 Energy allocated to branching paths and energy conservation

In branching from an averaged path as above, those paths can have different (higher and lower) energies than that of the averaged (parent) path. Therefore we should survey how the populations and energies should be allocated to each path, and in so doing it is confirmed that the total

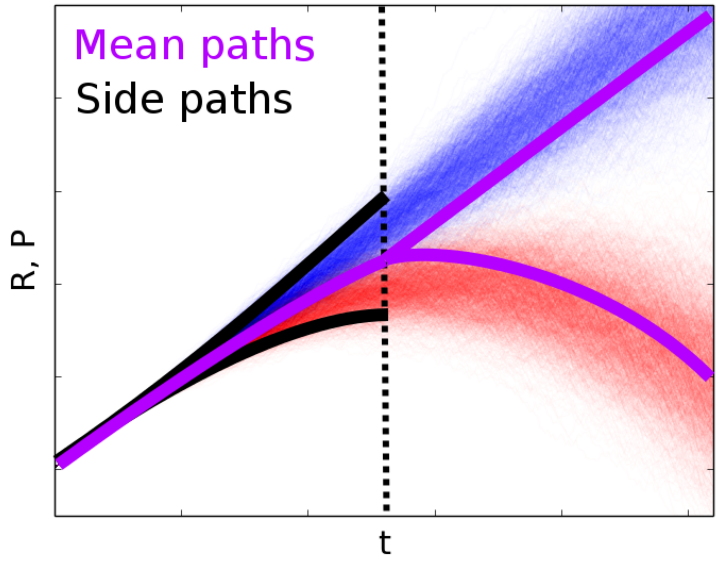

Figure 2.1: Schematic representation of the expected exact solutions of Eq. (2.6) (expressed as cascades) and the mean (SET) path as a representative (purple lines). The side paths running on the edge lines of the cascades are monitored for a short time (see text). The mean path is let branch when the side paths are significantly separated from each other.

energy summed up over all the branched paths are conserved.

First we consider the path 0 (SET path). The total Hamiltonian for the SET dynamics is

$$\begin{aligned} H_0\left(\mathbf{R},\mathbf{P}\right) &= \frac{\mathbf{P}^2}{2} + \frac{\left\langle \Phi(t)\right) \left| H^{(el)} \right| \Phi(t) \right\rangle}{\left\langle \Phi(t) \right| \left. \Phi(t) \right\rangle} \\ &= \frac{\mathbf{P}^2}{2} + \frac{\left\langle \left(D_1(t)\lambda_1(\mathbf{R}) + D_2(t)\lambda_2(\mathbf{R})\right) \left| H^{(el)} \right| \left(D_1(t)\lambda_1(\mathbf{R}) + D_2(t)\lambda_2(\mathbf{R})\right) \right\rangle_{\mathbf{r}}}{\left\langle \Phi(t) \right| \left. \Phi(t) \right\rangle}, \end{aligned} \tag{2.29}$$

where again the bra-ket inner product is to be performed over the electronic coordinates alone. Likewise the Hamiltonians to drive the path 1 and path 2 are, respectively,

$$H_K\left(\mathbf{R},\mathbf{P}\right) = \frac{\mathbf{P}^2}{2} + \frac{\left\langle \Phi_K(t)\right) \left| H^{(el)} \right| \Phi_K(t) \right\rangle}{\left\langle \Phi_K(t) \right| \left. \Phi_K(t) \right\rangle} = \frac{\mathbf{P}^2}{2} + \left\langle \lambda_K(\mathbf{R}) \left| H^{(el)} \right| \lambda_K(\mathbf{R}) \right\rangle_{\mathbf{r}} \tag{2.30}$$

for $K = 1, 2$. It is well established that the individual energy is conserved along each SET path.

Potential energy varied

In the force-state representation, we usually do not directly refer to the value of adiabatic potential energy surfaces. Therefore the potential energy that each path bears is to be estimated with integration of the force over a shifted distance. With the above Hamiltonian, Eq. (2.29) for path

0, let us write down the time-derivative of the momenta, that is, the forces as

$$\dot{\mathbf{P}}_0^k = -\frac{\left\langle (D_1(t)\lambda_1(\mathbf{R}) + D_2(t)\lambda_2(\mathbf{R})) \left| \partial H^{(el)}/\partial \mathbf{R}^k \right| (D_1(t)\lambda_1(\mathbf{R}) + D_2(t)\lambda_2(\mathbf{R})) \right\rangle_{\mathbf{r}}}{\langle \Phi(t) | \Phi(t) \rangle} \quad (2.31)$$

For the force eigenstates, the off-diagonal terms are close to zero, that is,

$$\left\langle \lambda_1(\mathbf{R}) \left| \partial H^{(el)}/\partial \mathbf{R}^k \right| \lambda_2(\mathbf{R}) \right\rangle \simeq 0, \quad (2.32)$$

and only the diagonal parts remaining in the expression as

$$\dot{\mathbf{P}}_0^k = -\frac{\left\langle D_1(t)\lambda_1(\mathbf{R}) \left| \partial H^{(el)}/\partial \mathbf{R}^k \right| D_1(t)\lambda_1(\mathbf{R}) \right\rangle_{\mathbf{r}} + \left\langle D_2(t)\lambda_2(\mathbf{R}) \left| \partial H^{(el)}/\partial \mathbf{R}^k \right| D_2(t)\lambda_2(\mathbf{R}) \right\rangle_{\mathbf{r}}}{\langle \Phi(t) | \Phi(t) \rangle}. \quad (2.33)$$

Similarly we have the forces for path 1 and 2, respectively, as

$$\dot{\mathbf{P}}_K^k = -\left\langle \lambda_K(\mathbf{R}) \left| \partial H^{(el)}/\partial \mathbf{R}^k \right| \lambda_K(\mathbf{R}) \right\rangle_{\mathbf{r}}. \quad (2.34)$$

for $K = 1, 2$.

The variation of the potential energy can be estimated rather directly with an elementary expression as

$$\Delta V_0 = \langle \Phi(t) | \Phi(t) \rangle \sum_k \int_{\mathbf{R}^k}^{\mathbf{R}^k + \Delta \mathbf{R}^k} \dot{\mathbf{P}}_0^k d\mathbf{R}^k. \quad (2.35)$$

Note that the population of the state to be carried by the path 0 is multiplied to the classical expression of the potential energy. Likewise, we have

$$\Delta V_K = |D_K(t)|^2 \sum_k \int_{\mathbf{R}^k}^{\mathbf{R}^k + \Delta \mathbf{R}^k} \dot{\mathbf{P}}_K^k d\mathbf{R}^k \quad (2.36)$$

for path K ($K = 1, 2$). For a time interval as short as Δt, $\Delta \mathbf{R}^k$ can be approximated to be

$$\Delta \mathbf{R}^k = \mathbf{P}^k(\mathbf{t}) \Delta t \quad (2.37)$$

irrespective of the kind of these paths. Collecting Eqs. (2.33) to (2.34) and Eqs. (2.35) to (2.36) altogether, we have

$$\Delta V_1 + \Delta V_2 = \Delta V_0, \quad (2.38)$$

which claims that the variation in the sum of the potential energies of path 1 and path 2 is the

same as that for path 0 in the first order.

Kinetic and total energies varied

Next we survey the variation of the kinetic energy. In the first order with respect to Δt, one can approximate as

$$\mathbf{P}(t+\Delta t) = \mathbf{P}(t) + \dot{\mathbf{P}}\Delta t, \tag{2.39}$$

which in turns give the first order expression of the kinetic energy as

$$\frac{1}{2}\mathbf{P}(t+\Delta t)^2 \simeq \frac{1}{2}\mathbf{P}(t)^2 + \mathbf{P}(t)\cdot\dot{\mathbf{P}}\Delta t. \tag{2.40}$$

Recalling here that at the branching time t all the momenta are taken equal, that is, $\mathbf{P}(t) = \mathbf{P}_0(t) = \mathbf{P}_1(t) = \mathbf{P}_{2.}(t)$, we compare only $\dot{\mathbf{P}}\Delta t$ terms. For path 0, it is

$$\begin{aligned}&\dot{\mathbf{P}}_0\Delta t \\ &= -\frac{\left\langle D_1(t)\lambda_1(\mathbf{R})\left|\partial H^{(el)}/\partial\mathbf{R}^k\right|D_1(t)\lambda_1(\mathbf{R})\right\rangle_{\mathbf{r}} + \left\langle D_2(t)\lambda_2(\mathbf{R})\left|\partial H^{(el)}/\partial\mathbf{R}^k\right|D_2(t)\lambda_2(\mathbf{R})\right\rangle_{\mathbf{r}}}{\langle\Phi(t)|\,\Phi(t)\rangle}\Delta t,\end{aligned} \tag{2.41}$$

while

$$\dot{\mathbf{P}}^k_K\Delta t = -\left\langle\lambda_K(\mathbf{R})\left|\partial H^{(el)}/\partial\mathbf{R}^k\right|\lambda_K(\mathbf{R})\right\rangle_{\mathbf{r}}\Delta t \tag{2.42}$$

for path 1 and path 2 with $K = 1$ and 2, respectively. The same arithmetic in the potential energy can be applied to the present case, and the result is

$$\mathbf{P}(t)\cdot\dot{\mathbf{P}}_0\Delta t\,\langle\Phi(t)|\,\Phi(t)\rangle = \mathbf{P}(t)\cdot\dot{\mathbf{P}}_1\Delta t\,|D_1(t)|^2 + \mathbf{P}(t)\cdot\dot{\mathbf{P}}_2\Delta t\,|D_2(t)|^2\,. \tag{2.43}$$

Therefore, in the first order, the kinetic energy is conserved as

$$\mathbf{P}_0(t+\Delta t)^2 = \mathbf{P}_1(t+\Delta t)^2 + \mathbf{P}_2(t+\Delta t)^2. \tag{2.44}$$

Thus, the total energy E_0 at the point $(\mathbf{R}(t), \mathbf{P}(t))$ with the population $\langle \Phi(t)| \Phi(t)\rangle$ is conserved as

$$E_0 = E_1 + E_2, \tag{2.45}$$

where E_K $(K = 1, 2)$ is the energy carreied by path K, whose population is $\langle \Phi_K(t)| \Phi_K(t)\rangle = |D_K(t)|^2$.

In summary the total energy at a branching point is to be partitioned in proportional to the populations of the to-be-branched paths, and each is carried in a manner to conserve their own energy. Note that these branching paths should be guided by the eigenforces. Under the conservation rule, the individual non-Born–Oppenheimer paths can thus penetrate into classically forbidden regions through nonadiabatic interactions.

2.2.6 Schematic illustration

Now that we know how the electronic population should be allocated to each path, we can consider qualitatively important cases within the framework of the path-branching theory. An illustrative schematic example is presented in Fig. 2.2: A path running on the lower potential surface comes in the interaction region and at some point below the top of the adiabatic potential (left white small circle) branches into two pieces, one with a smaller component but having a higher energy and the other of larger population whose energy is lowered a little to cancel the energy taken away by the counterpart. Note that these branched paths are continuously connected with each other at the branching point in phase space, although the higher energy path graphically seems to jump abruptly in the potential curve diagram. Therefore this continuous branching should not be confused with the surface-hopping motion. (Note also that although the adiabatic potentials are drawn in the figure in order to help imagination, but the dynamics are performed with use of the force diabatization.) The higher energy path can proceed to totally different course from the lower energy counterpart, and can bifurcate again at somewhere else (right white circle). So does the lower path. Thus even after many-time branchings, all the cascade paths can be continuously traced back to the original path with the total energy being conserved in the above sense.

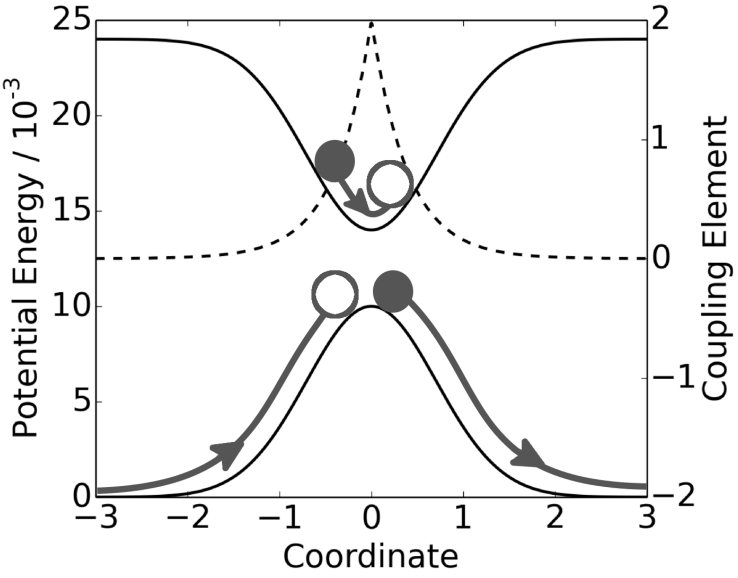

Figure 2.2: Schematic representation of energy conserving path-branching in configuration space. The branching paths are continuously connected in phase space.

2.3 Applications

2.3.1 Interactions and initial conditions

We apply the above algorithm to a model chemical reaction on one-dimensional, two-state interaction potential, which is constructed as follows: We first determine a pair of adiabatic potential energy curves (APEC) to be represented as

$$\epsilon_1(R) = V_{TS} \exp\left(-\left(\frac{R}{a}\right)^2\right)$$
$$\epsilon_2(R) = -\epsilon_1(R) + b, \tag{2.46}$$

where the parameters V_{TS}, a, b are set to $V_{TS} = 0.01$, $a = 1$ and $b = 0.024$ in atomic units, and thus the top of $\epsilon_1(R)$ is 0.01 while the bottom V_B of $\epsilon_2(R)$ is 0.014) As usual the matrix U

$$\mathrm{U} = \begin{pmatrix} \cos\theta(R) & \sin\theta(R) \\ \sin\theta(R) & -\cos\theta(R) \end{pmatrix} \tag{2.47}$$

transforms the APEC to diabatic potential energy curves (DPEC) with the coupling element X_{12} is given as

$$X_{12} = \frac{d\theta}{dR} = -X_{21}, \tag{2.48}$$

where the rotation angle θ as a function of R is given as

$$\theta(R) = \frac{\pi}{4}\left(2 - \exp\left(-\frac{4dR}{\pi}\right)\right), \quad \text{for } x \geq 0 \tag{2.49}$$

and

$$\theta(R) = \frac{\pi}{4}\exp\left(-\frac{4dR}{\pi}\right) \quad \text{for } x < 0, \tag{2.50}$$

where d is a parameter. We here set $d = 2$. The resulting APEC and DPEC are shown in Fig. 2.3. In this scheme therefore we can scan the intensity of the nonadiabatic coupling elements keeping the adiabatic potentials unchanged. We can thus uniquely define the total energy of the non-Born–Oppenheimer paths with respect to the height of the potential barrier V_{TS}.

The initial conditions are chosen so that the total energy of the path is comparable to the barrier height V_{TS}. The initial paths are generated on the ground state. The nuclear mass is set to $M = 1836$, mimicking a proton. The initial position to launch the paths is set at $R_0 = -9$, and let them start with a momentum $P_0 = \sqrt{2ME_0}$ and the total energy E_0 to the positive direction (from left to right in the figures). We here illustrate four typical paths:

1. $E_0 = 0.0080 = 0.8V_{TS}$: below the barrier top (V_{TS})
2. $E_0 = 0.0099 = 0.99V_{TS}$: close to the barrier top
3. $E_0 = 0.0125 = 1.25V_{TS}$: higher than the top (V_{TS}) and lower than the bottom of the excited state (V_B)
4. $E_0 = 0.0145 = 1.45V_{TS}$: a little higher than V_B.

2.3.2 Surmounting a potential barrier by lower energy paths

We begin with the branching dynamics of the two lower energy paths of $E_0 = 0.8V_{TS}$ and $E_0 = 0.99V_{TS}$. As suggested above, quantum paths can branch into the excited state even if the state energy is not classically accessible, the dynamics of which is caused by the electronic state mixing due to the derivative coupling X^k_{IJ}. The surface hopping model and the related theories

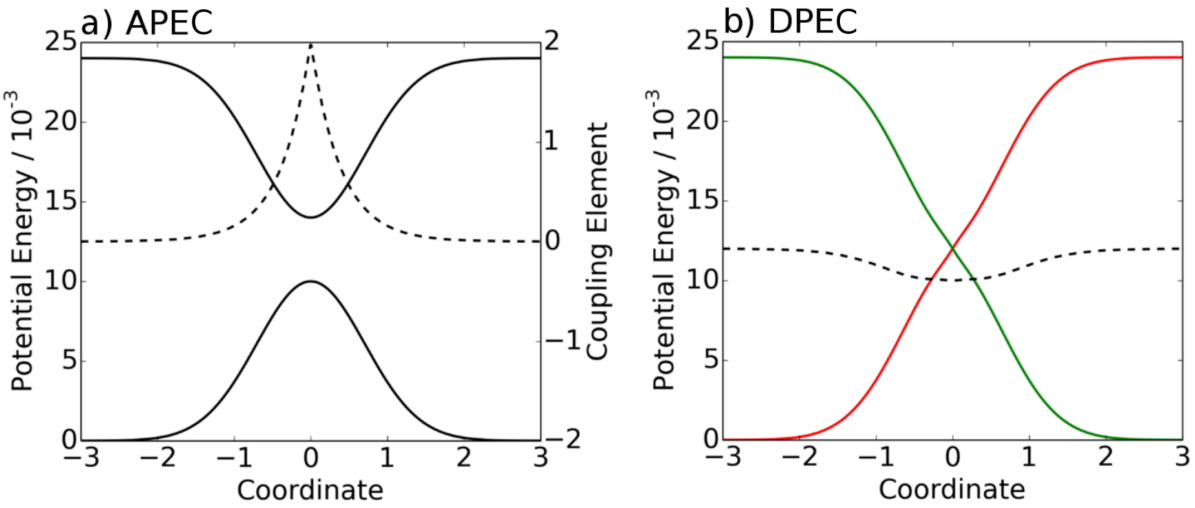

Figure 2.3: Potential energy curves versus the coordinate R. (a) Adiabatic representation. The solid lines denote APEC ϵ_i, while the dashed line does nonadiabatic coupling element X_{12}. (b) Diabatic representation. The solid lines represent the DPEC (red: V_{11}, green: V_{22}) and the dashed line shows the electronic coupling element V_{12}.

based on it would miss this phenomenon. The branch parameter Θ (see Eq. (2.25)) is set to 8 for the path of $E_0 = 0.8V_{TS}$ and to 7 for that of $E_0 = 0.99V_{TS}$. These parameters have been chosen to make the demonstrations clear.

As observed in Fig. 2.4, the paths come in and return to the reactant site with a large electronic-state population (the thicker is a curve, the larger is the associated population in the figure). However, in spite of the fact that the energy of these paths are lower than the barrier height, they begin to branch and some of the paths eventually reach the other side of the barrier. Inspection over this figure also shows that some other branched paths go back to the reactant site tracking the different routes from the parent one. Therefore, a part of the initial wavepacket is bifurcated and surmounts the barrier.

The paths that reach the other side of the barrier are assisted by the forces from the excited states. Let us focus on the path ending at around $t = 5 \times 10^3$ and $R = 1.5$ of Fig. 2.4(a). The precise history of this path is as follows. First, the path entered the interaction area with the first diagonal force (dominated by that of the ground state), and then at a branching point the path resumes to run driven by the second diagonal force (close to that of the excited state), and at the second branching point the driving force comes back to the first diagonal component. In this way the path could go over the barrier although it was classically forbidden.

The overall phenomenon effectively looks like the so-called deep tunneling. [40–45] How-

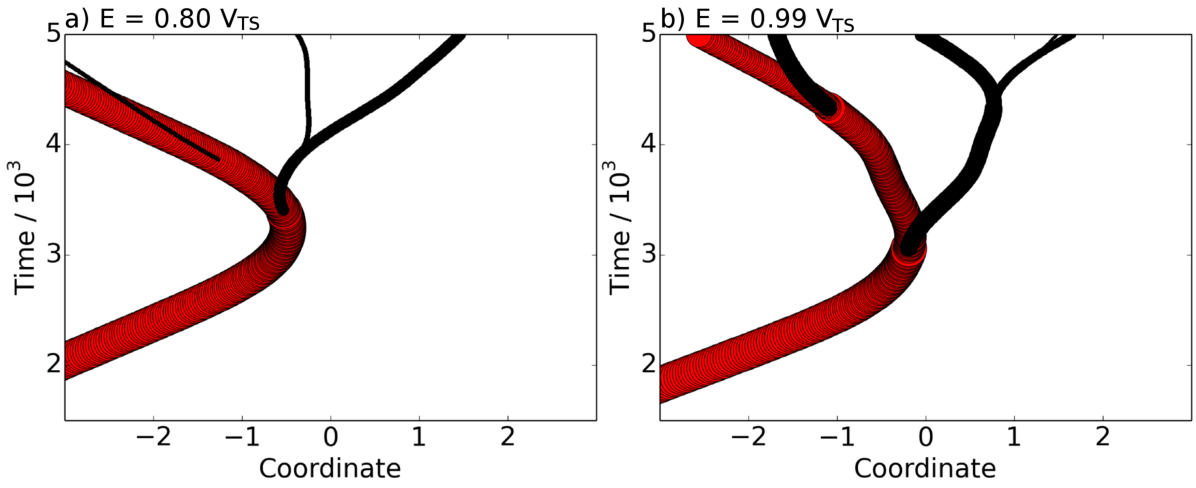

Figure 2.4: The branching paths of the total energy lower than the barrier height. The width of the paths is proportional to the square root of the electron population on the path. The paths in red (black) are driven by the forces mainly coming from the ground (excited) state.

ever, of course, they are independent phenomena. In the quantum deep tunneling, the paths go over the barrier through imaginary space and/or time, as in the instanton theory. [40] On the other hand, all the non-Born–Oppenheimer paths in this study are supposed to run in the real space, although the present theory of path branching can be generalized so that the paths can penetrate into complex spaces.

Another important difference between "surmounting" and "deep tunneling" is their dependences on the potential curves. Deep tunneling tends to be more effective as the potential barrier is thinner, while the nonadiabatic surmounting does not have such a simple characteristic. For instance, the path ending at $t = 5 \times 10^3$ and $R = 0$ in Fig. 2.4(b) is about to go back to the reactant side. If this path branches and get back to the ground state, it does not contribute to the increasing of reaction probability. Another difference is the time-delay of paths, which has nothing to do with the so-called tunneling time. We will return the problem of time-delay in the next section.

2.3.3 Trapping above the potential barrier

We next examine the case where the total energy is slightly higher than the barrier height, namely, $E_0 = 1.2V_{TS}$ (lower than the bottom of the excited state though) and $1.45V_{TS}$ (higher than the bottom too). Only to the last case, the surface hopping model can access. The branch parameter Θ (see Eq. (2.25)) is set to 5 and 4, respectively. As shown in Fig. 2.5, some paths are

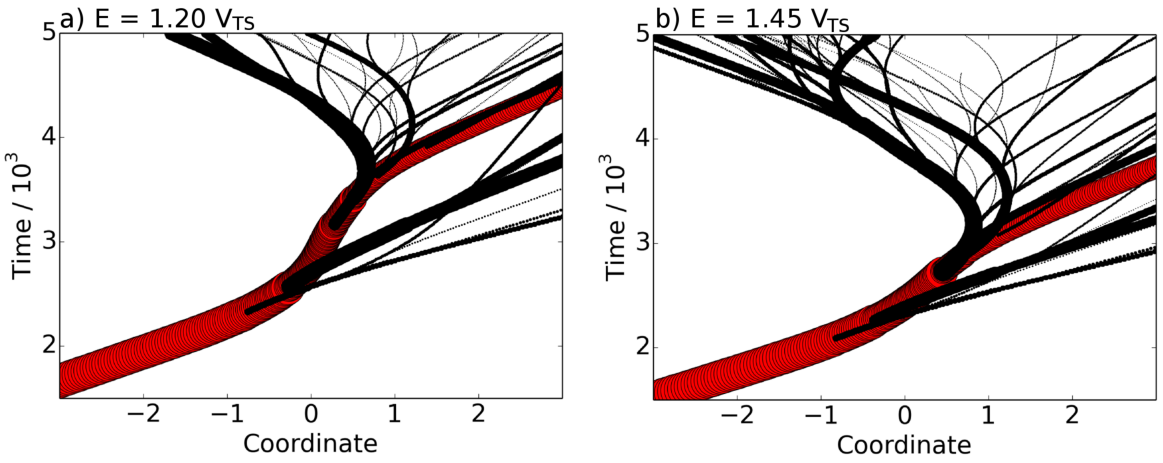

Figure 2.5: The same as Fig. 2.4, except that the branching paths have the total energy higher than the barrier height.

pushed back to the reactant side. These returning paths obviously work to reduce the reaction probability, and can be regarded as a friction to the reactive motions.

The precise mechanism is as follows. The paths come about the strong interaction area, where the electronic-state mixing is induced. The forces originated from the excited state trap some paths as though they undergo vibrational motion on the excited state adiabatic potential curve. However, again due to the nonadiabatic interactions, the trapped paths gradually spill out to the both ends of the potential barrier of the ground state. From the view point of chemical reaction therefore this delayed dynamics looks like a result of friction.

2.4 Full-quantum dynamics to verify the branching phenomena

We now proceed to confirm the physical picture drawn by the path-branching representation is consistent with the full-quantum results. Here in this chapter we compare the quantitative aspects of the phenomena observed above.

2.4.1 Method and initial conditions

The initial conditions for the quantum dynamics corresponding to those in the preceding section are first described. Suppose a total wavefunction $\Psi(R, r, t)$ is expanded as [77]

$$\Psi(R, r, t) = \sum_I \chi_I(R, t)\Phi_I(r; R), \tag{2.51}$$

where χ_I is a nuclear wavepacket on the adiabatic potential curve created by the electronic eigenstates $\Phi_I(r; R)$, which are assumed to be known beforehand. We propagate the nuclear wavepackets with the extended split operator method. [15] The initial nuclear wavepacket $\{\chi_I(R, t)\}$ is chosen to be a coherent-type Gaussian function on the adiabatic ground state as

$$\begin{aligned}\chi_1(R, 0) &= (\pi\Delta R^2)^{-1/4} \exp\left[-\frac{(R - R_0)^2}{2\Delta R^2} + i\frac{P_0 R}{\hbar}\right], \\ \chi_2(R, 0) &= 0.\end{aligned} \tag{2.52}$$

R_0 and P_0 are the same quantities as those defined in Sec. 2.3.1 for the path-branching representation. The wavepacket width in coordinate space is set to $\Delta R = 1$. The number of grid points for FFT is 512 on the space ranging from -32 to 32. Two absorbing imaginary potentials V_a are placed at the both ends, which are defined as

$$V_a(R) = -30i \exp\left(-\left(\frac{R \pm 20}{2}\right)^2\right). \tag{2.53}$$

V_a works not only to avoid the artificial reflection of the wavepackets from the boundaries but in the calculation of the reaction probability by integrating the absorbed components.

2.4.2 Time-delay induced by the trapping motion above the transition

The trails of the quantum wavepackets in (t, R)-coordinates are drawn in Fig. 2.6 left column, corresponding to the above four energies: (a) $E_0 = 0.008V_{TS}$, (b) $E_0 = 0.99V_{TS}$, (c) $E_0 = 0.0125 = 1.25V_{TS}$, and (d)$E_0 = 1.45V_{TS}$. The color chart in each diagram clearly indicates the wavepacket bifurcations, whose patterns are dependent on the energy.

In the right column, corresponding to each left panel, are depicted the square root of the population of the state ($|\Psi|$) that passes across the line $R = 9$ (red and solid curve, measured from right to left along the horizontal axis) and $R = -9$ (green and dashed curve, measured

from the left to the right) as a function of time. The former is proportional to the magnitude of $|\Psi|$ reaching the product area, while the latter represents that of the original reactant area. (We do not resort to the population $|\Psi|^2$ itself to prevent the small components from being invisible.)

In the lowest energy case, we can readily identify the packet components that are flowing out to the product site (of large positive R values). It is the usual practice that we attribute this seemingly leaking dynamics to deep tunneling. That this is not the case can be readily confirmed by running the full quantum dynamics without both the excited state and nonadiabatic coupling elements (simple dynamics on the ground state alone with the wavepackets whose average energies are lower than the barrier). It turns out that with this width of the potential barrier, the pure (deep) tunneling turned out to be virtually invisible, and the so-called shallow tunneling dominates (passing over the barrier by wavepacket components of energy higher than the barrier height). However, the presence of the nonadiabatically surmounting dynamics is clearly confirmed in terms of the time-delay components in the wavepacket dynamics, that is, shoulders of $|\Psi(9,t)|$ after the passage of the potential barrier (see Fig. 2.6, red curves after $t = 6$ in the right boxes of panels (a) and (b)). Such shoulders are more prominent in case of $E_0 = 0.99V_{TS}$ (panel (b)). The shoulders are seen not only in the graph of $|\Psi(9,t)|$ but in that of reflecting wave $|\Psi(-9,t)|$. Without the nonadiabatic coupling, the nuclear wavepackets would split into only two pieces and no those shoulders are found.

In the higher energy regime, the evidence of the tentatively vibrational motion in the excited adiabatic curve is clearly observed as the oscillatory structure around $R = 0$ in panel (d), left. The major component in this energy is found in the product site. A remarkable consequence of the tentative vibrational motion in excited state is a sequential appearance of pulse-train wavepackets with "time-delay", and the small shoulders arise from the delayed pulses. The time interval of the appearance of the pulses is approximately equivalent to the vibrational period of the excited state, although a complicated quantum interference gives rise to deviation from such a simple rule. This phenomenon of pulse-train is essentially equivalent to those observed by Zewail et al. in pump-probe experiments for the photodynamics of NaI. [78] However, the present dynamics arises from collision events starting from the ground state and therefore may give additional pieces of information about transition state and associated excited state if observed experimentally.

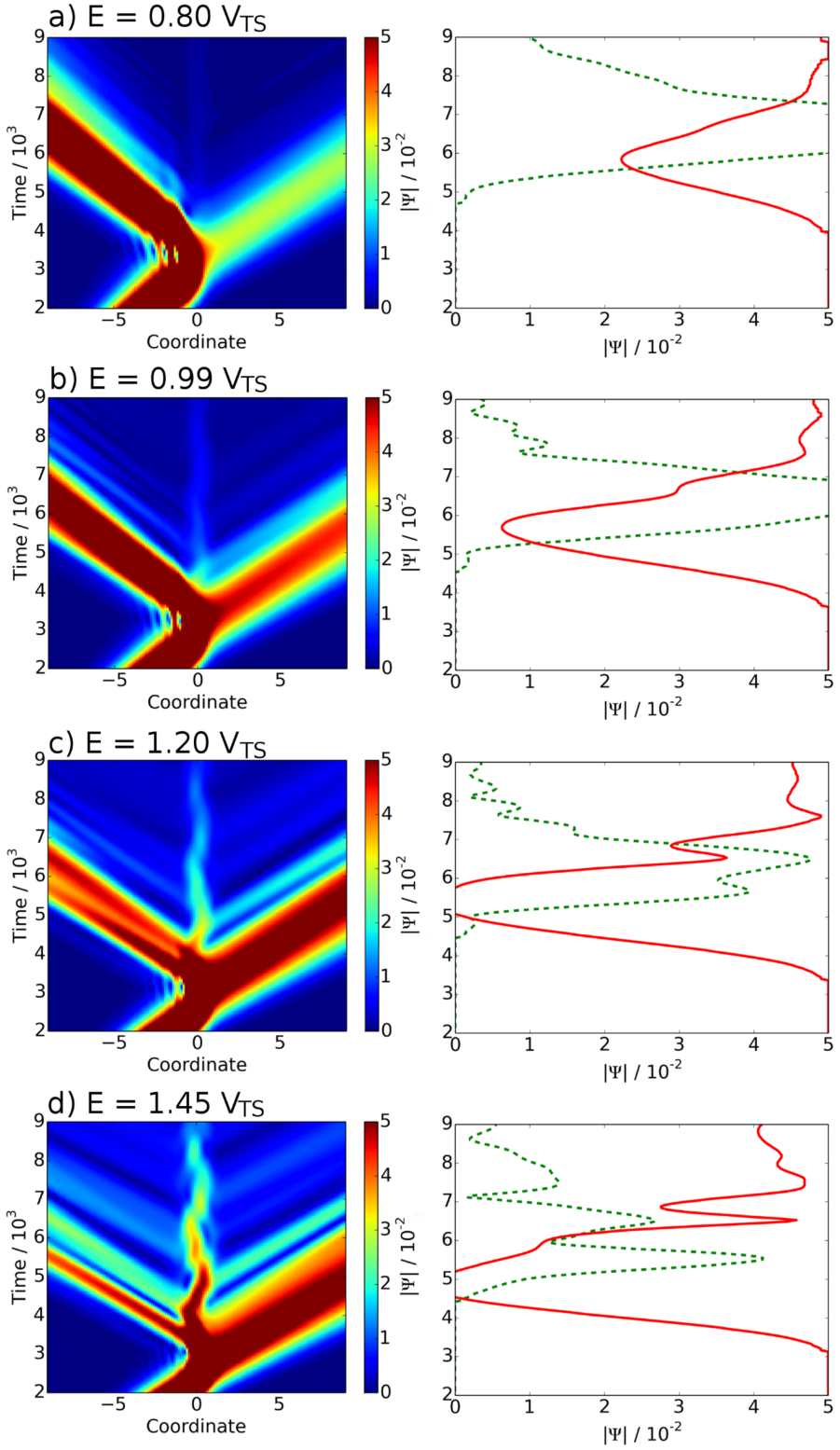

Figure 2.6: The reaction pathways in space-time for various total energies obtained from the full-quantum mechanics. The color maps on the left hand side are the plot of $|\Psi(R,t)|$. The plots on the right hand side are $|\Psi(R=9,t)|$ (solid line, measure to the left) and $|\Psi(R=-9,t)|$ (dashed line, measure to the right). The solid line is scaled as $|\Psi| = 2.5 \times 10^{-2}$.

2.5 Multi-dimensional implementation for molecular systems

2.5.1 Target system: $Mn(OH)OH_2\cdots$guanidine

Let us apply the theory of PBR to a multi-dimensional molecular system to confirm that the mechanism discussed above are not the characteristics of the one-dimensional system. We investigate the system of X-$MnOH_2\cdots$Ac in advance for this purpose, where X and Ac are an arbitrary subsystem and a proton-electron acceptor, respectively. In Chapter 3, we focus on only the mechanism of coupled proton-electron transfer in excited states of X-$MnOH_2\cdots$Ac for the sake of simplicity, rather than explicit path-branching that we do in this section.

Now we preview the mechanism of coupled proton-electron transfer found in the photodynamics of X-$MnOH_2\cdots$Ac, in which we consider the path-branching dynamics. Here the "photodynamics" denotes the nonadiabatic dynamics in excited electronic states accessed by means of direct photoexcitation. If the total energy allocated to the nuclear degrees of freedom is as much as that of zero-point oscillation, the most probable chemical reaction is H atom transfer between O and Ac, that is, interchange between [O-H$\cdots$Ac] and [O$\cdots$H-Ac].

In this section, we consider the case where X=OH and Ac=guanidine. The resulting molecule and projected one-dimensional coordinate relevant to the photodynamics are shown in Fig. 2.7. All the other candidates of X and Ac discussed in Chapter 3 have similar projected one-dimensional potential curves, thus we can probably find a similar path-branching dynamics among those systems. (See Fig. 2.7(a)). The projected one-dimensional potential curves have nonadiabatic region between S_3 and S_4.[*1] As we explain in Chapter 3, in the ground electronic state, this reaction is recognized as H^+ transfer. However, in the excited electronic states, the reaction mechanism is different from that of the ground state. This reaction is the coupled proton-electron transfer to induces charge separation on Ac, because H^{n+} and ne^- $(n \approx 0.6)$ reach spatially different places on Ac through mutually different pathways. The mechanism is discussed in detail in Section 3.3.

2.5.2 Further approximation for multi-dimensional molecular systems

If we perform full-dimensional on-the-fly calculations for the system of X-$MnOH_2\cdots$Ac, it is still difficult in terms of machine power to apply the side paths algorithm to such a system, because finite but a large number of paths need to be taken into account. For qualitative analysis

[*1] Here "S" denotes the excited electronic states in ascending order of energy.

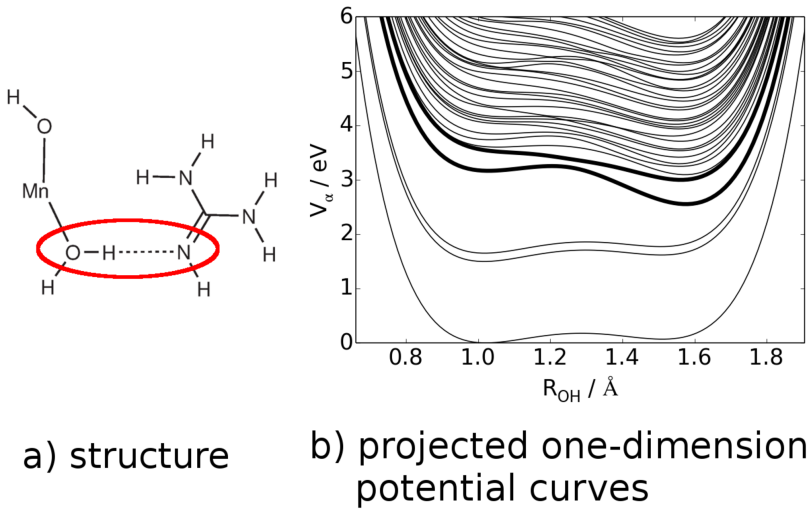

Figure 2.7: (a) The chemical structure of the target system $Mn(OH)OH_2 \cdots$ guanidine (the same as Fig. 3.2(a)). (b) Projected one-dimensional potential curves relevant to the chemical reaction under consideration, in which we perform multi-dimensional dynamics (the same as Fig. 3.4). The atoms in the red circle are mainly involved in the reaction.

as a starting point, we reduce the calculation cost by performing further approximation to the side paths algorithm.

We make the following assumptions about the side paths algorithm:

1. a set of adiabatic states can be used as an alternative set of of eigen force states.

2. the time when the momentum of the target degree of freedom is sufficiently small is the most appropriate to invoke path-branching.

The first assumption is also mentioned in Ref. [22] to say that the result with adiabatic states is similar to that with eigen force states. The second assumption can be justified with Fig. 2.2. We consider a case where a path has slightly lower energy than to surmount the potential barrier. It is anticipated that the path comes back to the reactant site after nonadiabatic transitions. If the side paths were running, they would split off from each other near the turning point. That is definitely when the momentum is sufficiently small. As shown later, the characteristic of the mechanism is preserved even by this rather drastic simplification, although the calculation cost is considerably saved.

2.5.3 Methods

The method for PBR photodynamics of $Mn(OH)OH_2 \cdots Ac$ that uses the further approximated algorithm is as follows:

1. Run the full-dimensional adiabatic dynamics in S_0 to obtain initial set of coordinates and momenta. The total energy allocated to nuclei is set to as much as that of zero-point oscillation.

2. Run the full-dimensional SET dynamics restarting in S_3 each 10 fs with the same coordinates and momenta as the adiabatic path at that time. We let the path integrated for further 10 fs.

3. Pick up a SET path that likely involves the tunneling-like effect induced by nonadiabatic transition. In other words, we find a SET path that cannot surmount the barrier, but undergoes adequate electronic state mixing.

4. Apply the algorithm discussed in Subsection 2.5.2 for PBR dynamics. Let each path integrated further 25 fs.

2.5.4 The tunneling-like effect induced by nonadiabatic interaction in the multi-dimensional system

Here we demonstrate that the tunneling-like effect induced by nonadiabatic interaction is indeed found in this multi-dimensional system. Internuclear distance between the O and H atoms $R_{\mathbf{OH}}$ along the adiabatic path in S_0 is shown in Fig. 2.8 as a dashed line. If $R_{\mathbf{OH}}$ becomes more than 1.3 Å, we can regard the path as experiencing the H atom transfer (See Fig. 3.4). Thus in the displayed time range, no H atom transfer takes place.

Solid (red) lines shown in Fig. 2.8 are corresponding to the SET paths restarted in S_3 at every 10 fs with the same coordinates and momenta at that time. We have four restarted paths and they can be classified into two groups. The first group contains paths restarting at $t = 10, 20$ fs, which reach almost the same points as those of adiabatic path (dashed line). The second group contains the others, which reach significantly different points. This difference stems from whether the path enters the nonadiabatic region. The paths in the second group undergo more than 20% of nonadiabatic transition as shown in Fig. 2.9. The path restarting at $t = 0$ fs comes back, while that restarting at $t = 30$ fs surmounts the barrier (H atom transfer). Following the method above, hereafter we focus on the path of $t = 0$ fs. The path would likely involve the tunneling-like effect induced by nonadiabatic interactions. We confirm it by calculating full-dimensional PBR dynamics.

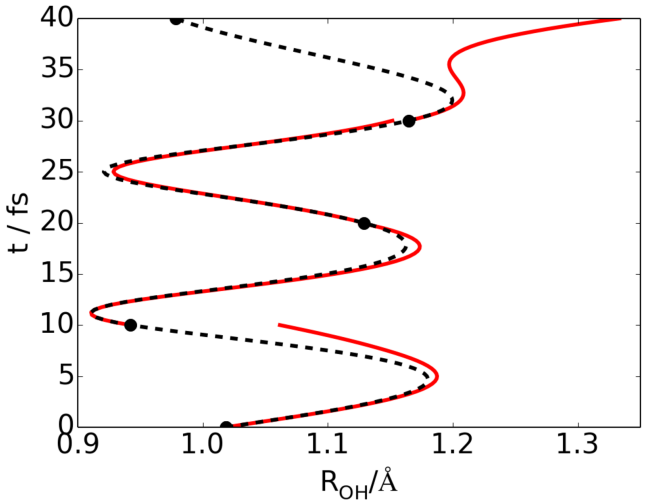

Figure 2.8: Time propagation of internuclear distance between the O-H bond of O-H$\cdots$Ac bonds (See Fig. 3.2(a)) along the path of full-dimensional dynamics. The dashed line is the path of adiabatic dynamics in S_0, while solid lines are the paths of SET dynamics restarting in S_3 each 10 fs with same coordinate and momenta as the path of S_0 at that time.

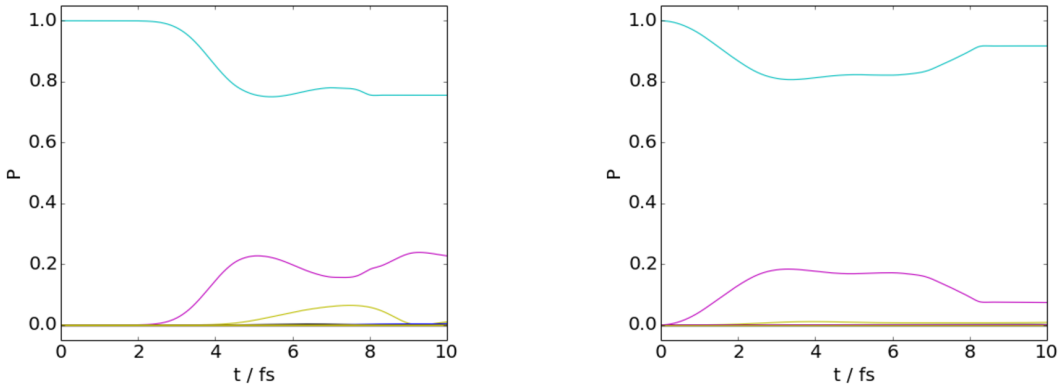

a) restarting at $t = 0$ fs

b) restarting at $t = 30$ fs

Figure 2.9: Time propagation of adiabatic state population along the SET path restarting at $t = 0$ fs (a) and $t = 30$ fs (b). Those lines are corresponding to S_3 (cyan), S_4 (magenta) and S_5 (yellow) in descending order of population. In both cases, more than 20% of nonadiabatic transitions occurs.

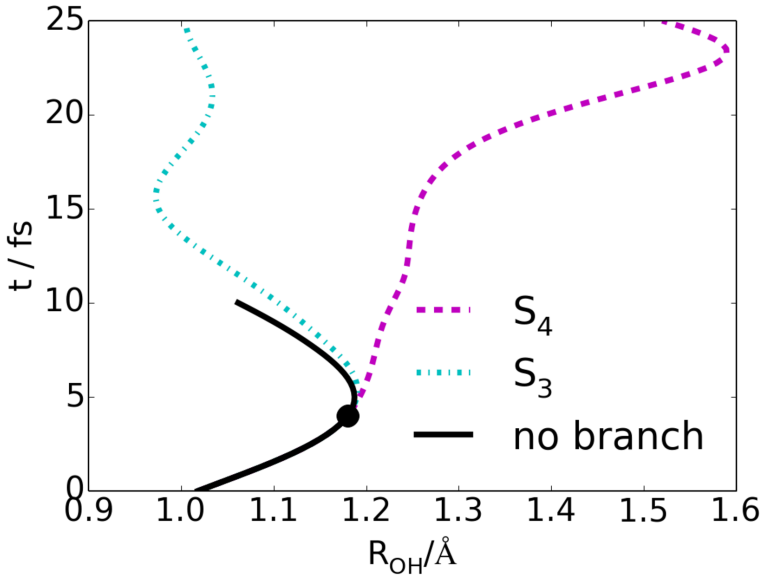

a) Time propagation of R_{OH}

b) O-H$\cdots$Ac (S_3)

c) O$\cdots$H-Ac (S_4)

Figure 2.10: Time propagation of R_{OH} on the branching paths (a) and resulting geometry and spatial distribution of unpaired electron density (Eq. (3.8)) from path-branching at $t = 4$ fs (b, c). (b) and (c) are corresponding to the geometries and unpaired electron densities equivalent to the restarting ones of S_3 and S_4, respectively.

The further approximated algorithm discussed in Subsection 2.5.2 is applied to the SET path restarting in S_3 at $t = 0$. The time to invoke path-branching is set to $t = 4$ fs, because the momenta of the transferred H atom is sufficiently small. That is when the side paths would be significantly apart from each other if they were running. We consider only the path-branching between S_3 and S_4, which undergoes relatively large nonadiabatic transition (See Fig. 2.9(a)). Path-branching is invoked only once for the sake of simplicity.

The branched paths shown in Fig. 2.10 obviously separate from each other. The path assigned to S_3 when the path-branching is invoked comes back to the reactant site, while that to S_4 eventually surmounts the barrier. The latter path is definitely the path of tunneling-like effect

induced by nonadiabatic interaction. In addition, electronic states along those paths are different from each other. We can clearly find the difference by using unpaired electron density $D(\mathbf{r})$, which is responsible for the radical character of an atom or a molecule. The unpaired electron density of each branching-path is also shown in Fig. 2.10. To sum up, the tunneling-like effect induced by nonadiabatic interaction can be indeed found even in this full-dimensional molecular system. The friction-like effect should also be found likewise. The SET path restarting at $t = 30$ fs is probably a good candidate for it.

2.6 Concluding remarks

We have developed an algorithm and computational practices for nonadiabatic path branching of non-Born–Oppenheimer trajectories in an energy region comparable to the barrier height of adiabatic potential energy curves in the theory of nonadiabatic electron wavepacket dynamics. The theoretical analysis on the practice has shown that individual branched paths due to nonadiabatic interactions can undergo classically forbidden phenomena, with the total energy of them being conserved. Using this algorithm, we have investigated the model chemical reactions that involve nonadiabatic couplings.

Two reaction mechanisms, namely, "surmounting" and "trapping above" the potential barrier have been discussed. They are also referred to as a tunneling-like effect and as friction-like effect induced by nonadiabatic interactions, respectively. The former takes place when the total energy of the path is lower than the barrier height, and the latter is observed when it is higher than the top. Although the surmounting phenomenon seems effectively similar to deep tunneling, [40–45] they are physically independent of each other and can happen simultaneously. Likewise, the present phenomenon of trapping above the transition state, which works as friction against chemical reaction, is independent of the kinematic effects arising from rotation-vibration coupling on a single potential surface [37] and the periodic bouncing motion in the transition state region [35, 36]. The solvent effect is also important in this regard, since solvent molecules surrounding a reactive system are known to work as friction against the passage across the transition state (see [79, 80] as early stage developments in this field and [81] for a review.) Therefore they can further couple in nonadiabatic systems.

The present chapter has been devoted to conceptual and phenomenological aspects of nonadiabatic transitions in chemical dynamics; path branching penetrating into classically forbidden

regions and time-delay dynamics in passing over the transition state. On the other hand, the method based on the path-branching representation can be readily extended to multi-dimensional systems to analyze more realistic chemical reactions, as we actually performed before. [3,8,20–29] Also, it can take account of external fields like laser or fluctuation due to solvents. Such studies are now under way.

Chapter 3

Photodynamics of OH dissociation and charge separation in X-$MnOH_2$

3.1 Introduction

An early process of photosynthesis, that is, photo-driven water oxidation to give protons, electrons and molecular oxygen,

$$2H_2O \rightarrow 4H^+ + 4e^- + O_2, \tag{3.1}$$

is now widely studied not only to understand photosynthesis itself, but also to find a guiding principle of solar cells and photocatalysts. This reaction is catalyzed by oxygen-evolving complex embedded in photosystem II (PSII), a membrane pigment-protein complex. [82] The key reaction is performed by the Mn_4CaO_5 cluster (the Mn cluster, in short) shown in Fig. 3.1 at the center of the oxygen-evolving complex. It is hypothesized that four photons are successively

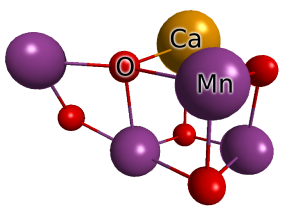

Figure 3.1: The structure of the Mn_4CaO_5 cluster (or the Mn cluster, in short) of the oxygen-evolving complex embedded in PSII.

absorbed by the oxygen-evolving complex to promote the redox states K_i ($i = 0 - 4$), [*1] which is called Kok cycle. [83–85] In this cycle, the oxygen-evolving complex is increasingly oxidized to K_4, and eventually it oxidizes H_2O to O_2 to get back to K_0. Surprisingly, no variations have been observed so far among oxygenic photosynthetic organisms. [86] In other words, only the Mn cluster can catalyze the photo-driven water oxidation in nature. This remarkable fact has already been reflected to artificial solar driven oxidation of water as a part of dye-sensitized solar cells. [87–90]

The Kok cycle was originally hypothesized in the context of flash-induced oxygen formation experiments, [85] which was a charge-accumulation model, that is,

$$K_0 \rightarrow K_1^{1+} \rightarrow K_2^{2+} \rightarrow K_3^{3+} \rightarrow K_4^{4+} \rightarrow K_0. \tag{3.2}$$

Each oxidation step is driven by photon absorption. The water decomposition is supposed to take place when the transition $K_4^{4+} \rightarrow K_0$ occurs. The redox state K is usually connected to the structure and the electron spin states, [86] thus following the change of structure and/or spin states of the oxygen-evolving complex in each redox state of the Kok cycle is frequently recognized as leading to solve the mechanism of water oxidation.

Many experimental efforts based on the hypothesized Kok cycle have been made to clarify the mechanism. Since the first X-ray crystal structure of PSII at $\sim$3.8 Å was published in 2001, [91] the resolution of the crystal structure has been improved in a gradual manner. [92–94] In 2011, Shen, Kamiya and coworkers reached atomistic resolution (1.9 Å), [82, 95] which is known to be a breakthrough. Structural analysis has also been performed by extended X-ray absorption fine structure (EXAFS), [96–100] which enables us to follow the structural "changes" among redox states. Electron paramagnetic resonance (EPR) [101] is performed to identify the spin state of Mn. Fourier transform infrared spectrum (FTIR) is also available for the structural analysis. [102, 103]

As for theoretical aspects, this problem is usually tackled by means of energetics with stationary state quantum chemistry. Most studies are again based on the hypothesized Kok cycle. With the help of rapid developing of massive computation, the system under consideration is becoming larger and larger. Most of the approaches of stationary state quantum chemistry depend on density functional theory (DFT), which can reproduce a structure obtained experimentally

[*1] "S" is usually used to represent the redox states of the Kok cycle, but here we use "K" to reserve it for representing electronic states later.

by X-ray diffraction (XRD). [104–111] Yamaguchi and coworkers have performed systematic geometry optimization to find reaction paths. [110, 112–118] They pointed out that the geometry in K_2 and K_3 can be altered compared to K_0 and K_1. Siegbahn has similarly calculated energy diagram of the Kok cycle by using DFT. [104–107] The suggested mechanism is that the optimal O-O bond formation occurs between an oxygen radical and an oxo ligand, or alternatively, the oxygen radical reacts with an external water. In contrast, Kurashige performed density matrix renormalization group (DMRG) [119–121] to determine the near-exact many-electron wavefunctions corresponding to the XRD structure of the oxygen-evolving complex. Through the analysis of the wavefunctions in the K_2 state, their direct access to spin states and spin projections suggests that existing candidates must be reassessed. He also performed multi-state calculations, and find a nonadiabatic region.

In spite of both experimental and theoretical efforts, the mechanism of the early process of photosynthesis is still a matter of controversy [86, 116, 122, 123]. Now let us recall the water oxidation reaction (3.1). The reaction is driven by photoexcitation of electronic states (visible light absorption), and such excited states can never be stationary. In this way, the mechanism can be beyond the scope of the Born–Oppenheimer approximation, although even all atom molecular dynamics simulation of PSII has been reported [124] base on this approximation. Therefore, electron dynamics should play an important role in the early process of photosynthesis. However, such a dynamical property has never been addressed in the system relevant to the oxygen-evolving complex.

Electron dynamics has been proved to produce insight into chemical reactions. Ushiyama and Takatsuka have performed electron wavepacket dynamics of H atom transfer in the system of ground and excited states of $H_2O + H_3O^+$. [125] They found a dynamical difference between these states, although the transferred H nucleus moves in the same way. In the ground state, $H^{0.5+}$ is transferred, while in the excited states, a H radical is. We can even track pathways of electrons in a chemical reaction in terms of Schiff probability current [126] (flux, in short). Nagashima and Takatsuka calculated nonadiabatic electron wavepacket dynamics of phenol-ammonia cluster in excited electronic states. [11] The result clearly shows the importance of electron dynamics to understand the mechanism of chemical reactions. They demonstrated that when the H nucleus was transferred from the phenoxy group to the ammonia cluster, approximately 0.5 electrons were bonded to the transferred H nucleus, and the rest of electrons ($\sim$0.5) took different pathways from the H nucleus. In addition, the electron reached spatially different

places on the ammonia cluster to naturally induce charge separation. This result can be regarded as a prototype mechanism of charge separation in excited states.

In this study, we calculate photodynamics of water decomposition by means of nonadiabatic electron wavepacket dynamics theory. Here the "photodynamics" denotes the nonadiabatic dynamics in excited electronic states accessed by means of direct photoexcitation. We approach this problem with two steps. First we perform analysis in the projected one-dimensional coordinate relevant to the photochemical reaction dynamics to grasp the landscape. And then we calculate full-dimensional nonadiabatic electron wavepacket dynamics to propose photodynamical mechanism related to charge separation. The target system is chosen to be X-$MnOH_2\cdots$Ac. Here X and Ac are respectively an arbitrary subsystem and a proton-electron acceptor such as guanidine and ammonia cluster. We are stimulated to examine the systems by the Mn cluster of the oxygen-evolving complex, where such a charge separation by using photon energy must be crucial. The oxygen-evolving complex is far more intricate than the systems under consideration in this thesis, thus the present calculations are not regarded as simulations. Rather than that, our purpose is to extract important partial systems to find a key component of the mechanism.

We propose a photodynamical mechanism resulting in charge separation, which is similar to that of the phenol-ammonia cluster system proposed in a different context. The characteristic of this mechanism is that protons and electrons are transferred to mutually different places on the acceptor through difference pathways. In addition, we investigate such dynamics of molecules including a Ca atom, which is known to be an essential cofactor for the Mn_4CaO_5 cluster of the oxygen-evolving complex. [127] We find resemblances and differences in the photodynamical mechanism to suggest the possible roles of the Ca atom. In connection with the oxygen-evolving complex, we calculate the same properties in the projected one-dimensional coordinate relevant to the full-dimensional dynamics. The result indicates that the same photodynamical mechanism can be found even in the Mn cluster of the oxygen-evolving complex. This study takes the first step of electron dynamics in the system relevant to the oxygen-evolving complex embedded in PSII.

The present chapter is organized as follows. In Section 3.2, we state the methodology used in this chapter. In Section 3.3, we propose a photodynamical mechanism to induce charge separation through nonadiabatic electron dynamics. In Section 3.4, roles of Ca in PSII are addressed in this context. In Section 3.5, possibility of the present mechanism in the Mn cluster of the oxygen-evolving complex is considered. In Section 3.6, we mention the alternative mechanism,

namely, electron attachment. Section 3.7 concludes this chapter.

3.2 Methodology

3.2.1 On-the-fly dynamics of the semiclassical Ehrenfest theory (SET)

We calculate nonadiabatic electron wavepacket dynamics in the level of theory equivalent to the semiclassical Ehrenfest theory (SET) to the first order. Here we do not consider explicit path-branching for the sake of simplicity, but we have presented it in part in Section 2.5. The theory is derived from the path-branching representation [3, 8, 20–28] by means of wavepacket-averaging of the force operator $\hat{\mathcal{F}}^k$. Theoretical details have already been discussed in Chapter 2, thus here we rewrite only the resulting equations.

The electron wavepacket is expanded in the form

$$\Psi_{\rm elec}(\mathbf{R}, \mathbf{r}, t) \quad = \quad \sum_I C_I(t)\Phi_I(\mathbf{r}; \mathbf{R}(t)). \tag{3.3}$$

The electron wavepacket follows the equation of motion expressed as

$$i\hbar\frac{dC_I}{dt} = \sum_J \left(H_{IJ}^{(el)} - i\hbar\sum_k \dot{R}_k X_{IJ}^k - \frac{\hbar^2}{2}\sum_k Y_{IJ}^k \right) C_J, \tag{3.4}$$

and a nuclear path is classically driven by the wavepacket-averaged force F_k defined as

$$F_k \quad = \quad \langle\Psi|\hat{\mathcal{F}}^k|\Psi\rangle = \sum_{IJ} C_I^*\langle\Phi_I|\frac{\partial\hat{H}^{(el)}}{\partial R_k}|\Phi_J\rangle C_J. \tag{3.5}$$

In the present chapter, Y_{IJ}^k (a correction term for intuitively derived SET [22]) is neglected in all the calculations for the sake of computational cost, which should be justified because of the factor $\hbar^2$.

In this study, those equations are numerically integrated with the matrix elements calculated on-the-fly. The nuclear (classical) equation of motion using the mean force in Eq. (3.5) is numerically integrated by using the velocity Verlet method with the time step of $\frac{0.25}{3}$ fs. The electronic equation of motion (3.4) is also numerically integrated by means of the Adams method with automatically controlled time step width, which is usually 10-100 attoseconds. The matrix elements are updated at the same interval as nuclei for the sake of calculation cost, and assumed

to be constant in the meantime. It is justified because the amount of changes in matrix elements are much smaller than that of $\{C_I(t)\}$.

Evaluation of derivatives of the matrix elements such as $\frac{\partial H_{IJ}^{(el)}}{\partial R_k}$ or X_{IJ}^k takes so much longer time of all the calculations involved, thus it is regarded as a bottle neck. In order to increase the overall speed of computation, we implemented a framework to perform parallel computation of numerical derivatives. We discuss technical detail in Appendix A.

3.2.2 Adiabatic wavefunctions as a basis set

In the present work, the basis functions of the electron wavepacket $\{\Phi_I(\mathbf{r};\mathbf{R}(t))\}$ shown in Eq. (3.3) are chosen to be adiabatic wavefunctions $\{\Phi_\alpha(\mathbf{r};\mathbf{R}(t))\}$ obtained on-the-fly through quantum chemical calculations. The adiabatic wavefunctions and relevant matrix elements are calculated by using modified GAMESS programming package. [128, 129] We perform CISD/RHF level of calculation for all the static and dynamical analysis, except for geometry optimization and following Hessian matrix evaluation (RHF level). Effective core potential is adopted for Mn atom, and 6-31G basis set is for all other atoms. We added diffuse orbitals to the H and N atoms, which are crucial for expressing the present mechanism. [11] Those to the other atoms are omitted to reduce the cost and unstability of computation, but it does not cause qualitative difference. Configuration state functions (CSFs) are generated by means of the graphical unitary group approach (GUGA). [130–136] Only the HOMO to (HOMO+50) are taken into account to generate CSFs, and all other orbitals are "frozen". We "froze" HOMO-1 and lower MOs, since the energy gap between HOMO and HOMO-1 is quite large (commonly more than 2 eV). MOs higher than HOMO+51 are not always far away from HOMO+50 in energy, but they can be "frozen" because the resulting low-lying adiabatic states are sufficiently converged without these higher MOs. We use first 50 of the adiabatic states $\{\Phi_\alpha\}$ out of 1326 in ascending order of energy as the basis set $\{\Phi_I\}$ of electron wavepacket in Eq. (3.3).

Technically speaking, such an adiabatic basis set is not always continuous in a series of time, which can cause a failure in computation. So as to avoid it, we transform the basis set at each time step so that the neighboring basis sets are smoothly connected by using the overlap between them. The method is discussed in Appendix B in detail.

3.2.3 General settings of the target molecular system: X-$MnOH_2\cdots$Ac

We investigate the system expressed as X-$MnOH_2\cdots$Ac, where X and Ac are an arbitrary subsystem and a proton-electron acceptor, respectively. Thus X-$MnOH_2$ serves as a proton-electron donor as we see in the rest of this chapter. In the present study, X is chosen to be one of the three subsystems, namely, OH, O(Ca)H or Mn_3CaO_5. The choice has a specific purpose as

OH: The simplest system to demonstrate the mechanism in detail.

O(Ca)H: A Ca adduct to find the roles of Ca in comparison with X=OH.

Mn_3CaO_5: The system of the same composition as the Mn_4CaO_5 cluster in PSII.

On the other hand, the choice of Ac generally does not affect the present mechanism on the whole. Ac is chosen to be one of guanidine, imidazole, ammonia cluster, or *N*-methylformamidine. The last one is used only for X=O(Ca)H, because it produces almost the same structure of X-$MnOH_2\cdots$Ac irrespective of the existence of the Ca atom. Ac=ammonia cluster is a similar setting to the previous study — phenol-ammonia cluster system. [11] The other Ac's, guanidine and imidazole, come from parts of positively charged proteinogenic amino acids. The partial systems are the edge of the amino acid residues that bring about basicity.

We focus on the H atom of O-H$\cdots$Ac bonds in the excited electronic states, which is involved in the low energy (in terms of nuclear degrees of freedom) chemical reactions. We calculate properties in the projected one-dimensional coordinate relevant to such a reaction for all the target systems, and full-dimensional nonadiabatic electron wavepacket dynamics for some systems that can be handled in terms of machine power available.

3.3 Photodynamical mechanism resulting in charge separation

3.3.1 Target system: X=OH, Ac=(guanidine, imidazole, or ammonia cluster)

Here we consider photodynamics of X-$MnOH_2\cdots$Ac, where X=OH and Ac=(guanidine, imidazole, or ammonia cluster). The resulting chemical structures are shown in Fig. 3.2.

Without Ac, that is, if the $Mn(OH)OH_2$ exists alone, the Mn(OH)O(H)-H bond is stronger than the Mn(OH)-OH_2 bond. Here the hyphen "-" denotes the bond to be compared. In short,

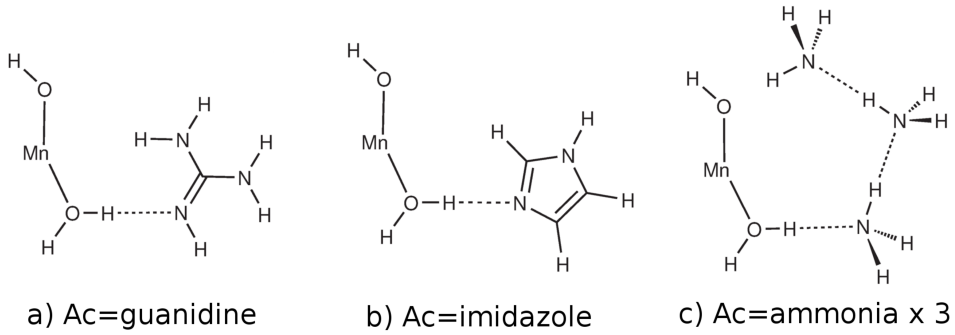

Figure 3.2: The chemical structures of target molecules for full-dimensional photodynamics. $Mn(OH)OH_2$ is in common and Ac is different from each other. They commonly have O-H$\cdots$Ac bonds, which is relevant to the mechanism proposed in this study.

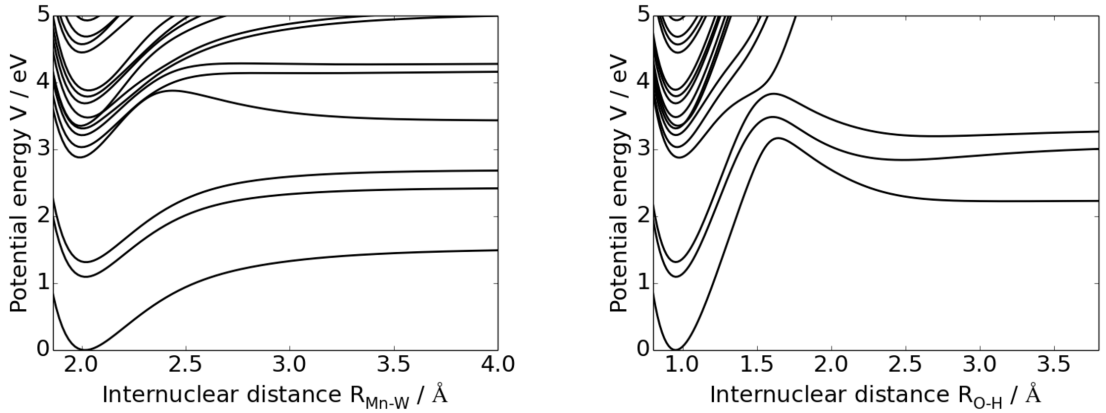

Figure 3.3: Potential curves as functions of bond length denoted by hyphen "-". (a) MnO bond, (b) OH bond of the water molecule. The former is weaker than the latter in this condition, but the relation is reversed if the accepter is attached (see Fig. 3.2).

OH and MnO bonds are compared. Potential curves as functions of the corresponding bond length is shown in Fig. 3.3. Here all other geometries are fixed to the optimized geometry. The OH bond is stronger than the MnO bond in this condition, but the relation is reversed if the acceptor is attached. In other words, OH bond of the water molecule is significantly weakened as a result of linkage to Ac.

3.3.2 Properties in the projected one-dimensional coordinate

Before full-dimensional dynamics, we investigate properties in the projected one-dimensional coordinate relevant to the following full-dimensional dynamics. The chemical reaction that occurs in the full-dimensional dynamics can be well explained by using this coordinate. The projected one-dimensional coordinate is defined as the position of the H atom connecting O and

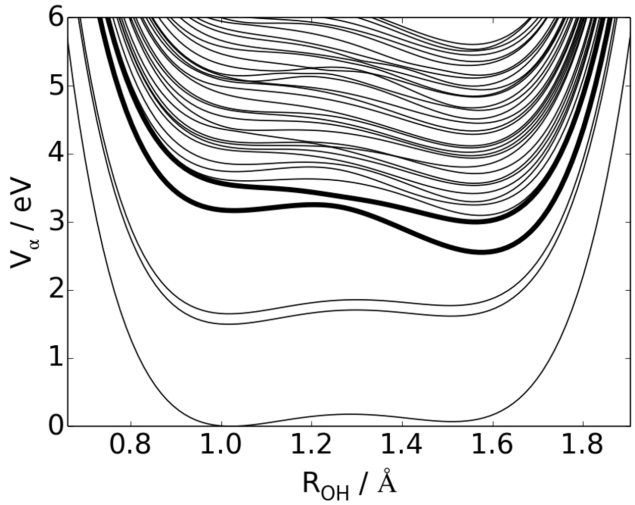

Figure 3.4: Adiabatic potential curves as functions of position of the transferred H atom for $Mn(OH)OH_2 \cdots$ guanidine. S_3 and S_4 are drawn as thick lines, which are the states that electrons mainly populate in excited state in our analysis.

Ac, that is, the H atom of the O-H$\cdots$Ac bonds (See Fig. 3.2). We call the H atom "transferred H atom" to distinguish it from the other relatively stable H atoms. All other atoms are fixed to the optimized geometry. The transferred H atom is restricted to be on the line connecting O and Ac. The O-Ac length is commonly as long as 2.5 Å. No further optimization is performed for the sake of simplicity. We can obtain similar properties, and find the same mechanism among those acceptors shown in Fig. 3.2, thus here we demonstrate only the case where Ac=guanidine (Fig. 3.2(a)).

Here we focus on differences between S_0 and the set (S_3, S_4) in the one-dimensional coordinate. In what follows, "S" denotes the adiabatic states in ascending order of energy. Note that it is not used for the redox states of Kok cycle. Those excited states are accessible by means of photoexcitation, because the transition dipole between S_0 and (S_3, S_4) is relatively large. On the other hand, that between S_0 and (S_1, S_2) is very small. Adiabatic potential curves in this coordinate is shown in Fig. 3.4. The focused excited states (S_3, S_4) are represented as thick lines there. We can find three characteristic differences as explained below.

The first difference is the position of the minimum in the one-dimensional potential curves. While the minimum of the S_0 in this coordinate is on the O atom side (left hand side), those of (S_3, S_4) are on the Ac side (right hand side). This indicates that the structure having the H atom on the Ac side is energetically more favorable in those excited states.

The second difference is the existence of nonadiabatic region (See thick lines in Fig. 3.4).

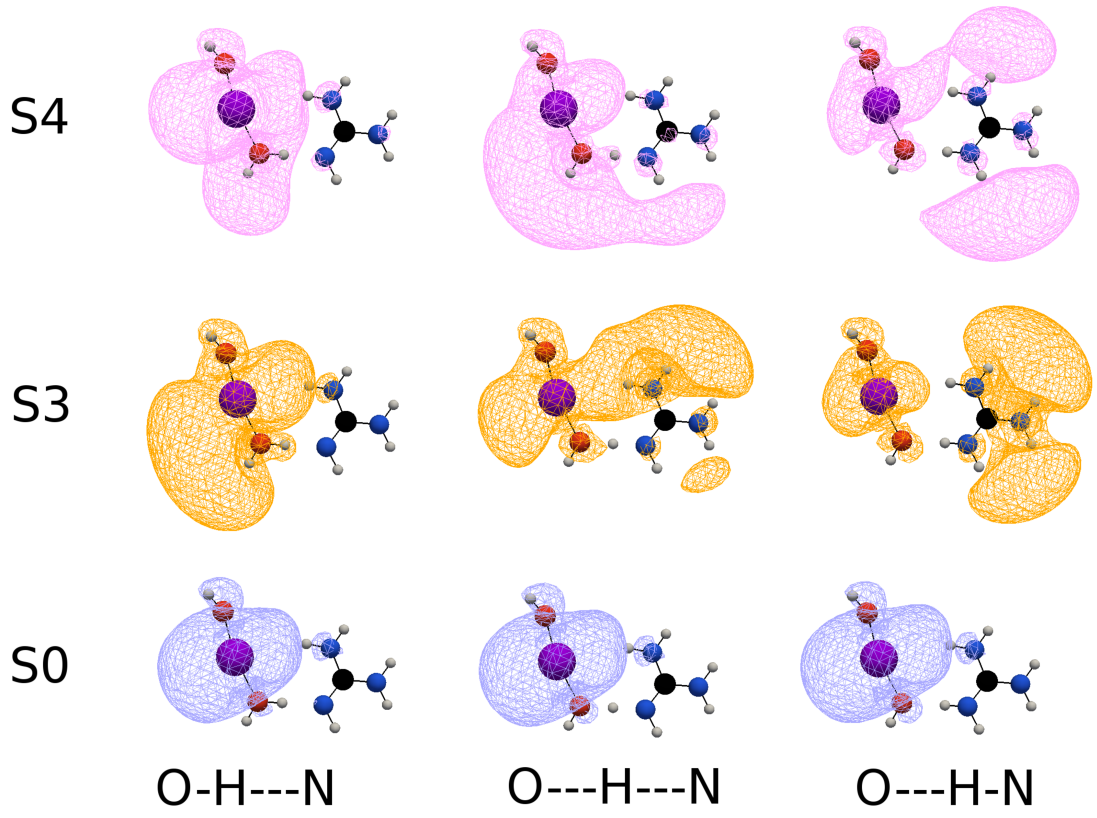

Figure 3.5: Spatial distribution of the sum of electrons occupying natural orbitals whose occupation number is less than two for $Mn(OH)OH_2 \cdots$ guanidine. The colors are attributed to atoms as follows: H=white, C=black, N=blue, O=red and Mn=purple. Those electrons are responsible for the differences among electronic states, thus here referred to as "responsible electrons". The row denotes the position of transferred H atom, while the column does the adiabatic states S_0, S_3 and S_4. Those of S_1 and S_2 are similar to that of S_0. We can find the Rydberg-like diffused states only in the excited states.

Drastic change of electronic states would take place near the avoided crossing at $R_{\mathrm{OH}} = 1.25$ Å, where R_{OH} denotes the OH bond length in the one-dimensional coordinate. This avoided crossing looks more like a conical intersection according to the situation, and we can probably find such conical intersection if we do not restrict the H atom on the O-Ac line.

The third difference is the spatial distribution of electrons. We show the spatial distribution of the sum of electrons occupying natural orbitals whose occupation number is less than two in Fig. 3.5. Those electrons are responsible for the differences among electronic states, thus here referred to as "responsible electrons". This difference is particularly significant, because it characterizes the H atom transfer in S_0 and (S_3, S_4). In S_0, the spatial distribution of responsible electrons is kept almost unchanged to be on $Mn(OH)OH_2$ regardless of the position of the transferred H atom. Thus the H atom transfer in S_0 should be recognized as ordinary proton transfer, which is equivalent to common acid-base reaction. No charge separation on Ac is

induced by this reaction in S_0. On the other hand, spatial distribution of responsible electrons in (S_3, S_4) depends on the position of the transferred H atom. Since the responsible electrons follow the transferred H atom, the H atom transfer in those excited states is termed "coupled proton-electron transfer", which is originally termed in Ref. [11]. It should be distinguished from H radical transfer, although it appears to be so. We also discuss this difference in detail in the dynamics part (Subsec. 3.3.4).

3.3.3 Postulated mechanism of the coupled proton-electron transfer

From those one-dimensional static analysis, we can think of the reaction expressed as

$$\text{X-MnOH}_2 + h\nu \rightarrow \text{X-MnOH} + \text{H}^{n+} + n\text{e}^- \qquad (0 < n \leq 1). \tag{3.6}$$

In this reaction, photon energy is utilized for charge separation. The postulated mechanism of this reaction is as follows:

1. Excited electronic states are generated by UV-visible light.

2. H^{n+} is transferred to the acceptor (Ac) through nonadiabatic region.

3. $n\text{e}^-$ are transferred to the Rydberg-like states of Ac (see Fig. 3.5) through different pathways from that of H^{n+}.

We emphasize that this mechanism results in charge separation on Ac, because H^{n+} and $n\text{e}^-$ reach different places on Ac through mutually different pathways. The step 2 and 3 are not necessary to occur sequentially, but they can take place at the same time, or even in the reversed order.

Until the present work, this kind of mechanism (coupled proton-electron transfer that results in charge separation on an acceptor) had been appeared only in the literature of phenol-ammonia cluster. [11] However, the mechanism was not discussed explicitly in the context of solar cells or photocatalysts, because the excitation energy was as much as 6 eV (200 nm). Additionally, only the set of phenol and ammonia clusters are discussed as a set of proton-electron donor and acceptor. Thus our study can be recognized as relevant generalization of the mechanism so as to be applicable in the context of solar cells and photocatalysts, with relatively various set of proton-electron donor and accepters.

3.3.4 Full-dimensional dynamics following the mechanism

Initial conditions

Now we proceed to full-dimensional dynamics so as to confirm that the dynamics indeed follows the postulated mechanism. We consider only $Mn(OH)OH_2 \cdots$ guanidine (Fig. 3.2(a)), but the other acceptors shown in the Fig. 3.2 result in the same in quality. Before the dynamics in excited states, completely adiabatic dynamics of zero-point oscillation in S_0 is integrated for 250 fs to obtain a set of initial conditions assigned to nuclear coordinates and momenta. We pick initial conditions every 10 fs from the path, and lift up the electronic wavepacket to S_4. We integrate SET dynamics for each path restarted in the excited state.

The energy allocated to the transferred H atom is as much as the barrier height located in the projected one-dimensional coordinate (see Fig. 3.4). The total energy of nuclei is 3.3 eV, which is corresponding to the total energy of zero-point oscillations. We can estimate the momenta P_{H} of the transferred H atom projected to the line connected to O and Ac as

$$P_{\mathrm{H}} = \mathbf{P}_{\mathrm{H}} \cdot \frac{\mathbf{R}_{\mathrm{Ac}} - \mathbf{R}_{\mathrm{O}}}{|\mathbf{R}_{\mathrm{Ac}} - \mathbf{R}_{\mathrm{O}}|} \tag{3.7}$$

to appraise the energy allocated to the one-dimensional coordinate, which is turned out to be 0.05 eV on average. This energy is comparable to the barrier height of the proton transfer in S_0. This is reflected in the adiabatic path in S_0. The OH length along the path in S_0 is shorter than 1.3 Å (OH bond is retained) until $\sim$100 fs, but it turns to longer than 1.3 Å (OH bond is broken to generate H-Ac bond).

Excitation to S_4 increases reactivity compared to S_0

As we predicted in the analysis in the projected one-dimensional coordinate, the relevant H atom becomes easy to be transferred to Ac if excited to S_4. The internuclear distance R_{OH} between the transferred H atom and the nearest O atom along the path is shown in Fig. 3.6. The projected one-dimensional potential curves (Fig. 3.4) would help us understand it. Let us regard the transferred H as being on the O atom side if $R_{\mathrm{OH}} \leq 1.3$Å (left hand side), and Ac side if $R_{\mathrm{OH}} > 1.3$Å (right hand side).

First we focus on the path in S_0, which is represented as a dashed line in Fig. 3.6. While $t < 100$ fs, the H atom is on the O atom side. Then it moves to the Ac side to stay there during $100 < t < 250$ fs (it gets back once at $t = 210$ fs, though). As mentioned before, this is the

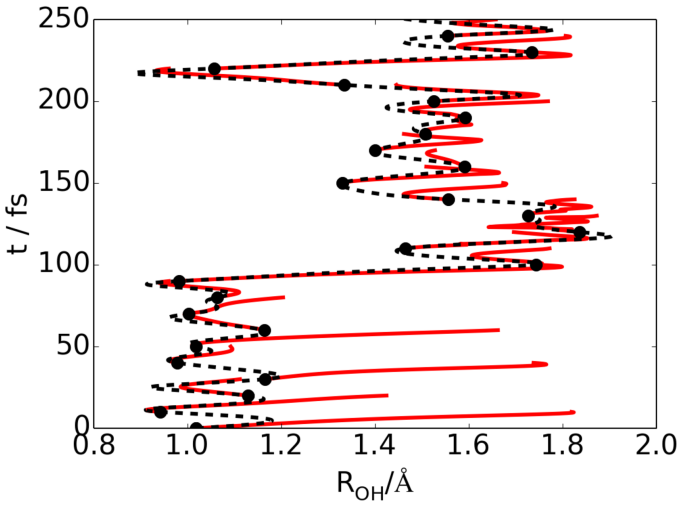

Figure 3.6: Internuclear distance between the transferred H and the nearest O along the path. The dashed line is the path of zero-point oscillation in S_0, which is completely adiabatic. The solid lines are paths that restarted after vertical excitation to S_3 with the same coordinates and momenta as that of S_0 at that time. Each excited-state path is generated every 10 fs and propagate for further 10 fs with SET.

proton transfer and thus an acid-base reaction.

On the other hand, the H atom is immediately transferred to the Ac side in the paths restarted in S_4 (solid lines in Fig. 3.4) if it is originally on the O atom side ($t < 100$ fs). In contrast, paths restarted from the Ac side ($t > 100$ fs) are not transferred back to the O atom side in (S_3, S_4). These results indicate that it is indeed more favorable for the transferred H atom to be on the Ac side if it is in (S_3, S_4) (they can mix by nonadiabatic transition) as we predicted in the one-dimensional analysis (excluding the path restarting at $t = 200$ fs). Therefore, the forward reaction (breaking the OH bond to form AcH) easily takes place in those excited states, while the backward one does not.

The detailed mechanism of the coupled proton-electron transfer in excited states

Here we pick up and explain one of the most illustrative cases, which is the path restarted at $t = 0$ fs in S_4. Most of the paths restarted at $t < 100$ fs are the same in quality. We begin with investigating the time propagation of the unpaired electron density along the SET path. The unpaired electron density $D(\mathbf{r})$ that uses natural orbitals as its basis functions is defined

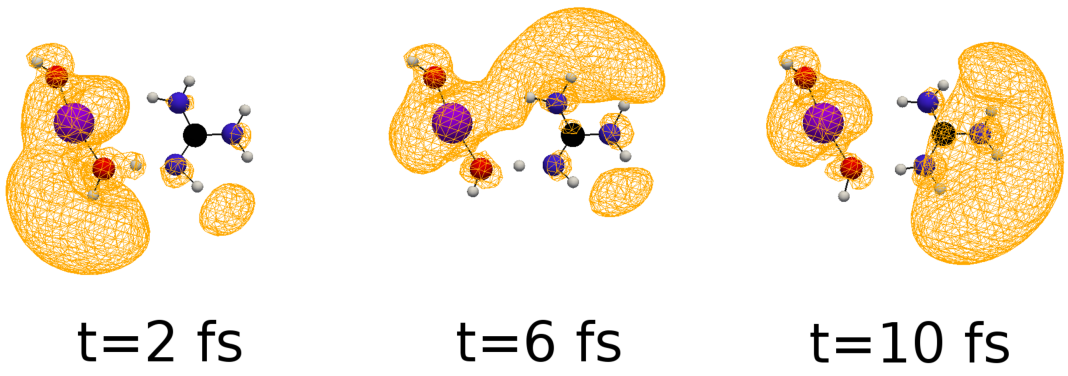

Figure 3.7: Snapshots of the unpaired electron density along the SET path obtained by full-dimensional on-the-fly dynamics for the case of X=OH. It clearly demonstrates that the coupled proton-electron transfer in excited states, where H^{n+} and ne^- takes mutually different pathways and reach spatially different places on the accepter Ac (Ac=guanidine in this case, see Fig. 3.2(a)). Color attribution is the same as Fig. 3.5.

as [137]

$$D(\mathbf{r}) = \sum_{l}^{NO} d_l(2-d_l)\psi_l^*(\mathbf{r})\psi_l(\mathbf{r}), \tag{3.8}$$

where ψ_l and d_l are respectively a natural orbital and its occupation number. Unpaired electron density serves to estimate the electron density of the singly occupied orbitals, because the coefficient $d_l(2-d_l)$ in Eq. (3.8) becomes maximum when $d_l = 1$ and minimum when $d_l = 0$ or 2. The unpaired electrons are responsible for radical character of an atom or a molecule. If the transferred H atom is dressed with unpaired electrons, it is regarded as a radical.

In the present dynamics, both the H atom and the unpaired electrons are transferred to Ac, but they obviously take different pathways and reach different places on Ac. Snapshots of the unpaired electron density along the path are shown in Fig. 3.7. The H atom is accepted by the nearest N atom of Ac, and the unpaired electrons become to occupy the Rydberg-like diffused orbitals on Ac. At $t = 2$ fs, the H atom is on the O atom side, and most of the unpaired electrons are on the same side. At $t = 6$ fs, both the H atom and the unpaired electrons take middle positions. However, the unpaired electrons are likely not on the H atom, that is, the H atom would not be a radical when it is transferred. At $t = 6$ fs, the H atom is finally transferred to Ac, and the unpaired electrons reach the Rydberg-like diffused orbitals. Therefore the H atom is still not a radical and charge recombination would not take place even at this point of time. A little more quantitative characterization of the transferred H atom is given later.

As shown in Fig. 3.8, the molecule indeed undergoes nonadiabatic transition by passing

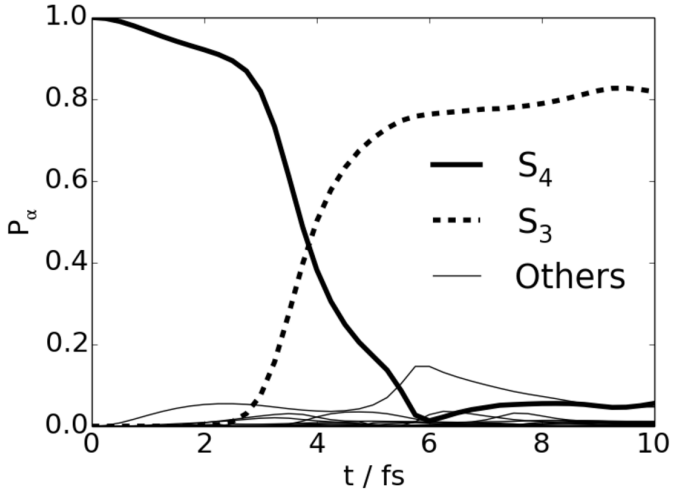

Figure 3.8: Adiabatic state population P_α along the path obtained by full-dimensional on-the-fly dynamics for the case of X=OH. The transition between S_3 and S_4 is prominent, which would occur near the avoided crossing between them shown in Fig. 3.4.

through near the nonadiabatic region shown in Fig. 3.4. The nonadiabatic transition between S_3 and S_4 is prominent. In this path, the other states contribute only a little to this dynamics by chance, but they can be involved much more because S_4 and higher states are densely quasi-degenerate (See Fig. 3.4). The amount of nonadiabatic transition between S_3 and S_4 is as much as 80%. This large transition implies that the avoided crossing is near a conical intersection. It is anticipated that the conical intersection is probably generated by electronic states with and without Rydberg-like diffused states.

The present mechanism is not equivalent to H radical transfer

Atomic population analysis can more quantitatively distinguish the present mechanism from radical transfer. Here we apply a hybrid method of Mulliken [138] and Hirshfeld [139] atomic population analysis. This hybrid method is explained in detail in Appendix C.

As shown in Fig. 3.9, the atomic charge Q_A of the transferred H atom along the path is kept as much as $+0.6$. This means that the transferred H atom is not a bare proton, but dressed with 0.4 electrons. As shown in Fig. 3.10, the atomic unpaired electron density D_A is kept close to zero, although the tonal number of the unpaired electrons is as much as 2.0. In this way, the H atom is not a radical, thereby we can confirm that the unpaired electrons indeed take different pathways to reach the Rydberg-like diffused states on Ac. Therefore, the transferred H atom should be expressed as $H^{0.6+}$, which is not a radical throughout the process. This result

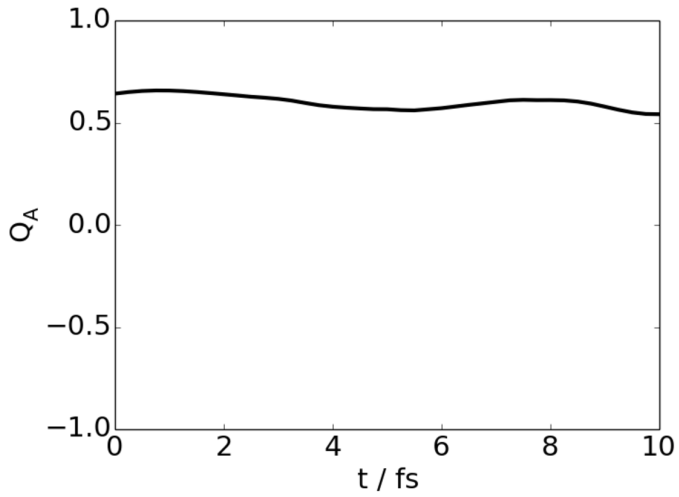

Figure 3.9: Atomic charge Q_A on the transferred H atom along the full-dimensional SET path, which is kept as much as $+0.6$. This means that the H atom should be expressed as $H^{0.6+}$ instead of bare proton H^+.

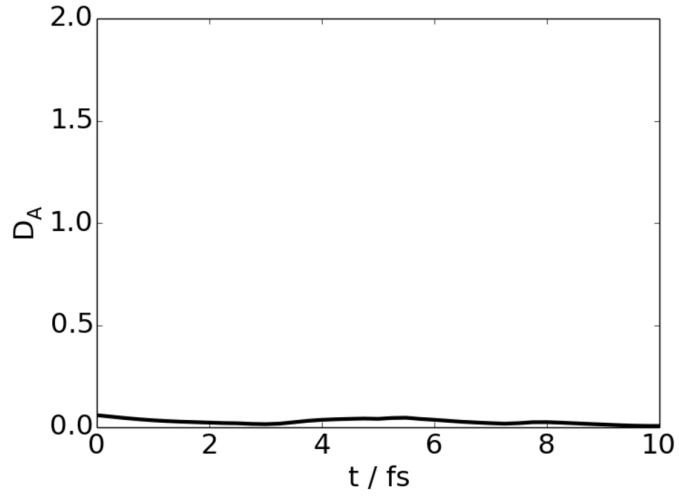

Figure 3.10: Atomic unpaired electron density D_A on the transferred H atom along the full-dimensional SET path, which is kept close to zero. This indicates that the transferred H atom is not a radical throughout, and the unpaired electrons indeed take different pathways to reach the Rydberg-like diffused states on Ac.

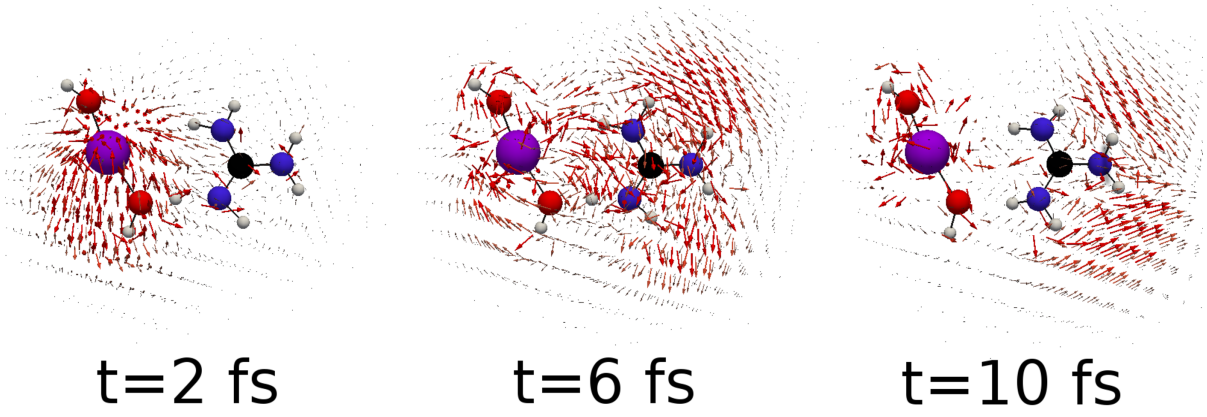

Figure 3.11: Snapshots of the electron flux along the path. Huge values that come from inner shell electrons are cut off to the preset maximum for a better visualization. The electron flux indicates circular motions of electrons, and it does not go parallel to the transferred H atom. Color attribution is the same as Fig. 3.5.

is parallel to the previous study of phenol-ammonia cluster system. [11]

Electron flux indicates circular motions of electrons

Here we calculate Schiff probability current (or flux, in short) [126] derived from the nonadiabatic electron wavepacket to reexamine the different pathways of H^{n+} and ne^{-}. This type of analysis has been performed by Takatsuka and coworkers, [11, 27, 140–142] and Manz and coworkers, [143–152] which have proved to be useful to track the nuclear and/or electronic pathways.

It would be worth mentioning here two typical examples where electron flux is useful to understand mechanisms of chemical reaction. First, let us mention the ground state dynamics of water-assisted proton relay in formamide [141]. This reaction results in intramolecular charge transfer as if a bare proton is transferred, but the mechanism is actually not so simple. The transferred H nucleus is always covered with as much as 0.7 electrons, and backward electron flux balances the net charge distribution. Second, we mention the excited state dynamics of coupled proton-electron transfer in phenol-ammonia cluster [11]. The electron flux serves to track the different pathways of electrons from the transferred H nucleus to the Rydberg-like diffused state on Ac. Here we apply the same analysis to find a similar result to this second example.

Snapshots of the electron flux shown in Fig. 3.11 indicate circular motions of electrons. In addition, the motions of electrons are not parallel to that of the transferred H atom. At $t = 2$ fs (before prominent nonadiabatic transition between S_3 and S_4), relatively large electron flux can

be seen only around $Mn(OH)OH_2$. The unpaired electrons (Fig. 3.7) do not move to Ac yet at this time as well. At $t = 6$ fs (right after the large nonadiabatic transition), the electrons look like moving anticlockwise around the transferred H atom. We cannot find significant electron flux parallel to the movement of the H atom. At $t = 10$ fs (the coupled proton-electron transfer is complete), the electron flux is rather pointing to the Rydberg-like diffused states than to the transferred H atom, thus the charge recombination is probably not starting yet.

As shown above, electron flux supports the mechanism involving different pathways. According to the electron flux, while H^{n+} moves linearly from the O atom to Ac, electrons make detours to the Rydberg-like diffused state on Ac to induce charge separation. It is consistent with the analysis with the unpaired electron density to clearly distinguish the present mechanism from H radical transfer.

3.4 Roles of Ca in the oxygen-evolving complex

3.4.1 Target system: X=(OH or O(Ca)H), Ac=*N*-methylformamidine

Let us investigate the roles of Ca in the context of photodynamics. A Ca atom is suggested to be an essential cofactor in the Mn cluster in PSII. [127] However, the actual role of Ca atom has not yet been definitely clarified. The roles proposed so far are mostly related to the structures and/or oxidation potentials [116, 153–156]. Here we propose the other types of roles of Ca in the context of photodynamics, namely, reducing the excitation energy and providing electrons involved in the coupled proton-electron transfer.

We demonstrate the static and dynamical analysis to the system of X-$MnOH_2 \cdots$ Ac, where X=(OH or O(Ca)H) and Ac=*N*-methylformamidine [157] (an analog of guanidine). The resulting optimized chemical structures are shown in Fig. 3.12. The structures are fortunately very similar to each other. In other words, the geometry is not affected so much by attachment of a Ca atom on the OH site. Thus they are suitable for investigating the role of calcium atom by comparison.

3.4.2 Properties in the projected one-dimensional coordinate

Those two molecules shown in Fig. 3.12 are similar to each other in a way that both projected one-dimensional potential curves and the electronic states remind us of the mecha-

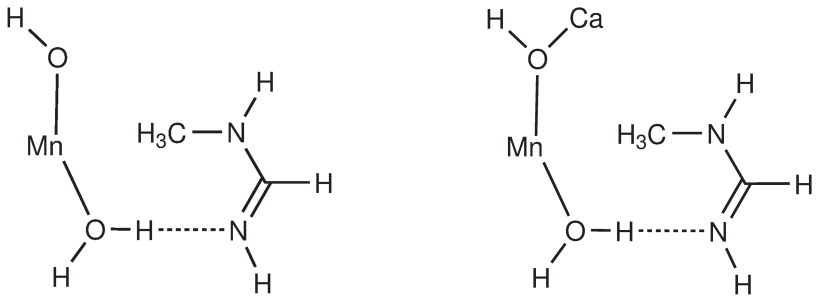

a) X=OH b) X=O(Ca)H

Figure 3.12: Chemical structures of X-$MnOH_2\cdots$Ac, where Ac=*N*-methylformamidine is common and X is different from each other. The structures are actually not planar, but rather twisted along the O-H$\cdots$Ac bonds.

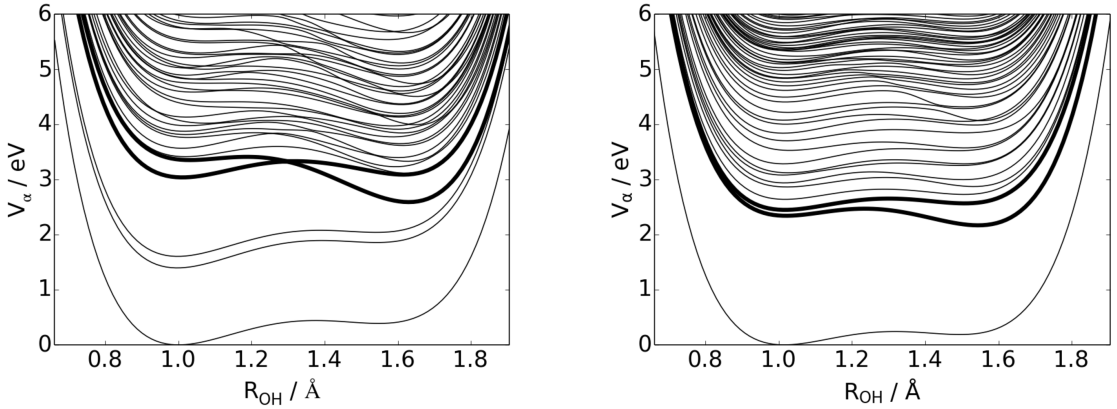

a) X=OH b) X=O(Ca)H

Figure 3.13: The one-dimensional potential curves of X-$MnOH_2\cdots$*N*-methylformamidine, where (a) X=OH and (b) X=O(Ca)H (See Fig. 3.12 for their structures). These potential curves are obtained in the same manner as before shown in Fig. 3.4.

nism discussed in Section 3.3. The potential curves obtained as the same manner as before (Fig. 3.4) are shown in Fig. 3.13. Both molecules have similar potential curves to that of $Mn(OH)OH_2\cdots$guanidine (Fig. 3.4). They commonly have minima on the O atom side in S_0, and on Ac side in the excited states expressed as thick lines in Fig. 3.13. The responsible electrons for the difference among the electronic states (the sum of electrons of natural orbitals whose occupation number is less than two) are also similar to the previous case without Ca atom (see Fig. 3.5). In S_0, the responsible electrons are kept on the donor side irrespective of the position of the transferred H atom, while those of the excited states commonly become to have contributions of the Rydberg-like diffused states. However, there are two remarkable differences between the two cases (with and without Ca).

First, excitation energy to access those excited states (expressed as thick lines in Fig. 3.13)

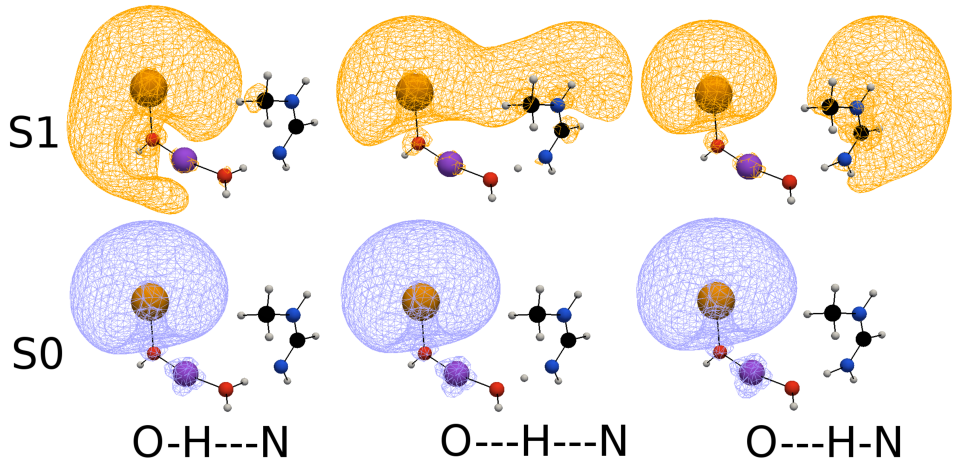

Figure 3.14: Spatial distribution of the sum of electrons of natural orbitals whose occupation number is less than two for X-$MnOH_2\cdots$*N*-methylformamidine, where X=O(Ca)H. The display style is the same as Fig. 3.5. The distribution is similar, except that most of the electrons are not on the Mn atom (see Fig. 3.15 for comparison). Color attribution is the same as Fig. 3.5, and Ca=orange.

is lowered from 3.2 eV to 2.4 eV when a Ca atom is attached. This shift indicates that the Ca atom serves to lower the excitation energy to enter the visible light range. Second, the origin of electrons responsible for the differences among the electronic states are altered when the Ca atom is attached (Fig. 3.14). In all the cases without Ca atom, the responsible electrons in S_0 are almost localized at the Mn atom connected with the water molecule. No such change is observed in the case of X=OH (Fig. 3.15).

3.4.3 Full-dimensional nonadiabatic electron dynamics

Now let us proceed to the full-dimensional nonadiabatic electron dynamics of Mn(O(Ca)H)$OH_2\cdots$(*N*-methylformamidine) to find the similarities and differences between the cases of X=OH and O(Ca)H. The case of X=OH is not shown here, because its dynamics is quite similar to that of the previous analysis done in the Sec. 3.3.

Initial conditions

Initial conditions are set in the same manner as the previous dynamics calculations. The total energy allocated to the nuclei is as much as that of zero-point oscillation. The molecule is vertically excited to S_1 at arbitrary time, which is defined to be $t = 0$ fs. We integrate the full-dimensional nonadiabatic electron wavepacket dynamics until $t = 10$ fs. Here we pick up one of the most illustrative cases of the mechanism.

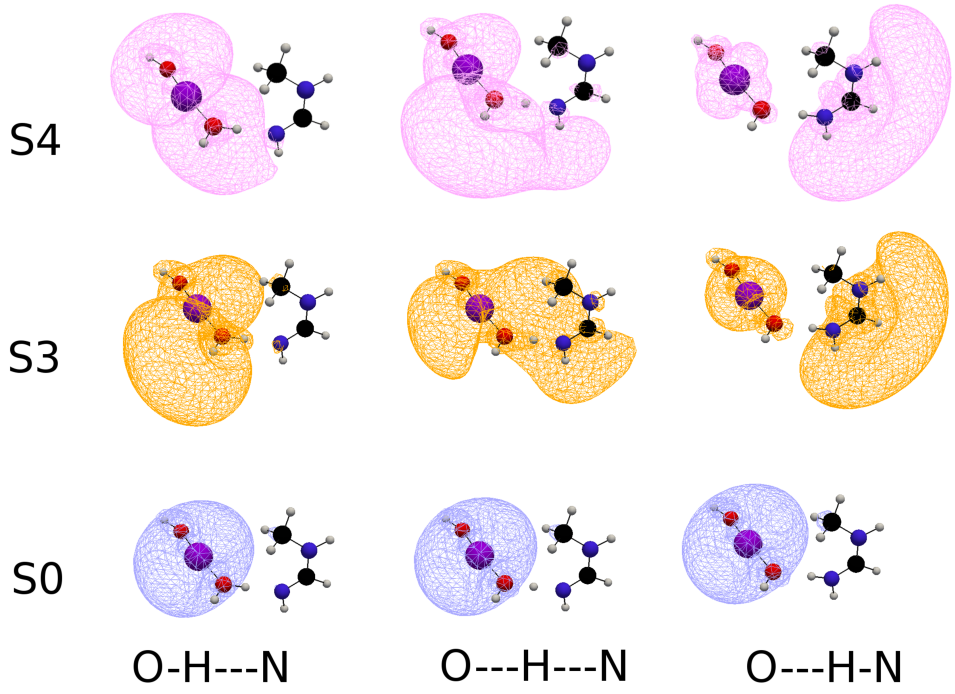

Figure 3.15: Spatial distribution of the sum electrons in natural orbitals whose occupation number is less than two for X-$MnOH_2 \cdots$*N*-methylformamidine, where X=OH. The display style is the same as Fig. 3.5. The distribution is very similar to that of the case of Ac=guanidine (Fig. 3.5). Color attribution is the same as Fig. 3.14.

Resemblances and differences in the mechanism

On the whole, the mechanism found in the Ca adduct (Fig. 3.12(b)) is the same as that without the Ca (Fig. 3.12(a)). The atomic change Q_A on the transferred H atom (Fig. 3.16) and the atomic unpaired electron density D_A (Fig. 3.17) are qualitatively the same as those of the previous analysis in Section 3.3. Thus the transferred H atom is actually $H^{0.6+}$ and not a radical as well. The part of the unpaired electrons reach the Rydberg-like diffused states on Ac through different pathways from the transferred H atom as shown in Fig. 3.18.

However, there are some differences between the cases with and without Ca. As we have seen in the projected one-dimensional analysis, the unpaired electrons likely populate on the Ca atom instead of the Mn atom. At $t = 6$ fs, roughly half of the unpaired electrons seem to be on the Ca atom (see Fig. 3.18), while they are on the Mn atoms in the previous calculation (see Fig. 3.7). The electron flux around the Mn atoms is relatively small compared to that around the Ca atom (see Fig. 3.19).

To sum up, the photodynamical mechanism found in the case of X=O(Ca)H is the same as X=OH on the whole, but we found two significant differences. First, the photon energy to access the relevant excited states are lowered from 3.2 eV (390 nm) to 2.4 eV (520 nm) by the

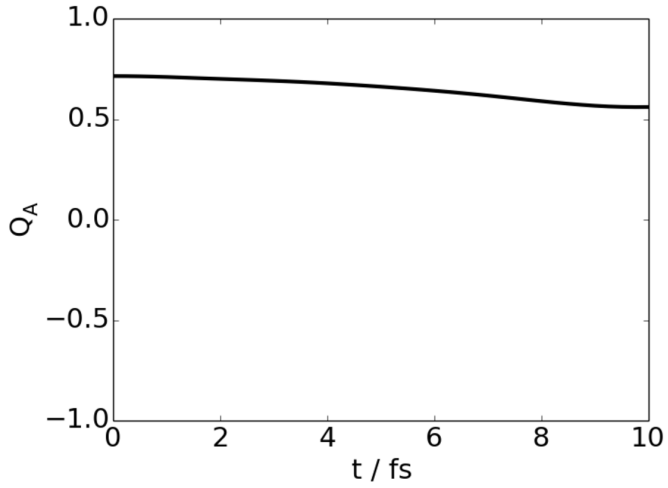

Figure 3.16: Atomic charge Q_A on the transferred H atom along the full-dimensional SET path, which is kept as much as $+0.6$. This indicates that the transferred H atom is actually $H^{0.6+}$ as well as the previous analysis without the Ca atom (see Fig. 3.9).

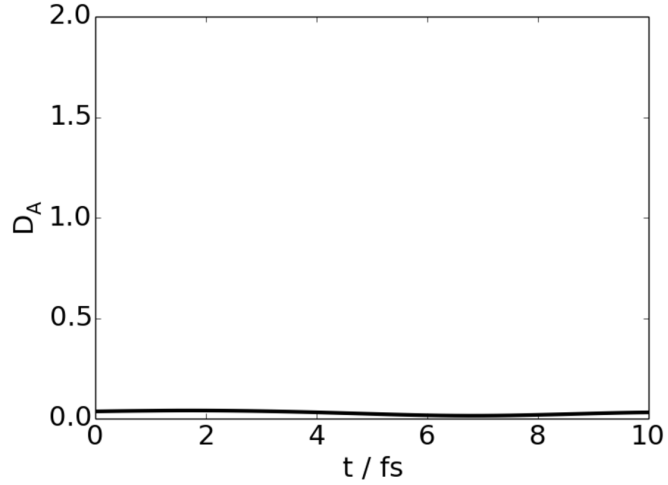

Figure 3.17: Atomic unpaired electron density D_A on the transferred H atom along the SET path obtained by full-dimensional on-the-fly dynamics for the case of X=O(Ca)H. And the unpaired electrons indeed take different pathways to reach the Rydberg-like diffused states on Ac as well as the previous analysis without the Ca atom (see Fig. 3.10).

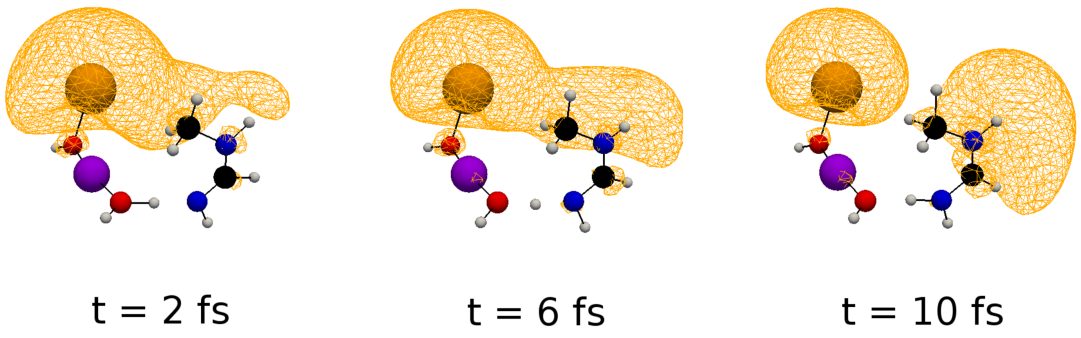

Figure 3.18: Snapshots of the unpaired electron density along the SET path obtained by full-dimensional on-the-fly dynamics for the case of X=O(Ca)H. Color attribution is the same as Fig. 3.14.

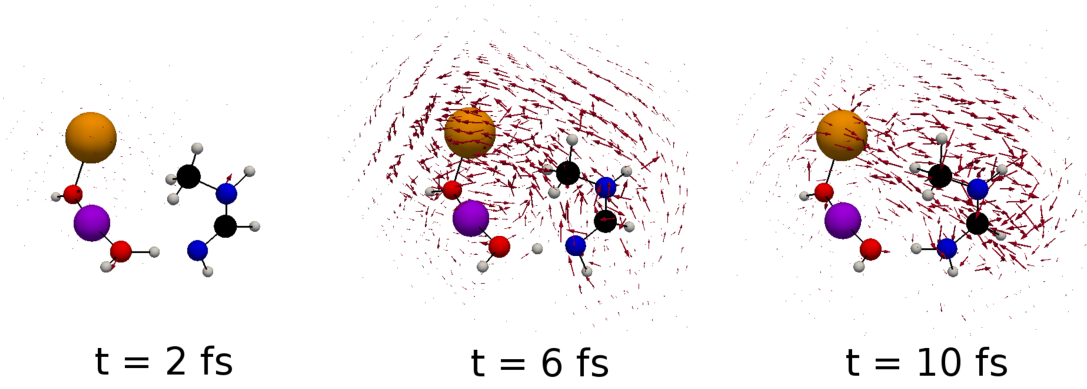

Figure 3.19: Snapshots of the electron flux along the SET path obtained by full-dimensional on-the-fly dynamics for the case of X=O(Ca)H. Color attribution is the same as Fig. 3.14.

attachment of the Ca atom. Second, the unpaired electrons are likely produced by the Ca atom instead of the Mn atom.

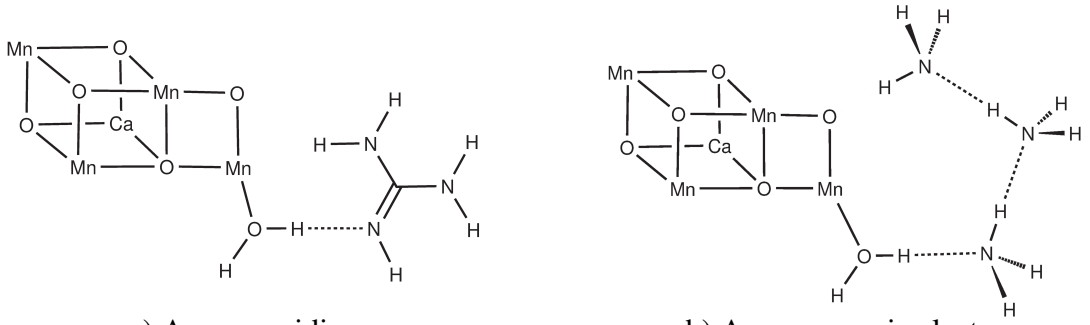

Figure 3.20: Chemical structure of $Mn_4CaO_5OH_2\cdots$Ac. a) The case where Ac=guanidine. The $MnOH_2\cdots$guanidine part is almost the same as that of $Mn(OH)OH_2\cdots$guanidine shown in Fig. 3.2(a). b) The case where Ac=ammonia cluster, Note that these structure is rather schematic, but the actual structure is a little more distorted.

3.5 The Mn cluster of the oxygen-evolving complex embedded in PSII

3.5.1 Target system: X=Mn_3CaO_5 and Ac=(guanidine or ammonia cluster)

Now we demonstrate the case where the proton-electron donor X-$MnOH_2$ is the Mn cluster of the oxygen-evolving complex embedded in PSII shown in Fig. 3.1. The acceptor Ac is chosen to be Ac=(guanidine or ammonia cluster). The resulting molecules are schematically shown in Fig. 3.20. The actual structures are a little more distorted. This donor can also be expressed as X-$MnOH_2$ with X=Mn_3CaO_5. The O-$MnOH_2$ part is common among molecules studied so far. Since it is difficult in terms of machine power at present to perform full-dimensional nonadiabatic electron wavepacket dynamics for this system, here we only investigate the one-dimensional properties to demonstrate that they are significantly resemble those of X=OH and X=O(Ca)H in many ways.

3.5.2 Properties in the projected one-dimensional coordinate

Here we show that the case of X=Mn_3CaO_5 resembles qualitatively the case of X=OH and X=O(Ca)H that we have discussed so far. The projected one-dimensional potential curves obtained in the same manner as Fig. 3.4 and 3.13 is shown in Fig. 3.21. The set of S_0 and (S_2, S_3) seems similar to that of S_0 and (S_3, S_4) in the case X=OH in the following ways: i) The minimum in S_0 is on the O atom side, while those in (S_2, S_3) are on the guanidine side. ii) (S_2,

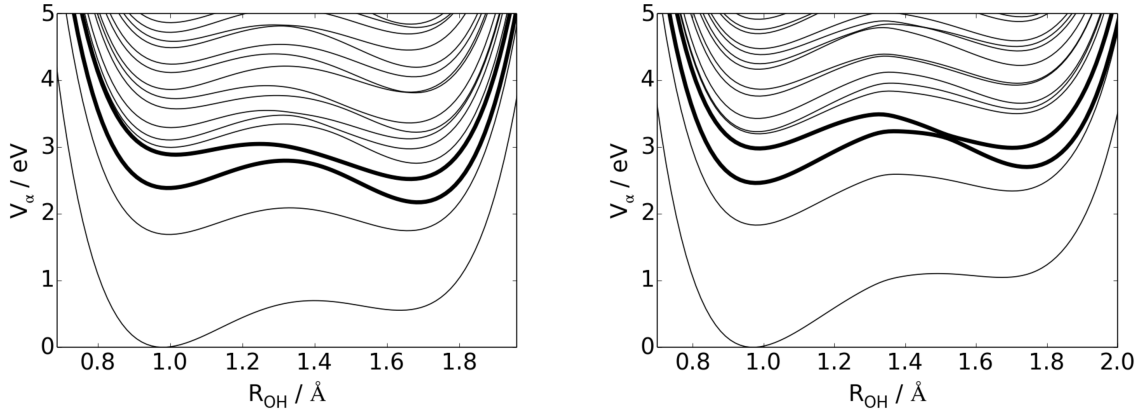

Figure 3.21: Potential energy curves of in the relevant one-dimensional coordinate, which is obtained in the same manner as Fig. 3.4.

S_3) has nonadiabatic region. iii) (S_2, S_3) has electrons in the Rydberg-like diffused states, but S_0 does not.

The electronic states of the present cases are also similar to those of X=OH and X=O(Ca)H. The sum of electron density of natural orbitals whose occupation number is less than two is shown in Fig. 3.22 and 3.23, which are respectively corresponding to Ac=guanidine and Ac=ammonia cluster. In both cases, S_3 becomes to have contributions from the Rydberg-like diffused states on Ac when the H atom is transferred.

The photon energy to access the relevant excited states (expressed as thick lines in Fig. 3.21) in the present system is more similar to that of X=O(Ca)H rather than X=OH (see Fig. 3.13). That possibly owes to the Ca atom, as we have seen in the Sec. 3.4. The responsible electrons (the sum of electrons of natural orbitals whose occupation number is less than two) in S_0 are shared by the Ca and Mn atoms, thus we can indeed find the contribution of the Ca atom.

The X-$MnOH_2$ where X=OH or X=O(Ca)H can be regarded as a good representative of the present system of the Mn cluster of the oxygen-evolving complex in a way that it has similar potential curves and similar electronic states, although it contains only a single Mn atom. Therefore, we can anticipate that the same photodynamical mechanism (coupled proton-electron transfer resulting in charge separation on Ac) can be found even in these relatively realistic cases.

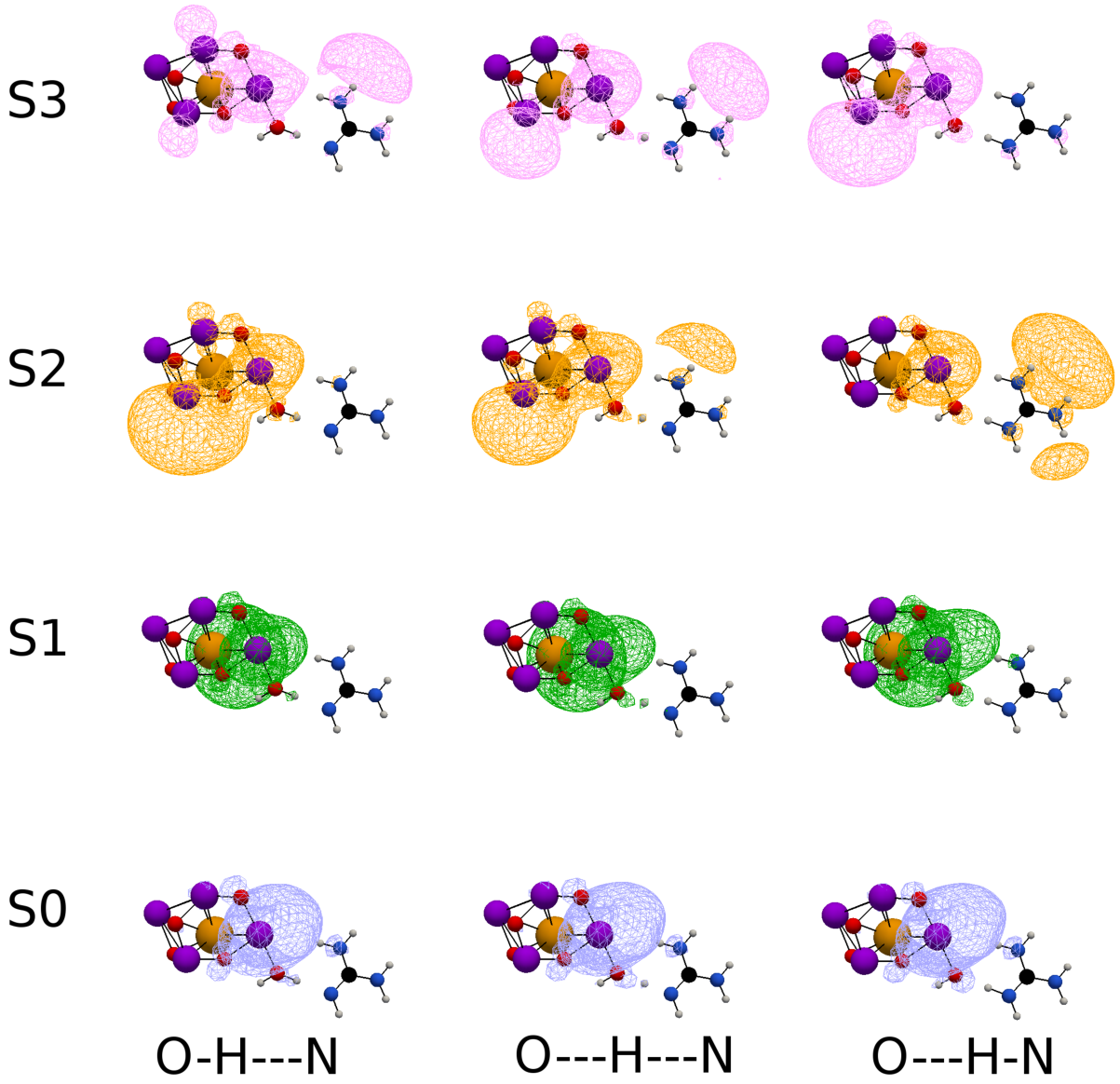

Figure 3.22: Spatial distribution of electrons in natural orbitals whose occupation number is less than two for $Mn_4CaO_5OH_2 \cdots$ guanidine. The row denotes the position of transferred H atom, while the column does the adiabatic states. We can find the Rydberg-like diffused states in S_3, which is the same situation in Fig. 3.5.

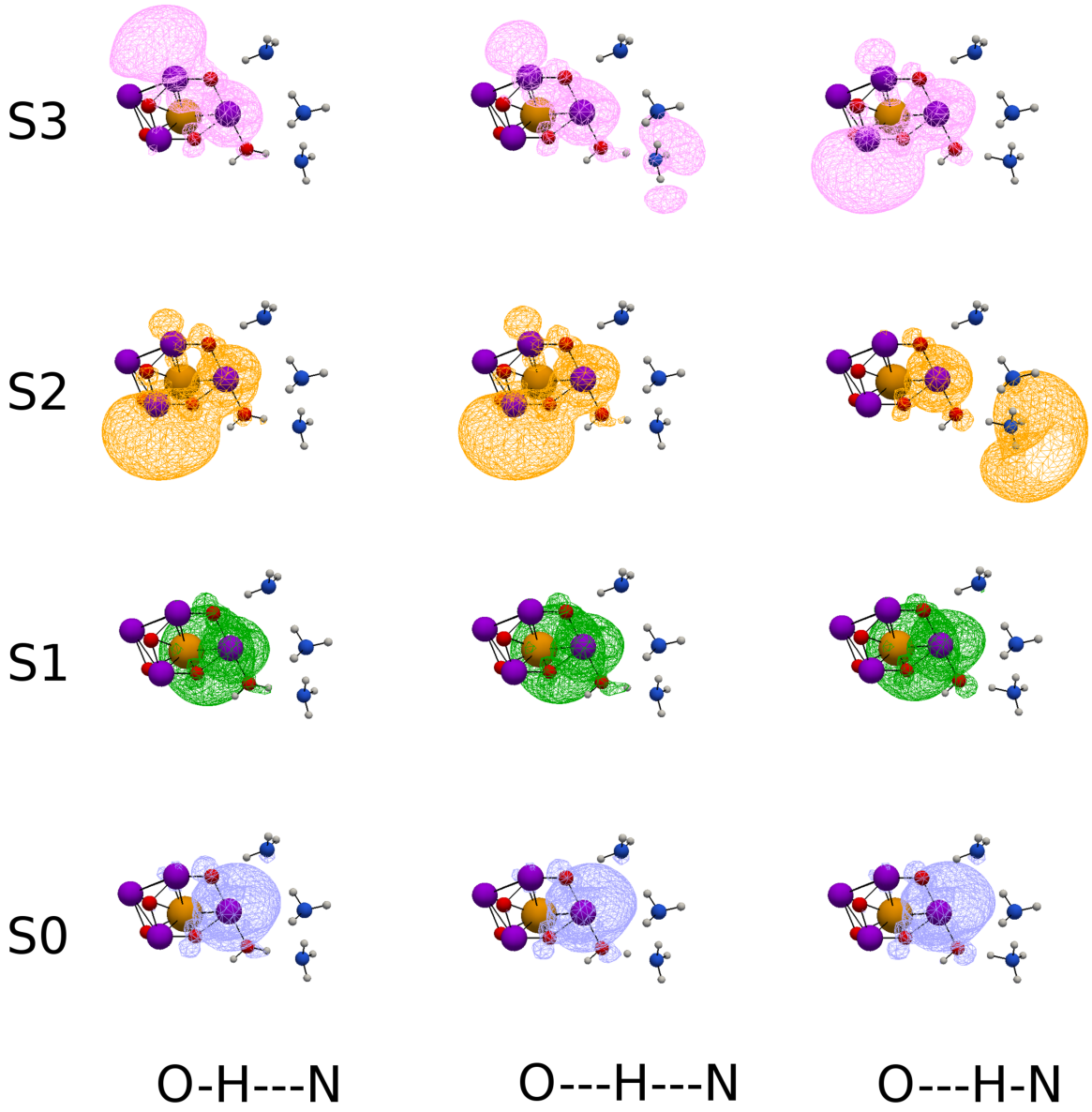

Figure 3.23: Spatial distribution of electrons in natural orbitals whose occupation number is less than two for $Mn_4CaO_5OH_2 \cdots$ ammonia cluster. The row denotes the position of transferred H atom, while the column does the adiabatic states. We can find the Rydberg-like diffused states in S_3, which is the same situation in Fig. 3.5.

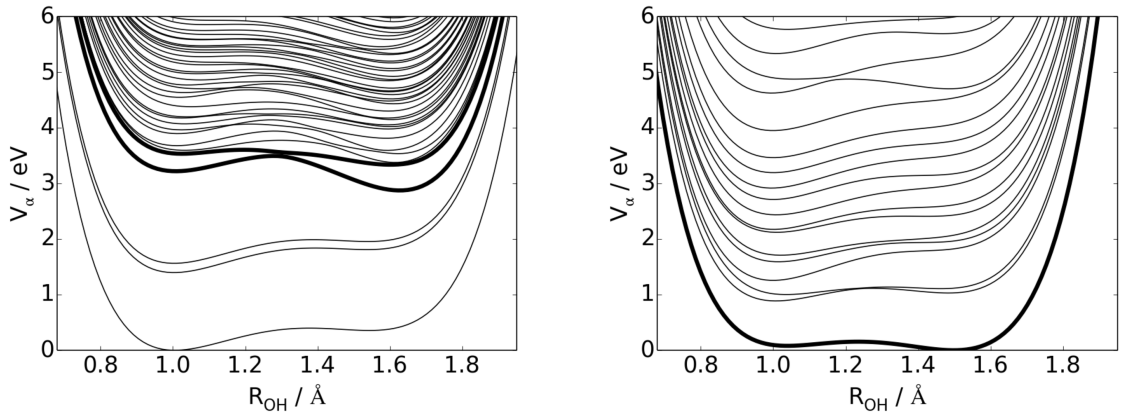

Figure 3.24: Adiabatic potential curves as functions of position of the transferred H atom for $Mn(OH)OH_2\cdots$(ammonia cluster) (a) and $[Mn(OH)OH_2\cdots$(ammonia cluster)$]^-$ (b). In the case(a), S_3 and S_4 are drawn as thick lines, which include the Rydberg-like diffused states, while in the case (b), such a state is S_0 (see Fig. 3.26).

3.6 Electron attachment as an alternative mechanism

3.6.1 Target system: X=OH, Ac=ammonia cluster (neutral and anion)

Now we mention another scenario of water decomposition, which is related to the present coupled proton-electron transfer. We have assumed so far that the energy to drive the reaction of coupled proton-electron transfer is produced by direct photoexcitation, but this is not the only possibility. Here we consider the case where an electron is somehow attached to the $Mn(OH)OH_2\cdots$(ammonia cluster) (Fig. 3.2(c)). The resulting molecule $[Mn(OH)OH_2\cdots$(ammonia cluster)$]^-$ is optimized again, but the geometry is not affected so much by this operation.

Incidentally, $Mn(OH)OH_2\cdots$(ammonia cluster) does not have electron affinity in terms of the energy of MOs, thus the following analysis should be kept in mind as reference. It can become more meaningful if this molecule is embedded in relevant environment such as a protein or solvent.

3.6.2 Properties in the projected one-dimensional properties

The projected one-dimensional potential curves obtained in the same manner as Fig. 3.4 for neutral and anionic molecules are shown in Fig. 3.24. In anion (Fig. 3.24(b)), the position of the minimum in S_0 is shifted from the O atom side to the Ac side. This shift reminds us of that of the excited states (S_3, S_4) of the neutral (Fig. 3.24(a)). The spatial distribution of responsible electrons are shown in Fig. 3.26 for the neutral and Fig. 3.25 for the anion. S_3 or S_4 of the

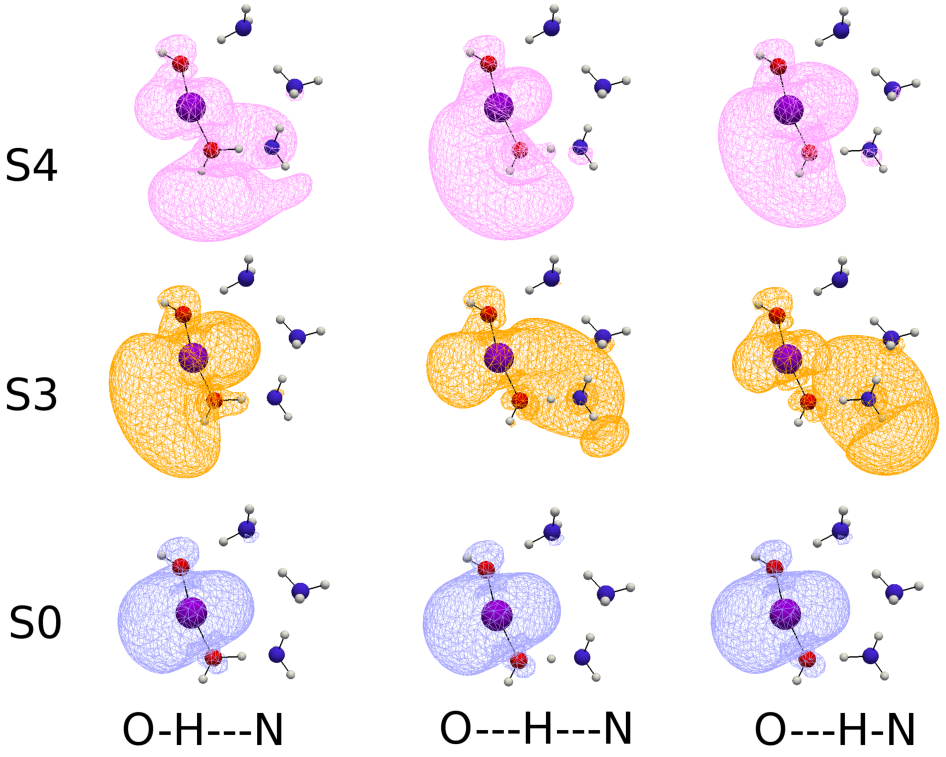

Figure 3.25: Spatial distribution of the sum electrons of natural orbitals whose occupation number is less than two for $Mn(OH)OH_2 \cdots$ ammonia cluster. The row denotes the position of transferred H atom, while the column does the adiabatic states S_0, S_3 and S_4. Those of S_1 and S_2 are similar to that of S_0. We can find the Rydberg-like diffused states only in the excited states. They are quite similar to those of Ac=guanidine shown in Fig. 3.5. Color attribution is the same as Fig. 3.14.

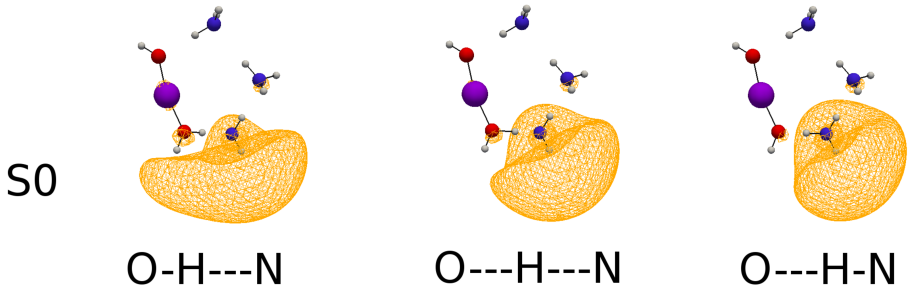

Figure 3.26: Spatial distribution of the sum electrons of natural orbitals whose occupation number is less than two for $[Mn(OH)OH_2 \cdots$ ammonia cluster$]^-$. The colors are attributed to atoms as follows: H=white, C=black, N=blue, O=red and Mn=purple. The attached electron likely occupies the Rydberg-like diffused states like those of (S_3, S_4) of the neutral shown in Fig. 3.25. Color attribution is the same as Fig. 3.14.

neutral is more similar to S_0 of the anion than S_0 of the neutral.

3.7 Concluding remarks

We have investigated photodynamics of X-$MnOH_2\cdots$Ac, which is stimulated by the Mn cluster embedded in PSII, by means of the theory of nonadiabatic electron wavepacket dynamics. Here X and Ac are respectively an arbitrary subsystem and a proton-electron acceptor. Various X and Ac are examined to find a common mechanism of coupled proton-electron transfer in excited states. The reaction on the proton-electron donor (X-$MnOH_2$) is expressed as

$$\text{X-MnOH}_2 + h\nu \rightarrow \text{X-MnOH} + \text{H}^{n+} + n\text{e}^- \qquad (n \approx 0.6). \tag{3.9}$$

The mechanism can be summarized as follows:

1. Excited electronic states are generated by UV-visible light.
2. H^{n+} is transferred to Ac through nonadiabatic region.
3. ne^- are transferred to the Rydberg-like states of Ac.

Significantly, this mechanism results in charge separation on Ac, because the H^{n+} and ne^- reach different places on Ac through mutually different pathways (see Fig. 3.7 and 3.11, for example). Charge recombination does not take place immediately after the coupled proton-electron transfer, thus further charge separation can follow this mechanism as a trigger.

We have investigated various X and Ac, and found that they have similar projected one-dimensional potential curves relevant to the present mechanism. We especially focus on the case where X=OH and Ac=guanidine (Fig. 3.2(a)) to perform the full-dimensional nonadiabatic electron wavepacket dynamics. In the derived mechanism from the dynamics, H^{n+} and ne^- ($n \approx 0.6$) take different pathways and reach spatially different places on Ac to induce charge separation. Note that this is exactly the excited state mechanism. The ground state dynamics with the similar initial nuclear coordinates and momenta results in a common acid-base reaction, and thus it does not induce charge separation on Ac.

We have clarified the effect of a Ca atom in the X-$MnOH_2$ system by comparing molecules with and without the Ca atom, and found that the Ca atom serves to reduce the photon energy to access the relevant electronic states, which was almost the same as the system of $Mn_4CaO_5OH_2$.

This implies that the role of Ca atom is to reduce the excitation energy, and produce the electrons involved in the reaction.

In connection with the oxygen-evolving complex in PSII, we also investigated the case where X=Mn_3CaO_5 and Ac=(guanidine or ammonia cluster), namely, $Mn_4CaO_5OH_2 \cdots Ac$ (Fig. 3.20). Even in this larger system, we could obtain similar projected one-dimensional potential curves relevant to the present mechanism. This implies that the partial system ($Mn(OH)OH_2 \cdots Ac$, for example) can well represent the dynamics of the Mn cluster in the oxygen-evolving complex.

This work is stimulated by the system of the oxygen-evolving complex, but we do not mean to "simulate" its dynamics at present. As we mentioned in Sec. 3.6, there are a number of possible channels in the oxygen-evolving complex. However, our work provided the first example of using photon energy for charge separation by means of electron dynamics in the relevant system to the oxygen-evolving complex, which is a novel aspect of this field of science.

Chapter 4

General conclusion

We have investigated nonadiabatic electron dynamics in chemical reactions to propose mechanisms involving nonadiabatic interaction. We were especially concerned with low energy dynamics, where the total energy allocated to the nuclear motion toward the potential barrier was as much as its height. In this case, nonadiabatic interaction is rather crucial than unignorable.

In Chap. 2, we have applied the developed method to rather conceptual systems, and proposed two mechanisms involving nonadiabatic interaction, namely, tunneling-like effect and friction-like effect. In the tunneling-like effect, some part of branching paths surmounts the potential barrier by using the force from excited states, although the path originally does not have enough energy to surmount the barrier in the ground state. On the other hand, in the friction-like effect, the part of branching paths is reflected by the force from excited states, while the path is originally able to surmount the barrier. These mechanisms are expected to bring about pulse trains. This phenomenon is also confirmed in full-quantum calculation. We performed multi-dimensional implementation to find essentially the same mechanism.

The method was derived in the present work from the path-branching representation (PBR), which was the general expression of mixed quantum-classical theory. As we have explained, exact calculation of PBR needs infinite number of branching paths, which is technically impossible. Thus we needed to somehow extract representative paths from the cascade of branching paths. We adopted wavepacket averaging of the force matrix to realize such an extraction. This operation gave rise the equivalent force to the semiclassical Ehrenfest theory (SET) to the first order. As for path-branching, the important idea was the use of "side paths". The side paths were defined to be virtually generated at the entrance of nonadiabatic region, and driven by mutually different eigenforces. This method has an advantage over the previous methods for

path-branching in low energy cases, where the total energy allocated to nuclear degrees of freedom is comparable to the potential barrier height. The number of side-paths is the same as electronic states involved. When the side paths become far apart from each other more than a given threshold, path-branching is invoked. The number of path-branching is unlimited.

In Chap. 3, we have demonstrated the photodynamical mechanism resulting in charge separation. The system was chosen to be X-$MnOH_2\cdots$Ac, where X and Ac were arbitrary subsystem and proton-electron accepter, respectively. We were stimulated to examine such a system by the Mn cluster of oxygen evolving complex embedded in the photosystem II (PSII). The reaction on the proton-electron donor is expressed as

$$\text{X-MnOH}_2 + h\nu \rightarrow \text{X-MnOH} + \text{H}^{n+} + n\text{e}^- \qquad (n \approx 0.6). \tag{4.1}$$

In the proposed mechanism, H^{n+} and ne^- reach spatially different places on Ac through mutually different pathways, which results in charge separation on Ac. We have emphasized that this mechanism should be distinguished from H radical transfer, because the unpaired electrons were not on the transferred H atom. Since charge recombination does not take place immediately after the coupled proton-electron transfer, this mechanism can be a trigger of the further charge separation. This is the first example of mechanisms using photon energy for charge separation by means of electron dynamics in the relevant system to the oxygen-evolving complex.

On the whole, the mechanism was not affected by the attachment of Ca but we found two possible roles of the Ca atom, namely, reducing the excitation energy and providing electrons involved in the coupled proton-electron transfer. Because most of the proposed role of the Ca atom is concerned with the structure and/or oxidation potential, our rule should be recognized as a novel one.

We also examined one-dimensional properties of $Mn_4CaO_5OH_2\cdots$Ac, in which the Mn cluster of the oxygen-evolving complex is used as a proton-electron donor. The one-dimensional properties well resemble those of molecules investigated so far, thus the similar mechanism can probably be found even in this rather large system. This implies that the smaller subsystem including only a single Mn atom can represent the more realistic larger cases.

The present work has proven that the nonadiabatic electron dynamics is indeed inevitable for the appropriate description of some chemical reactions. By means of the nonadiabatic electron dynamics, we could produce further insight into chemical reactions. It was beyond the scope of standard methods based on the Born–Oppenheimer approximation. [1]

List of publications

[1] Jörn Manz and Kentaro Yamamoto, Mol. Phys. **110** , 517 (2012).
A selection rule for the directions of electronic fluxes during unimolecular pericyclic reactions in the electronic ground state

[2] Kentaro Yamamoto and Kazuo Takatsuka, J. Chem. Phys. **140**, 124111 (2014).
Electronic quantum effects mapped onto non-Born–Oppenheimer nuclear paths: Nonclassical surmounting over potential barriers and trapping above the transition states due to nonadiabatic path-branching

Appendix A

Parallel computation of numerical derivatives

A.1 Technical difficulty in the evaluation of derivatives

Here we discuss rather technical details to materialize full-dimensional, on-the-fly dynamics for the system of X-$MnOH_2$ in realistic calculation time. The rate-determining step of such a calculation is evaluation of derivatives such as $\partial H_{IJ}^{(el)}/\partial R_k$ and X_{IJ}^k. The program of analytic derivatives with CISD/RHF level of calculation is implemented in the quantum chemistry package GAMESS. [128, 129] However, it takes unrealistically long time for relatively large system for technical reasons. There are mainly two reasons why the program of analytic derivatives takes so long time.

First, the program for analytic derivatives does not run with "frozen virtual orbitals". This means that the number of configuration state functions (CSFs) increases exponentially as that of AOs (MOs) does. We have to choose a very small basis set such as STO-6G because of this constraint. In the present work, we calculate CISD by the graphical unitary group approach (GUGA) [130–136]. In this method, we divide all the MOs (in ascending order of energy) into four parts, namely, frozen core, active core, active virtual and frozen virtual orbitals. CISD is calculated only among the active core and the active virtual orbitals to reduce the exponential increase of the number of CSFs. However, we have to set the number of the frozen virtual orbitals to zero in analytic derivative calculation, because it is not implemented. In other words, we must set all the virtual orbitals to active ones. Therefore, if the number of AO (MO) increases, the number of CSFs increases exponentially.

Second, the program for analytic derivatives does not support parallel computation, although that for single point energy does. Here the parallel computation means using many computers to obtain a single target value. Therefore, no matter how many computational resources are available, we cannot use them to improve the speed of calculation.

It is never easy to solve those problems by only modifying the codes of GAMESS, because the relevant program is extremely complicated. On the other hand, single point energy calculation does not have such problems, that is, it supports both the frozen virtual orbitals and the parallel computation. Thus there is even a case where the evaluation speed of numerical derivatives exceeds that of analytic derivatives if a target system is significantly large. Accordingly, we come to a conclusion that parallel evaluation of single point values to calculate numerical derivatives is probably the fastest way in terms of real calculation time. In the following sections, we discuss implementation of a framework of parallel computation of numerical derivatives using the Python programming language as a wrapper of GAMESS.

A.2 Matrix elements to be calculated

We actually calculate numerical derivatives for $\frac{\partial H_{IJ}^{(el)}}{\partial R_k}$ and X_{IJ}^k . In this section, we clarify what is necessary to be evaluated in each single-point calculation. Now we consider the case where adiabatic wavefunctions $\{\Phi_\alpha\}$ are used as a basis set. They are expanded as

$$\Phi_\alpha \;=\; \sum_I C_{\alpha I}\Phi_I. \tag{A.1}$$

$\{\Phi_I\}$ can be any orthonormal basis set in general, but here we regard it as CSFs. The derivatives of the adiabatic representation of the electronic Hamiltonian matrix $\frac{\partial H_{\alpha\beta}^{(el)}}{\partial R_k}$ can be reduced as

$$\frac{\partial H_{\alpha\beta}^{(el)}(\mathbf{R})}{\partial R_k} \;\approx\; \frac{\delta_{\alpha\beta}}{2\Delta R}\left[\epsilon_\alpha(\mathbf{R}+\mathbf{e}_k\Delta R)-\epsilon_\alpha(\mathbf{R}-\mathbf{e}_k\Delta R)\right], \tag{A.2}$$

where ΔR is small variation along each nuclear coordinate and $\{\epsilon_\alpha\}$ is a set of adiabatic state energy obtained through diagonalization of $H_{IJ}^{(el)}$. Thus the desired derivatives can be calculated

if $\{\epsilon_\alpha\}$ at $6N$ points[*1] are obtained. The nonadiabatic coupling matrix $X^k_{\alpha\beta}$ can be expanded as

$$\begin{aligned} X^k_{\alpha\beta} &= \left\langle \alpha \middle| \frac{\partial}{\partial R_k} \middle| \beta \right\rangle \\ &= \sum_I C^*_{\alpha I} \frac{\partial C_{\beta I}}{\partial R_k} + \sum_{IJ} C^*_{\alpha I} C_{\beta J} X^k_{IJ}. \end{aligned} \tag{A.3}$$

We need to calculate numerical derivatives of both $\frac{\partial C_{\beta I}}{\partial R_k}$ and X^k_{IJ} to obtain $X^k_{\alpha\beta}$. The former can be reduced as

$$\sum_I C^*_{\alpha I} \frac{\partial C_{\beta I}}{\partial R_k} \approx \frac{1}{2\Delta R} \sum_I C^*_{\alpha I} \left[C_{\beta I}(\mathbf{R} + \mathbf{e}_k \Delta R) - C_{\beta I}(\mathbf{R} - \mathbf{e}_k \Delta R) \right], \tag{A.4}$$

which can be calculated if $C_{\alpha I}$ of $6N$ points are available. The latter can be reduced as

$$\sum_{IJ} C_{\alpha I} C_{\beta J} X^k_{IJ} \approx \frac{1}{2\Delta R} \sum_{IJ} C_{\alpha I} C_{\beta J} \left(\langle \Phi_I(\mathbf{R}) | \Phi_J(\mathbf{R} + \mathbf{e}_k \Delta R) \rangle - \langle \Phi_I(\mathbf{R}) | \Phi_J(\mathbf{R} - \mathbf{e}_k \Delta R) \rangle \right), \tag{A.5}$$

which can be evaluated if the overlap matrix of the basis sets at the target point and $6N$ shifted points are available. Here we have assumed that $\{\Phi_I\}$ is CSFs, thus $\langle \Phi_I(\mathbf{R}) | \Phi_J(\mathbf{R} + \mathbf{e}_k \Delta R) \rangle$ can be expanded as

$$\langle \Phi_I(\mathbf{R}) | \Phi_J(\mathbf{R} + \mathbf{e}_k \Delta R) \rangle \approx \frac{1}{N_e} \sum_{IJ}^{CSF} \sum_{ij}^{MO} \sum_{\mu\nu}^{AO} C^*_{\alpha I} C_{\beta J} a^{IJ}_{ij} c_{\mu i}(\mathbf{R}) c_{\nu j}(\mathbf{R} + \mathbf{e}_k \Delta R) S_{\mu\nu}. \tag{A.6}$$

Here we used the approximation $\langle \chi_\mu(\mathbf{R}) | \chi_\nu(\mathbf{R} + \mathbf{e}_k \Delta R) \rangle \approx S_{\mu\nu}$. Therefore, $X^k_{\alpha\beta}$ can be obtained if $\{C_{\alpha I}\}$ and $\{c_{\mu i}\}$ at $6N$ points under the approximation we made above. In short, we just need to calculate a set of adiabatic state energy, $\{\epsilon_\alpha\}$, CI coefficients $\{C_{\alpha I}\}$, and MO coefficients $\{c_{\mu i}\}$ for $6N$ points in parallel for fast evaluation of $\frac{\partial H^{(el)}_{\alpha\beta}}{\partial R_k}$ and $X^k_{\alpha\beta}$.

A.3 A framework for parallel computation of numerical derivatives

The basic idea of the framework is quite simple, that is, distributing $6N$ input data to many computers to perform single-point calculations, and then collecting all the results to gener-

[*1] N is the number of atoms. The "$6N$" is the number of points to calculate single-point values (forward and backward shift $\times$ degrees of freedom).

ate numerical derivatives. The setup to materialize this idea is schematically shown in Fig. A.1. It consists of four types of "processes", namely, client (C), server (S), translator (T) and worker(W). Here the "process" with double quotation marks is defined to denote the process in terms of computation.

The framework is a kind of the client-server model of computation. The client sends a request to perform $6N$ single-point calculations to the server, and the client eventually receives the results as its response. The server hides the translators and workers from the client to hide their complexity as well. We have at most $6N$ pairs of translator and worker taking charge of single-point calculations. It depends on the amount of computational resources. If we can only generate less than $6N$ pairs, some pairs perform the calculation more than once. If excess resources are available, they are assigned to each worker. The translator and worker always appear in pair, and the worker can communicate only with its counterpart.

The framework is implemented with two programming languages, that is, Python and FORTRAN 77. While the client, the server, and the translator are implemented with Python, the worker is implemented with FORTRAN 77, which is nothing but modified GAMESS [128, 129] in the present study. We choose Python because of the library named `multiprocessing` in the Python's standard library. We can implement a multiprocess program with so much less codes than using MPI by means of this library. We need the translator because GAMESS [128, 129] cannot directly receive a Python object.

The actual data flow can be summarized as follows: (1) The client sends both the input data (*e.g.* coordinates) and a request to perform single-point calculations to the server. (2) The server distributes the received input data to the translators. (3) Each translator sends the given part of input data to the worker after converting the data to readable format for it. (4) Each worker performs single-point quantum chemical calculation corresponding to the given part of input data. (5) Each result is sent back to the server through the connected translator. In this step, the translator converts the result appropriately as it does for the part of input data. (6) After all the single point calculations complete, the results accumulated in the server are sent back to the client. (7) The client calculates numerical derivatives by use of the results of single point calculation.

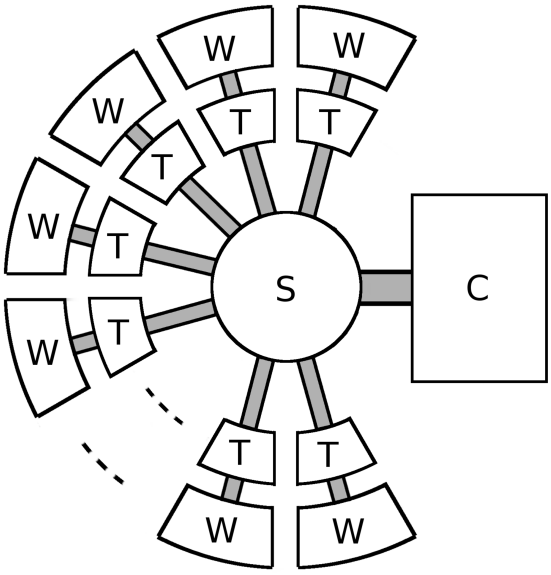

Figure A.1: Schematic representation of the correlation of “processes” in the proposed framework of parallel computation of numerical derivatives. Each piece denotes an independent “process”. Connections among those pieces represent the existence of interprocess communication. This framework is a kind of the client-server model of computation. It consists of four kinds of “processes”, namely, client (C), server (S), translator (T) and worker(W).

Appendix B

Smooth connection among on-the-fly basis sets

Technically speaking, it is not guaranteed that adiabatic wavefunctions calculated on-the-fly varies continuously in time, because they have some arbitrariness. The electron wavepacket in the present study is expanded in the form

$$\Psi(\mathbf{R}, \mathbf{r}, t) \;=\; \sum_{\alpha} C_{\alpha}(t)\Phi_{\alpha}(\mathbf{r}; \mathbf{R}(t)), \tag{B.1}$$

and $\{\Phi_{\alpha}\}$ is adiabatic wavefunctions calculated on-the-fly. If the adiabatic wavefunctions calculated on-the-fly are continuous in time, the time-shifted overlap matrix $\bar{S}_{\alpha\beta}(t) \equiv \langle \Phi_{\alpha}(t) | \Phi_{\beta}(t - \Delta t) \rangle$, where Δt is a small time step, is almost equal to the identity matrix as

$$\bar{S}_{\alpha\beta} \;\approx\; \delta_{\alpha\beta}. \tag{B.2}$$

However, in practice, the resulting $\bar{\mathrm{S}}$ matrix is quite often obviously different from the identity matrix. For example, if the phase (or $+/-$) of the wavefunction is reversed, $\bar{\mathrm{S}}$ should be something like

$$\begin{pmatrix} \ddots & & & \\ & -0.99 & 0.01 & \\ & 0.01 & 0.99 & \\ & & & \ddots \end{pmatrix}, \tag{B.3}$$

or if the order of them is swapped, $\bar{\mathrm{S}}$ should be something like

$$\begin{pmatrix} \ddots & & & \\ & 0.01 & 0.99 & \\ & 0.99 & 0.01 & \\ & & & \ddots \end{pmatrix}. \tag{B.4}$$

This discontinuity leads to (numerical) divergence in integrating the equations of motion. Thus we need to make them smoothly connected in time.

Here we propose a simple method to realize such a smooth connection. In this method, we transform the original on-the-fly basis set by attributing each component to that of the previous one. Suppose the relevant transformation matrix is expressed as T, that is,

$$\Phi'_\alpha(t) = \sum_\beta \Phi_\beta(t) T_{\beta\alpha}, \tag{B.5}$$

where $\{\Phi_\alpha(t)\}$ is the raw on-the-fly basis set and $\{\Phi'_\alpha(t)\}$ is the transformed but equivalent basis set, which is smoothly connected to $\{\Phi'_\alpha(t-\Delta t)\}$. Here we define the "prime" symbol to denote that the basis set is transformed to be smooth.

In order to construct T, first we expand $\{\Phi'_\alpha(t-\Delta t)\}$ with $\{\Phi_\alpha(t)\}$ as

$$\begin{aligned} |\Phi'_\alpha(t-\Delta t)\rangle &= \sum_\beta |\Phi_\beta(t)\rangle\langle\Phi_\beta(t)|\Phi'_\alpha(t-\Delta t)\rangle \\ &= \sum_\beta |\Phi_\beta(t)\rangle \bar{S}_{\beta\alpha}. \end{aligned} \tag{B.6}$$

Here the basis set is assumed to be complete. Now $\bar{\mathrm{S}}$ can be recognized as a matrix to transform $\{\Phi_\alpha(t)\}$ to $\{\Phi'_\alpha(t-\Delta t)\}$, therefore a good candidate for T.

Now we take $\bar{\mathrm{S}}$ as an initial guess for T. We assume that there is no degenerate component. In this case, the matrix element of T should be one of 0, ± 1, so that the transformed basis set is equivalent to the original. T is calculated as follows (for each α),

$$T_{\beta\alpha} = \begin{cases} \mathrm{sign}(\bar{S}_{\beta\alpha}), & \text{if } |\bar{S}_{\beta\alpha}| = \max(|\bar{S}_{\beta\alpha}|) \\ 0, & \text{otherwise} \end{cases}, \tag{B.7}$$

where the "max" function scans index β of each α. Finally, the resulting T is used to calculate

Eq. (B.5).

Appendix C

Hybrid atomic population analysis

Here we explain the hybrid population analysis used in Chapter 3 to assign either electron density or unpaired electron density $\rho(\mathbf{r})$ to a specific atom. The method is a hybrid of the Mulliken [138] and Hirshfeld [139] methods. The former is oriented to atomic orbital (AO) density matrix, while the latter is to spatial distribution. Mulliken's method is in general not suitable for the system where diffuse orbitals are included in the atomic basis set. [139, 158] On the other hand, Hirshfeld can better assign it, but is numerically unstable, because inner shell orbitals are too steep for easy numerical integral. [139] Therefore, we take an approach such as dividing the density into two parts, where one of them includes most of the contribution of diffuse orbitals (Hirshfeld's method in charge), and the other one does that of inner shell orbitals (Mulliken's method in charge). Each partial density is integrated to obtain partial atomic population. Finally we merge those two parts to evaluate atomic population. Hereafter we explain the method in detail.

Now we consider to assign either electron density, unpaired electron density, or any other density $\rho(\mathbf{r})$. The density $\rho(\mathbf{r})$ is expanded as

$$\rho(\mathbf{r}) \;=\; \sum_{\mu\nu}^{\mathrm{AO}} P_{\mu\nu}\chi_\mu(\mathbf{r})\chi_\nu(\mathbf{r}), \tag{C.1}$$

where $\{\chi_\mu(\mathbf{r})\}$ is an atomic basis set and $P_{\mu\nu}$ is its density matrix, to a specific atom A. First we derive a general form. Let us introduce a weighting operator $\hat{w}_A$ to partition the density, which is integrated to give P_A as

$$P_A \;=\; \int \hat{w}_A\, \rho(\mathbf{r}) d\mathbf{r}. \tag{C.2}$$

We can derive both Mulliken and Hirshfeld atomic population by setting $\hat{w}_A$ appropriately. The Mulliken atomic population [138] is derived by setting the weighting operator $\hat{w}_A^{(M)}$ as

$$\hat{w}_A^{(M)} P_{\mu\nu} \;\equiv\; \begin{cases} P_{\mu\nu}, & \text{if } \chi_\mu \text{ belongs to atom } A \\ 0, & \text{otherwise} \end{cases}. \tag{C.3}$$

Inserting Eq. (C.3) to Eq. (C.2) indeed gives us the definition of Mulliken atomic population $P_A^{(M)}$ as

$$P_A^{(M)} \;=\; \sum_{\mu\in A,\nu}^{\text{AO}} P_{\mu\nu} S_{\mu\nu}, \tag{C.4}$$

where $S_{\mu\nu}$ is an AO overlap matrix. Meanwhile, the Hirshfeld atomic population [139] is derived by setting the weighting operator $\hat{w}_A^{(H)}$ as

$$\hat{w}_A^{(H)} \;\equiv\; \frac{\rho_A^{\text{at}}(\mathbf{r})}{\sum_B \rho_B^{\text{at}}(\mathbf{r})}, \tag{C.5}$$

where $\rho_A^{\text{at}}(\mathbf{r})$ is spherically averaged ground-state electron density of an suitably positioned (isolated) atom.

Next we proceed to divide the density into two parts so that one of them includes most diffuse orbitals and the other does most inner shell orbitals to obtain the atomic population. We can materialize it by dividing CI natural orbitals (NOs) into higher and lower parts in occupation number. Lower parts should include most diffuse orbitals. The resulting parts of density, say respectively $\rho^i(\mathbf{r})$ and $\rho^d(\mathbf{r})$, are integrated after operating $\hat{w}_A$ to give atomic population P_A

$$P_A \;=\; \int \left(\hat{w}_A^{(M)} \rho^i(\mathbf{r}) + \hat{w}_A^{(H)} \rho^d(\mathbf{r}) \right) d\mathbf{r} \tag{C.6}$$

This method provides numerically stable and not physically meaningful atomic population.

References

[1] Born, M.; Oppenheimer, R. *Annalen der Physik* **1927**, *389*(20), 457–484.

[2] Domcke, W.; Yarkony, D.; Köppel, H. *Conical Intersections: Electronic Structure, Dynamics & Spectroscopy*, Vol. 15; World Scientific, 2004.

[3] Yonehara, T.; Hanasaki, K.; Takatsuka, K. *Chem. Rev.* **2011**, *112*(1), 499–542.

[4] Hentschel, M.; Kienberger, R.; Spielmann, C.; Reider, G. A.; Milosevic, N.; Brabec, T.; Corkum, P.; Heinzmann, U.; Drescher, M.; Krausz, F. *Nature* **2001**, *414*(6863), 509–513.

[5] Kling, M. F.; Vrakking, M. J. *Annu. Rev. Phys. Chem.* **2008**, *59*, 463–492.

[6] Krausz, F.; Ivanov, M. *Rev. Mod. Phys.* **2009**, *81*(1), 163.

[7] Wodtke, A. M.; Tully, J. C.; Auerbach, D. J. *Int. Rev. Phys. Chem.* **2004**, *23*(4), 513–539.

[8] Yonehara, T.; Takatsuka, K. *J. Chem. Phys.* **2012**, *137*(22), 22A520.

[9] Woodward, R.; Hoffmann, R. *Angew. Chem. Int. Ed. Engl* **1969**, *8*, 781.

[10] Hammes-Schiffer, S.; Stuchebrukhov, A. A. *Chem. Rev.* **2010**, *110*(12), 6939–6960.

[11] Nagashima, K.; Takatsuka, K. *J. Phys. Chem. A* **2012**, *116*(46), 11167–11179.

[12] Berry, M. V. *Proc. R. Soc. A* **1984**, *392*(1802), 45–57.

[13] Tully, J. C.; Preston, R. K. *J. Chem. Phys.* **1971**, *55*(2), 562–572.

[14] Tully, J. C. *J. Chem. Phys.* **1990**, *93*(2), 1061–1071.

[15] Balakrishnan, N.; Kalyanaraman, C.; Sathyamurthy, N. *Phys. Rep.* **1997**, *280*(2), 79–144.

[16] Tully, J. *Faraday Discuss.* **1998**, *110*, 407–419.

[17] Zhu, C.; Nakamura, H. *J. Chem. Phys.* **1994**, *101*(12), 10630–10647.

[18] Hack, M. D.; Truhlar, D. G. *J. Phys. Chem. A* **2000**, *104*(34), 7917–7926.

[19] Jasper, A. W.; Zhu, C.; Nangia, S.; Truhlar, D. G. *Faraday Discuss.* **2004**, *127*, 1–22.

[20] Takatsuka, K. *J. Phys. Chem. A* **2007**, *111*(41), 10196–10204.

[21] Yonehara, T.; Takatsuka, K. *J. Chem. Phys.* **2008**, *128*(15), 154104.

[22] Yonehara, T.; Takatsuka, K. *J. Chem. Phys.* **2008**, *129*(13), 134109.

[23] Yonehara, T.; Takahashi, S.; Takatsuka, K. *J. Chem. Phys.* **2009**, *130*(21), 214113.

[24] Yonehara, T.; Takatsuka, K. *Chem. Phys.* **2009**, *366*(1), 115–128.

[25] Yonehara, T.; Takatsuka, K. *J. Chem. Phys.* **2010**, *132*(24), 244102.

[26] Takatsuka, K.; Yonehara, T. *Phys. Chem. Chem. Phys.* **2011**, *13*(11), 4987–5016.

[27] Takatsuka, K.; Yonehara, T. *Adv. Chem. Phys.* **2010**, *144*, 93–156.

[28] Yonehara, T.; Takatsuka, K. *J. Phys. Chem. A* **2013**, *117*(36), 8599–8608.

[29] Yamamoto, K.; Takatsuka, K. *J. Chem. Phys.* **2014**, *140*(12), 124111.

[30] Jasper, A.; Kendrick, B. K.; Mead, C. A.; Truhlar, D. G. In *Modern Trends in Chemical Reaction Dynamics Part I*; Yang, X., Liu, K., Eds.; World Scientific, 2004; chapter 8.

[31] Feynman, R. P.; Hibbs, A. R. *Quantum mechanics and path integrals;* McGraw-Hill, 1965.

[32] Schulman, L. S. *Techniques and applications of path integration;* Courier Dover Publications, 2012.

[33] Miller, W. H. *Adv. Chem. Phys* **1974**, *25*(1), 69–177.

[34] Child, M. S. *Semiclassical mechanics with molecular applications*, Vol. 25; Oxford University Press on Demand, 1991.

[35] Pechukas, P. In *Dynamics of Molecular Collisions, Part B*; Miller, W. H., Ed.; Plenum Press: New York, 1976.

[36] Pollak, E.; Child, M. S. *J. Chem. Phys.* **1980**, *73*(9), 4373–4380.

[37] Yanao, T.; Takatsuka, K. *J. Chem. Phys.* **2004**, *120*(19), 8924–8936.

[38] Neumark, D. M. *Acc. Chem. Res.* **1993**, *26*(2), 33–40.

[39] Takatsuka, K. *Phys. Rev. A* **1997**, *55*(1), 347.

[40] Benderskii, V.; Makarov, D.; Wight, C. *Adv.Chem. Phys.* **1994**, *88*, 55.

[41] Garrett, B. C.; Truhlar, D. G. *J. Chem. Phys.* **1983**, *79*(10), 4931–4938.

[42] Gonzalez-Lafont, A.; Truong, T. N.; Truhlar, D. G. *J. Chem. Phys.* **1991**, *95*(12), 8875–8894.

[43] Takatsuka, K.; Ushiyama, H.; Inoue-Ushiyama, A. *Phys. Rep.* **1999**, *322*(5), 347–417.

[44] Meana-Pañeda, R.; Truhlar, D. G.; Fernández-Ramos, A. *J. Chem. Phys.* **2011**, *134*(9), 094302.

[45] Goumans, T. P. M.; Kastner, J. *J. Phys. Chem. A* **2011**, *115*(39), 10767–10774.

[46] Trahan, C. J.; Wyatt, R. E. *Quantum dynamics with trajectories: introduction to quantum hydrodynamics;* Springer, 2006.

[47] Bittner, E. R. *J. Chem. Phys.* **2000**, *112*(22), 9703–9710.

[48] Baer, M. *Beyond Born-Oppenheimer: electronic nonadiabatic coupling terms and conical intersections;* John Wiley & Sons, 2006.

[49] Bersuker, I. B. *The Jahn-Teller Effect;* Cambridge University Press, 2006.

[50] Nakamura, H. *Nonadiabatic Transition;* World Scientific, 2002.

[51] Arasaki, Y.; Takatsuka, K.; Wang, K.; McKoy, V. *Phys. Rev. Lett.* **2003**, *90*(24), 248303.

[52] Arasaki, Y.; Takatsuka, K.; Wang, K.; McKoy, V. *J. Chem. Phys.* **2003**, *119*(15), 7913–7923.

[53] Arasaki, Y.; Takatsuka, K.; Wang, K.; McKoy, V. *J. Chem. Phys.* **2010**, *132*(12), 124307.

[54] Arasaki, Y.; Wang, K.; McKoy, V.; Takatsuka, K. *Phys. Chem. Chem. Phys.* **2011**, *13*(19), 8681–8689.

[55] Horio, T.; Fuji, T.; Suzuki, Y.-I.; Suzuki, T. *J. Am. Chem. Soc.* **2009**, *131*(30), 10392–10393.

[56] Suzuki, Y.-I.; Fuji, T.; Horio, T.; Suzuki, T. *J. Chem. Phys.* **2010**, *132*(17), 174302.

[57] Kraus, P.; Arasaki, Y.; Bertrand, J.; Patchkovskii, S.; Corkum, P.; Villeneuve, D.; Takatsuka, K.; Wörner, H. *Phys. Rev. A* **2012**, *85*(4), 043409.

[58] Scheit, S.; Arasaki, Y.; Takatsuka, K. *J. Phys. Chem. A* **2011**, *116*(11), 2644–2653.

[59] Meyer, H.-D.; Miller, W. H. *J. Chem. Phys.* **1979**, *70*(7), 3214–3223.

[60] Micha, D. A. *J. Chem. Phys.* **1983**, *78*(12), 7138–7145.

[61] García-Vela, A.; Gerber, R.; Imre, D. *J. Chem. Phys.* **1992**, *97*(10), 7242–7250.

[62] Miller, W. H. *Faraday Discuss.* **1998**, *110*, 1–21.

[63] Hack, M. D.; Jasper, A. W.; Volobuev, Y. L.; Schwenke, D. W.; Truhlar, D. G. *J. Phys. Chem. A* **2000**, *104*(2), 217–232.

[64] Amano, M.; Takatsuka, K. *J. Chem. Phys.* **2005**, *122*(8), 084113.

[65] Miller, W. H. *J. Phys. Chem. A* **2009**, *113*(8), 1405–1415.

[66] Li, B.; Miller, W. H. *J. Chem. Phys.* **2012**, *137*(15), 154107.

[67] Tao, G. *J. Phys. Chem. A* **2013**, *117*(28), 5821–5825.

[68] Stock, G.; Thoss, M. *Phys. Rev. Lett.* **1997**, *78*(4), 578.

[69] Shalashilin, D. V. *J. Chem. Phys.* **2009**, *130*(24), 244101.

[70] Shalashilin, D. V. *J. Chem. Phys.* **2010**, *132*(24), 244111.

[71] Shalashilin, D. V. *Faraday Discuss.* **2011**, *153*, 105–116.

[72] Burghardt, I.; Meyer, H.-D.; Cederbaum, L. *J. Chem. Phys.* **1999**, *111*(7), 2927–2939.

[73] Beck, M. H.; Jäckle, A.; Worth, G.; Meyer, H.-D. *Phys. Rep.* **2000**, *324*(1), 1–105.

[74] Martínez, T. J. *Acc. Chem. Res.* **2006**, *39*(2), 119–126.

[75] Levine, B. G.; Martínez, T. J. *Annu. Rev. Phys. Chem.* **2007**, *58*, 613–634.

[76] Yang, S.; Coe, J. D.; Kaduk, B.; Martínez, T. J. *J. Chem. Phys.* **2009**, *130*(13), 134113.

[77] Born, M.; Huang, K. *Dynamical Theory of Crystal Lattices;* Oxford University Press: Oxford, 1954.

[78] Rose, T. S.; Rosker, M. J.; Zewail, A. H. *J. Chem. Phys.* **1988**, *88*(10), 6672–6673.

[79] Grote, R. F.; Hynes, J. T. *J. Chem. Phys.* **1980**, *73*(6), 2715–2732.

[80] Grote, R. F.; Hynes, J. T. *J. Chem. Phys.* **1981**, *74*(8), 4465–4475.

[81] Hänggi, P.; Talkner, P.; Borkovec, M. *Reviews of Modern Physics* **1990**, *62*(2), 251.

[82] Umena, Y.; Kawakami, K.; Shen, J.-R.; Kamiya, N. *Nature* **2011**, *473*(7345), 55–60.

[83] Kok, B.; Forbush, B.; McGloin, M. *Photochem. Photobiol.* **1970**, *11*(6), 457–475.

[84] Bouges-Bocquet, B. *Biochim. Biophys. Acta, Bioenerg.* **1973**, *292*(3), 772–785.

[85] Joliot, P. *Photosynth. Res.* **2003**, *76*(1-3), 65–72.

[86] Yano, J.; Yachandra, V. *Chem. Rev.* **2014**, *114*(8), 4175–4205.

[87] Brimblecombe, R.; Koo, A.; Dismukes, G. C.; Swiegers, G. F.; Spiccia, L. *J. Am. Chem. Soc.* **2010**, *132*(9), 2892–2894.

[88] Swierk, J. R.; Mallouk, T. E. *Chem. Soc. Rev.* **2013**, *42*(6), 2357–2387.

[89] Sartorel, A.; Bonchio, M.; Campagna, S.; Scandola, F. *Chem. Soc. Rev.* **2013**, *42*(6), 2262–2280.

[90] Kärkäs, M. D.; Verho, O.; Johnston, E. V.; Åkermark, B. *Chem. Rev.* **2014**.

[91] Zouni, A.; Witt, H.-T.; Kern, J.; Fromme, P.; Krauss, N.; Saenger, W.; Orth, P. *Nature* **2001**, *409*(6821), 739–743.

[92] Kamiya, N.; Shen, J.-R. *Proc. Natl. Acad. Sci.* **2003**, *100*(1), 98–103.

[93] Ferreira, K. N.; Iverson, T. M.; Maghlaoui, K.; Barber, J.; Iwata, S. *Science* **2004**, *303*(5665), 1831–1838.

[94] Loll, B.; Kern, J.; Saenger, W.; Zouni, A.; Biesiadka, J. *Nature* **2005**, *438*(7070), 1040–1044.

[95] Kawakami, K.; Umena, Y.; Kamiya, N.; Shen, J.-R. *J. Photochem. Photobiol. B* **2011**, *104*(1), 9–18.

[96] Glöckner, C.; Kern, J.; Broser, M.; Zouni, A.; Yachandra, V.; Yano, J. *J. Biol. Chem.* **2013**, *288*(31), 22607–22620.

[97] Yano, J.; Yachandra, V. K. *Inorg. Chem.* **2008**, *47*(6), 1711–1726.

[98] Dau, H.; Zaharieva, I.; Haumann, M. *Curr. Opin. Chem. Biol.* **2012**, *16*(1), 3–10.

[99] Penner-Hahn, J. E. In *Metal Sites in Proteins and Models Redox Centres;* Springer, 1998; pages 1–36.

[100] Yano, J.; Kern, J.; Sauer, K.; Latimer, M. J.; Pushkar, Y.; Biesiadka, J.; Loll, B.; Saenger, W.; Messinger, J.; Zouni, A.; others. *Science* **2006**, *314*(5800), 821–825.

[101] Cox, N.; Pantazis, D. A.; Neese, F.; Lubitz, W. *Acc. Chem. Res.* **2013**, *46*(7), 1588–1596.

[102] Noguchi, T.; Sugiura, M. *Biochemistry* **2002**, *41*(7), 2322–2330.

[103] Noguchi, T. *Philos. Trans. R. Soc., B* **2008**, *363*(1494), 1189–1195.

[104] Siegbahn, P. E. *Chem. - Eur. J.* **2008**, *14*(27), 8290–8302.

[105] Siegbahn, P. E. *Acc. Chem. Res.* **2009**, *42*(12), 1871–1880.

[106] Siegbahn, P. E. *ChemPhysChem* **2011**, *12*(17), 3274–3280.

[107] Siegbahn, P. E. *Biochim. Biophys. Acta* **2013**, *1827*(8), 1003–1019.

[108] Ames, W.; Pantazis, D. A.; Krewald, V.; Cox, N.; Messinger, J.; Lubitz, W.; Neese, F. *J. Am. Chem. Soc.* **2011**, *133*(49), 19743–19757.

[109] Luber, S.; Rivalta, I.; Umena, Y.; Kawakami, K.; Shen, J.-R.; Kamiya, N.; Brudvig, G. W.; Batista, V. S. *Biochemistry* **2011**, *50*(29), 6308–6311.

[110] Ichino, T.; Yamaguchi, K.; Yoshioka, Y. *Chem. Lett.* **2012**, *41*(1), 18–20.

[111] Kusunoki, M. *J. Photochem. Photobiol., B* **2011**, *104*(12), 100 – 110.

[112] Kanda, K.; Yamanaka, S.; Saito, T.; Umena, Y.; Kawakami, K.; Shen, J.-R.; Kamiya, N.; Okumura, M.; Nakamura, H.; Yamaguchi, K. *Chem. Phys. Lett.* **2011**, *506*(1), 98–103.

[113] Yamanaka, S.; Isobe, H.; Kanda, K.; Saito, T.; Umena, Y.; Kawakami, K.; Shen, J.-R.; Kamiya, N.; Okumura, M.; Nakamura, H.; others. *Chem. Phys. Lett.* **2011**, *511*(1), 138–145.

[114] Saito, T.; Yamanaka, S.; Kanda, K.; Isobe, H.; Takano, Y.; Shigeta, Y.; Umena, Y.; Kawakami, K.; Shen, J.-R.; Kamiya, N.; Okumura, M.; Shoji, M.; Yoshioka, Y.; Yamaguchi, K. *Int. J. Quantum Chem.* **2012**, *112*(1), 253–276.

[115] Yamanaka, S.; Saito, T.; Kanda, K.; Isobe, H.; Umena, Y.; Kawakami, K.; Shen, J.-R.; Kamiya, N.; Okumura, M.; Nakamura, H.; Yamaguchi, K. *Int. J. Quantum Chem.* **2012**, *112*(1), 321–343.

[116] Isobe, H.; Shoji, M.; Yamanaka, S.; Umena, Y.; Kawakami, K.; Kamiya, N.; Shen, J.-R.; Yamaguchi, K. *Dalton Trans.* **2012**, *41*(44), 13727–13740.

[117] Yamaguchi, K.; Yamanaka, S.; Isobe, H.; Saito, T.; Kanda, K.; Umena, Y.; Kawakami, K.; Shen, J.-R.; Kamiya, N.; Okumura, M.; Nakamura, H.; Shoji, M.; Yoshioka, Y. *Int. J. Quantum Chem.* **2013**, *113*(4), 453–473.

[118] Yamaguchi, K.; Isobe, H.; Yamanaka, S.; Saito, T.; Kanda, K.; Shoji, M.; Umena, Y.; Kawakami, K.; Shen, J.-R.; Kamiya, N.; Okumura, M. *Int. J. Quantum Chem.* **2013**, *113*(4), 525–541.

[119] White, S. R. *Phys. Rev. Lett.* **1992**, *69*(19), 2863.

[120] Fisher, M. E. *Rev. Mod. Phys.* **1998**, *70*(2), 653.

[121] Kurashige, Y.; Chan, G. K.-L.; Yanai, T. *Nat. Chem.* **2013**, *5*(8), 660–666.

[122] Kusunoki, M. *Biochim. Biophys. Acta* **2007**, *1767*(6), 484–492.

[123] Kusunoki, M. *Biochim. Biophys. Acta* **2008**, *1777*(5), 477.

[124] Ogata, K.; Yuki, T.; Hatakeyama, M.; Uchida, W.; Nakamura, S. *J. Am. Chem. Soc.* **2013**, *135*(42), 15670–15673.

[125] Ushiyama, H.; Takatsuka, K. *Angew. Chem.* **2007**, *119*(4), 593–596.

[126] Schiff, L. I. *Quantum mechanics;* McGraw-Hill: New York, 1968.

[127] Debus, R. J. *Biochim. Biophys. Acta, Bioenerg.* **1992**, *1102*(3), 269–352.

[128] Schmidt, M. W.; Baldridge, K. K.; Boatz, J. A.; Elbert, S. T.; Gordon, M. S.; Jensen, J. H.; Koseki, S.; Matsunaga, N.; Nguyen, K. A.; Su, S.; Windus, T. L.; Dupuis, M.; Montgomery, J. A. *J. Comput. Chem.* **1993**, *14*(11), 1347–1363.

[129] Gordon, M. S.; Schmidt, M. W. *Theory and Applications of Computational Chemistry: the first forty years;* Elsevier: Amsteldam, 2005.

[130] Paldus, J. *J. Chem. Phys.* **1974**, *61*(12), 5321–5330.

[131] Paldus, J. *Int. J. Quantum Chem.* **1975**, *9*(S9), 165–174.

[132] Paldus, J. *Phys. Rev. A* **1976**, *14*(5), 1620.

[133] Shavitt, I. In *Methods of electronic structure theory;* Springer, 1977; pages 189–275.

[134] Shavitt, I. *Int. J. Quantum Chem.* **1977**, *12*(S11), 131–148.

[135] Shavitt, I. *Int. J. Quantum Chem.* **1978**, *14*(S12), 5–32.

[136] Lischka, H.; Shepard, R.; Brown, F. B.; Shavitt, I. *Int. J. Quantum Chem.* **1981**, *20*(S15), 91–100.

[137] Takatsuka, K.; Fueno, T.; Yamaguchi, K. *Theor. Chim. Acta* **1978**, *48*(3), 175–183.

[138] Mulliken, R. S. *J. Chem. Phys.* **1955**, *23*(10), 1833–1840.

[139] Hirshfeld, F. *Theor. Chim. Acta* **1977**, *44*(2), 129–138.

[140] Okuyama, M.; Takatsuka, K. *Chem. Phys. Lett.* **2009**, *476*(1), 109–115.

[141] Nagashima, K.; Takatsuka, K. *J. Phys. Chem. A* **2009**, *113*(52), 15240–15249.

[142] Okuyama, M.; Takatsuka, K. *Bull. Chem. Soc. Jpn.* **2012**, *85*(2), 217–227.

[143] Barth, I.; Manz, J.; Shigeta, Y.; Yagi, K. *J. Am. Chem. Soc.* **2006**, *128*(21), 7043–7049.

[144] Barth, I.; Hege, H.-C.; Ikeda, H.; Kenfack, A.; Koppitz, M.; Manz, J.; Marquardt, F.; Paramonov, G. K. *Chem. Phys. Lett.* **2009**, *481*(1), 118–123.

[145] Accardi, A.; Barth, I.; Kuhn, O.; Manz, J. *J. Phys. Chem. A* **2010**, *114*(42), 11252–11262.

[146] Nadal-Ferret, M.; Gelabert, R.; Moreno, M.; Lluch, J. M. *J. Chem. Phys.* **2011**, *134*(7), 074115.

[147] Kenfack, A.; Barth, I.; Marquardt, F.; Paulus, B. *Phys. Rev. A* **2010**, *82*(6), 062502.

[148] Kenfack, A.; Marquardt, F.; Paramonov, G.; Barth, I.; Lasser, C.; Paulus, B. *Phys. Rev. A* **2010**, *81*(5), 052502.

[149] Hege, H.-C.; Manz, J.; Marquardt, F.; Paulus, B.; Schild, A. *Chem. Phys.* **2010**, *376*(1), 46–55.

[150] Manz, J.; Yamamoto, K. *Mol. Phys.* **2012**, *110*(9-10), 517–530.

[151] Diestler, D. J.; Kenfack, A.; Manz, J.; Paulus, B.; Pérez-Torres, J. F.; Pohl, V. *J. Phys. Chem. A* **2013**, *117*(36), 8519–8527.

[152] Manz, J.; Perez-Torres, J. F.; Yang, Y. *J. Phys. Chem. A* **2014**, *118*(37), 8411–8425.

[153] Yachandra, V. K.; Yano, J. *J. Photochem. Photobiol. B* **2011**, *104*(1), 51–59.

[154] Yocum, C. F. *Coord. Chem. Rev.* **2008**, *252*(3), 296–305.

[155] Zaharieva, I.; Najafpour, M. M.; Wiechen, M.; Haumann, M.; Kurz, P.; Dau, H. *Energy Environ. Sci.* **2011**, *4*(7), 2400–2408.

[156] Saito, K.; Ishikita, H. *Biochim. Biophys. Acta* **2014**, *1837*(1), 159–166.

[157] Seasholtz, M. B.; Thompson, T. B.; Rondan, N. G. *J. Phys. Chem.* **1995**, *99*(51), 17838–17843.

[158] Reed, A. E.; Weinstock, R. B.; Weinhold, F. *J. Chem. Phys.* **1985**, *83*(2), 735–746.

Acknowledgments

This thesis is the summary of my study at the Graduate School of Science, University of Tokyo from 2009 to 2014, under the supervision of Prof. Kazuo Takatsuka. This work would not have been possible without a number of people. Foremost, I am grateful to my supervisor Prof. Kazuo Takatsuka for his continuous support in various ways. I learned a lot from him, not only electron dynamics, but also attitude toward scientific working and all. He let me freely work on science, but always took care of me. All the discussions with him was stimulating, and frequently inspiring new ideas of science and technology. I am grateful to Dr. Satoshi Takahashi for his additional support in many ways. He always listened to my situation, and gave kind advices as necessary. I actually met him first of all the colleagues, and that opportunity triggered me to study the present field of science. He also taught me basics of computation. I am grateful to Dr. Yasuki Arasaki and Dr. Takehiro Yonehara for their technical managements, as well as fruitful discussions on science. I could not have performed parallel computation using hundreds of computational cores without their supports. My computational program quite often caused technical troubles, but they kindly managed to recover those machines. Acknowledgment is also made to Ms. Yukiko Kousaka, Dr. Manabu Kanno, Dr. Michihiro Okuyama, Dr. Kengo Nagashima, Mr. Nobuki Inoue, Mr. Shin-ichi Koda, and Dr. Kota Hanasaki. Finally, I thank my family for their trust, encouragement and patience.